

TECHNICAL UNIVERSITY OF LIBEREC

FACULTY OF MECHANICAL ENGINEERING



Doctoral Dissertation

2013

Ing. Phan Thanh NHAN

TECHNICAL UNIVERSITY OF LIBEREC
FACULTY OF MECHANICAL ENGINEERING

Ing. Phan Thanh Nhan

**EXPERIMENTAL AND ANALYTICAL STUDY OF
THERMO-MECHANICAL PROPERTIES OF COMPOSITES
FABRICATED FROM GEOPOLYMER MATRIX
REINFORCED WOVEN FABRICS**

**EXPERIMENTÁLNÍ A ANALYTICKÝ VÝZKUM
TERMO-MECHANICKÝCH VLASTNOSTÍ
KOMPOZITNÍCH MATERIÁLŮ TVOŘENÝCH
GEOPOLYMERNÍ MATRICÍ VYZTUŽENÝCH TKANINOU**

Doctoral Dissertation

submitted to Department of Engineering Mechanics,
in partial fulfillment of the requirements
for the degree of doctor
of Philosophy in Mechanical Engineering

Supervisor:

Prof. Ing. Bohdana Marvalová, CSc.

Liberec – 2013

Acknowledgments

I would not have finished this PhD. dissertation without the guidance, support and assistance of not only many respectable professors, generous colleagues, and close friends but also funding projects.

I would like to express my respectful gratitude to my supervisor, Professor Bohdana Marvalová for all her guidance, support, advice and encouragement throughout my study in more than three years.

Specially, I am very grateful to Dr. Petříková for the financial support to me during my work.

I would like to thank Prof. Petr Louda from Department of Material Science for his laboratory with the raw materials and all equipments to help me fabricate and test geocomposite materials.

I would like to thank my colleagues from Nha Trang University, from Technical University in Liberec, who always persuade and give me emotional supports during the time of my study in Czech Republic.

In addition, I would like to acknowledge the general support provided by head, vice-head and all members of the Department of Engineering Mechanics, Faculty of Mechanical Engineering, and Technical University of Liberec.

Finally, I would share my happiness to my wife and my daughter who stood beside me when I needed it, and celebrated with me when I was done.

Prohlášení

Byl jsem seznámen s tím, že na mou doktorskou práci se plně vztahuje zákon č. 121/2000 o právu autorském, zejména §60 (školní dílo) a §35 (o nevýdělečném užití díla k vnitřní potřebě školy).

Beru na vědomí, že Technická univerzita v Liberci má právo na uzavření licenční smlouvy o užití mé práce a prohlašuji, že souhlasím s případným využitím mé práce (prodej, zapůjčení apod.).

Jsem si vědom toho, že užit své doktorské práce či poskytnout licenci k jejímu využití mohu jen se souhlasem Technické univerzity v Liberci, která má právo ode mne požadovat přiměřený příspěvek na úhradu nákladů, vynaložených univerzitou na vytvoření díla (až do jejich skutečné výše).

V Liberci

.....

vlastnoruční podpis

Místopřísežné prohlášení

Místopřísežně prohlašuji, že jsem doktorskou práci vypracoval samostatně s použitím uvedené literatury, pod vedením školitelkou.

V Liberci

.....

ABSTRACT

Geopolymers are inorganic polymeric materials with a chemical composition similar to zeolites but without defined crystalline structure and possessing ceramic-like features. They are still considered as a new material for coatings and adhesives, a new binder for fiber composites, and new cement for concrete.

Geopolymer materials possibly fabricate composite materials not only with excellent mechanical properties such as lightweight and high strength in compression but also with ideal fire resistant (can sustain temperatures up to 1000°C with long term exposure), low shrinkage, low thermal conductivity, non toxic fumes and smokes, and resisting all inorganic solvents (only affected by strong hydrochloric acid).

On the other hand, composites based on geopolymeric matrices are handled easily and do not require high heat, they are fabricated already at room temperature or in a simple autoclave (usually less than 150°C) during several hours.

However, most of pure geopolymer has low tensile and flexural strength, but from previous studies we can use continuous reinforcements (carbon, glass or basalt fibers) in these materials. Woven fabrics are the most commonly used textile system for composite applications because the mechanical properties of textiles are balanced than unidirectional fiber system and the technical processes using woven fabric as reinforcement in making composites handle easily and applied for all fields of industries.

The dissertation will focus on experimental evaluating as well as numerical simulating the thermo-mechanical properties of geopolymer binder with abbreviated name FC4 combined with commercial woven fabrics such as carbon, glass and basalt.

Key words: *geopolymer, woven fabric, geocomposite, simulation, mechanical property, microstructure, fire-resistant property.*

ABSTRAKT

Geopolymery jsou anorganické polymerní materiály s chemickým složením podobným zeolitům bez definované krystalové struktury, které se svým chováním blíží keramice. Geopolymery jsou stále považovány za nové materiály pro přípravu povrchových vrstev, lepidel a pojiv pro vláknové kompozity stejně jako materiály pro přípravu betonů.

Geopolymerní materiály mohou vyrobít kompozitních materiálů nejen s vynikajícími mechanickými vlastnostmi jako je lehké a vysoká pevnost v tlaku, ale také ideální odolné proti ohni (muže vydržet teploty až do 1000 °C s dlouhodobou expozicí), nízké smrštění, nízkou tepelnou vodivostí, které nejsou toxické výpary a kouří, a odolnost proti všem anorganickým rozpouštědlům (pouze ovlivněn silnou kyselinou chlorovodíkovou).

Na druhou stranu, jsou kompozity na bázi geopolymerních matric snadno manipulovat a nevyžadují mnoho tepla, jsou vyrobeny již při pokojové teplotě, nebo v jednoduchém autoklávu (obvykle méně než 150 °C) během několika hodin.

Nicméně, většina čistých geopolymery má nízkou pevnost v tahu a v ohybu, ale z předchozích studií můžeme použít kontinuální výztuže (uhlíková, skleněná nebo čedičová vlákna) v těchto materiálech. Tkaniny jsou nejpoužívanější textilní systém pro kompozitní aplikace, protože mechanické vlastnosti tkaniny jsou vyrovnanější než jednosměrná vlákna systém a technický proces užití tkanin jako výztuž při výrobě kompozitů může být manipulovan snadno a používán ve všech oblastech průmyslu.

Práce se zaměří na experimentální vyhodnocení, stejně jako numerická simulace termo-mechanické vlastnosti geopolymerního pojiva se zkráceným názvem FC4 v kombinaci s komerčními tkanin, jako jsou uhlík, sklo a čedič.

Klíčová slova: Geopolymer, tkaniny, geokompozit, simulace, mechanické vlastnosti, mikrostruktury, ohnivzdorné vlastnosti.

Table of Contents

List of Figures.....	8
List of Tables	11
Notation and Symbols.....	13
Chapter 1: INTRODUCTION	15
Outline of the dissertation	17
Chapter 2: OVERVIEW OF LITERATURE	18
2.1 INTRODUCTION	18
2.2 GEOPOLYMER TERMINOLOGY	18
2.3 GEOPOLYMERIZATION.....	20
2.4 GEOPOLYMER PROPERTIES	21
2.5 GEOPOLYMER APPLICATIONS	23
Chapter 3: THEORETICAL FOUNDATION OF 2-D FABRIC REINFORCED COMPOSITE	26
3.1 2-D FABRICS.....	26
3.1.1 Overview.....	26
3.1.2 Geometrical parameters of plain woven fabric	27
3.1.3 Load in principal directions	28
3.2 MECHANICS OF WOVEN REINFORCED COMPOSITES.....	29
3.2.1 Mechanical properties for a thin lamina	29
3.2.2 Lamination theory	30
3.2.2 Lamination theory including transverse shear stresses	33
3.2.3 Thermal effects in a laminate	35
3.2.4 Application of lamination theory for studied geocomposites	36
3.2.5 Thermo-mechanical properties of constituents in a repeating unit cell.....	37
Chapter 4: EXPERIMENTS AND MATERIAL PARAMETER IDENTIFICATION.....	42
4.1 INTRODUCTION.....	42
4.2 EXPERIMENTAL EQUIPMENTS.....	42
4.2.1 Universal testing machine TIRA test 2810.....	42
4.2.2 Universal testing machine INSTRON Model 4202	43

4.2.3 System Q-400 digital cameras Dantec Dynamics	43
4.2.4 System of TESCAN VEGA 3XM microscope and optical microscope NIKON EPIPHOT 200.....	43
4.2.5 System of vacuum bagging and drying furnace; Heating oven	44
4.2.6 System of thermal conductivity NETZSCH model LFA 447 NanoFlash	45
4.3 GEOPOLYMER RESIN	46
4.3.1 Specimen preparation	46
4.3.2 Experimental results	47
4.4 WOVEN FABRIC REINFORCEMENTS	49
4.4.1 Overviews	49
4.4.2 Experiments and identification of mechanical properties of fabrics.....	51
4.5 GEOCOMPOSITES.....	54
4.5.1 Fabrication of geocomposite samples	54
4.5.2 Volume fractions of fibers and voids in geocomposites.....	54
4.5.3 Mechanical properties of geocomposites in tension.....	56
4.5.4 In-plane shear properties of geocomposites.....	57
4.5.5 Interlaminar shear strength of geocomposites	60
4.5.6 Fire-resistant properties of geocomposites	63
4.5.7 Thermal conductivity of geocomposites.....	70
4.5.8 Micro-structural evolution	72
4.5.9 Conclusion	73
Chapter 5: NUMERICAL SIMULATION OF ELASTIC BEHAVIOR OF GEOCOMPOSITES	76
5.1 INTRODUCTION.....	76
5.2 GEOMETRICAL MODEL OF UNIT CELLS.....	76
5.3 IMPLEMENTATION OF SIMULATING MODELS.....	79
5.3.1 The mosaic model	80
5.3.2 The crimp model	85
5.3.3 Result and Discussion.....	90
5.4 FEM IMPLEMENTATION WITH ANSYS AND TEXGEN	91
5.4.1 Model of internal architecture of woven laminate in 3-D geometry.....	91
5.4.2 Mechanical properties of constituents in a repeating unit cell.....	92

5.4.3 Prediction of geocomposite elastic properties in tension	92
5.4.4 Prediction of geocomposite elastic properties in in-plane shear	96
5.4.5 Prediction of geocomposite interlaminar shear strength	98
5.4.5 Prediction of geocomposite thermo-mechanical behaviors	99
Chapter 6: POTENTIAL APPLICATIONS	104
Chapter 7: CONCLUSIONS AND FUTURE WORKS	107
Literatures.....	109
PUBLICATIONS OF AUTHOR.....	115
APPENDIX A.....	116
APPENDIX B.....	122

List of Figures

Figure 2.1	The geopolymer terminology.....	19
Figure 2.2	Conceptual model for geopolymerization.....	21
Figure 2.3	Geopolymers and potential applications.....	25
Figure 3.1	2-D fabrics.....	26
Figure 3.2	Woven fabrics.....	27
Figure 3.3	Simple model of plain weave balanced fabric.....	27
Figure 3.4	Geometrical model.....	29
Figure 3.5	Schematic of a laminate.....	31
Figure 3.6	Laminate geometry.....	31
Figure 3.7	In-plane, bending, and twisting loads applied on a laminate.....	32
Figure 3.8	Plate under lateral loading.....	33
Figure 3.9	Bending of a short thin beam and stress state of element.....	34
Figure 3.10	Laminate is subjected by tensile load and shear load.....	37
Figure 3.11	The geometrical model of a yarn section.....	38
Figure 3.12	Five ultimate strength parameters for a unidirectional lamina.....	39
Figure 3.13	Model of failure tensile strains of the matrix in the transverse direction...40	40
Figure 4.1	Universal testing machine TIRA test 2810.....	42
Figure 4.2	Universal testing machine INSTRON Model 4202.....	42
Figure 4.3	Digital cameras and main window of Istra 4D software.....	43
Figure 4.4	Systems of TESCAN VEGA 3XM and NIKON EPIPHOT 200 microscopy.....	44
Figure 4.5	System of vacuum bagging and drying furnace ED23 and Heating oven...44	44
Figure 4.6	System of thermal conductivity NETZSCH model LFA 447 NanoFlash...45	45
Figure 4.7	Preparation of geopolymer resin.....	46
Figure 4.8	EDX spectrum of geopolymer mixture.....	47
Figure 4.9	Geopolymer specimens.....	47
Figure 4.10	Typical stress vs. strain curves in flexure of geopolymers.....	48
Figure 4.11	Typical load vs. displacement curve of compressive test of geopolymer...49	49
Figure 4.12	Woven cloths.....	50

Figure 4.13	Tensile stress-strain diagrams for various reinforcing fibers.....	51
Figure 4.14	Tensile diagram of fabrics.....	52
Figure 4.15	Structure of woven textile.....	53
Figure 4.16	Process for the preparation of test samples.....	55
Figure 4.17	Tension diagram of geocomposites.....	56
Figure 4.18	Tensile failure of geocomposites.....	57
Figure 4.19	Geocomposite specimens for shear and experiments.....	58
Figure 4.20	In-plane shear stress-strain diagrams and The first principal strain field of geocomposites from DIC camera.....	59
Figure 4.21	Failure mode of geocomposite samples under shear loads.....	60
Figure 4.22	Failure mode of geocomposite samples under shear loads.....	61
Figure 4.23	The stress-strain diagrams for a three-point bending tests of short-beam...62	
Figure 4.24	Failure modes of geocomposites under lateral loads.....	62
Figure 4.25	Heating the samples at 1000°C.....	65
Figure 4.26	Thickness expansion and mass retention of geocomposites graphs.....	67
Figure 4.27	Graphs of residual flexural properties of geocomposites after heating.....	68
Figure 4.28	Observation of the microstructure of the geocomposite when heated to the temperature 1000°C.....	70
Figure 4.29	Graphs of thermal conductivity and specific heat of geocomposites.....	72
Figure 4.30	SEM images of geopolymer and geocomposites without fire.....	73
Figure 4.31	SEM images of fired geo composites at 600 and 1000 °C	74
Figure 5.1	Unit cell and geometrical model of unit cell.....	76
Figure 5.2	Mosaic model	81
Figure 5.3	Direction of yarn element in the global system	87
Figure 5.4	The geometrical models of a repeating unit cell of composite with carbon fabric.....	92
Figure 5.5	Tension graphs of carbon geocomposites.....	94
Figure 5.6	The spectra of distribution of Von-Mise stress on matrix and tension stress on yarns in tensile model.....	95
Figure 5.7	Shear graphs of carbon geocomposites.....	97
Figure 5.8	The spectra of distribution of Von-Mise stress on matrix and failure index value on yarns in in-plane shear model.....	98

Figure 5.9	The spectra of distribution of Von-Mise stress on matrix and failure index value on yarns in interlaminar shear model.....	100
Figure 5.10	Thermal strain graphs of geocomposite reinforced carbon fabric.....	102
Figure 5.11	The spectra of distribution of Von-Mise stress on matrix and failure index value on yarns in thermal model at 200°C.....	103
Figure 6.1	Polystyrene and Plastic coated by pure geopolymer. Polystyrene coated by geopolymer mortar.....	104
Figure 6.2	Portland concrete coated by pure geopolymer before and after heated 600°C.....	105
Figure 6.3	The box made from geopolymer composite reinforced basalt fabric	105
Figure 6.4	Wooden plate coated by geopolymer mortar and after heated 354°C in the oven, outside only 175.8°C.....	105
Figure 6.5	Geocomposite samples after cutting and drilling and geopolymer mortar with different colors.....	106
Figure 6.6	The broken architecture sample was pasted by geopolymers.....	106
Figure A.1	Geocomposite samples after heating at different levels.....	116
Figure A.2	Flexural graph of geocomposite 7E after heating at 600°C.....	117
Figure A.3	Flexural graph of geocomposite 7E+2x1C after heating at 600°C.....	117
Figure A.4	Flexural graph of geocomposite 7E+2x2B after heating at 600°.....	117
Figure A.5	Flexural graph of geocomposite 10C after heating at 1000°C.....	118
Figure A.6	Flexural graph of geocomposite 15B at room temperature.....	118
Figure A.7	Flexural graph of geocomposite 12B+2x1C after heating at 200°C.....	118
Figure A.8	Observation of the microstructure of the geocomposite 10C in room temperature and after heating at different levels.....	119
Figure A.9	Observation of the microstructure of the geocomposite 7E in room temperature and after heating at different levels.....	120
Figure A.10	Observation of the microstructure of the geocomposite 15B in room temperature and after heating at different levels.....	121

List of Tables

Table 4.1	Percentages of chemical elements in geopolymers.....	46
Table 4.2	Density and bulk volume shrinkage of pure geopolymer matrix.....	48
Table 4.3	The flexural properties of geopolymer.....	48
Table 4.4	The compressive properties of geopolymer.....	49
Table 4.5	Characteristics of reinforced fabrics.....	50
Table 4.6	Mechanical properties of carbon, E-glass, and basalt fabrics.....	53
Table 4.7	Mechanical properties of filaments in accordance with Japanese Industrial Standard (JIS R 7601).....	54
Table 4.8	Physical properties of geocomposites.....	56
Table 4.9	Tensile properties of geocomposites.....	56
Table 4.10	In-plane shear properties of geocomposites.....	59
Table 4.11	Interlaminar shear strengths of geocomposites.....	63
Table 4.12	Six kinds of samples for experiments of fire-resistant properties of geocomposites.....	64
Table 4.13a	Experiment results of geocomposite 7E after heating at different levels	65
Table 4.13b	Experiment results of geocomposite 10C after heating at different levels.....	65
Table 4.13c	Experiment results of geocomposite 15B after heating at different levels.....	66
Table 4.13d	Experiment results of geocomposite 5E+2x2B after heating at different levels.....	66
Table 4.13e	Experiment results of geocomposite 5E+2x1C after heating at different levels.....	66
Table 4.13f	Experiment results of geocomposite 12B+2x1C after heating at different levels.....	66
Table 4.14a	Thermo-physical properties of carbon geocomposite.....	71
Table 4.14b	Thermo-physical properties of E-glass geocomposite.....	71
Table 4.14c	Thermo-physical properties of basalt geocomposite.....	71

Table 5.1	The basic geometrical parameters of geocomposites.....	78
Table 5.2	The distribution of fibers, matrix, and voids in each of unit cells.....	79
Table 5.3	Values of unidirectional elastic parameters.....	80
Table 5.4	Values of relative volumetric factors.....	85
Table 5.5	The elastic properties of geocomposites from numerical method.....	86
Table 5.6	The strengths of yarns in geocomposites.....	88
Table 5.7	Analytical and experimental results for composites... ..	90
Table 5.8	Tensile properties of geocomposites from simulation.....	92
Table 5.9	CTE of carbon yarn, basalt yarn, E-glass yarn.....	96

Notation and Symbols

We attempt to employ notations that reflect as clearly as possible differences of kind among mathematical entities. The scalar quantities are denoted by Latin or Greek italic letters while vectors and second-order tensors and/or matrices are represented by the boldface characters. Subscript indices i, j, \dots of vectors, matrices and tensors signify specific components of the corresponding vectors, matrices and tensors.

A	Extensional stiffness matrix
B	Coupling stiffness matrix
C	Stiffness matrix
D	Bending stiffness matrix
S	Compliance matrix
Q	Strain transformation matrix
a	Extensional compliance matrix
b	Coupling compliance matrix
d	Bending compliance matrix
ε	Vector of laminate strain
k	Vector of laminate curvatures
N	Vector of applied force resultants
M	Vector of applied moment resultants
N^T	Vector of thermal force resultants
M^T	Vector of thermal moment resultants
α	Vector of the coefficients of thermal expansion
E	Elastic modulus
G	Shear modulus
ν	Poisson's ratio
Q	Components of the reduced transformed stiffness matrix
θ	Angle of orientation
T	Temperature
t, b, l	Thickness, width, length
V	Volume fraction

c	Crimp of fabrics
p	Pitch of fabrics
ρ	Mass density
FI	Failure index
$\sigma_{Lu}^T, \sigma_{Lu}^C$	Longitudinal tensile, compressive strength of unidirectional lamina
$\sigma_{Tu}^T, \sigma_{Tu}^C$	Transverse tensile, compressive strength of unidirectional lamina
σ_{LTu}	In-plane shear strength of unidirectional lamina

Chapter 1

INTRODUCTION

The remarkable achievements of inorganic chemistry made through geosynthesis and geopolymerisation include mineral polymers which termed as polysatate or geopolymers. Geopolymer materials possibly fabricate composite materials not only with excellent mechanical properties such as lightweight and high strength but also with ideal fire resistant (can sustain temperatures up to 1000 °C with long term exposure), low shrinkage, low thermal conductivity, non toxic fumes and smokes, and resisting all inorganic solvents (only affected by strong hydrochloric acid) [1-5]. These special properties permit us to use more efficiently geopolymer matrix composites in high technologies, especially for various applications that require high temperature resistance [6]. These materials can be replaced efficiently traditional composites which are made with carbon or glass fibers and organic matrices such as epoxy (most organic matrix composites cannot be used in applications that require more than 200 °C temperature exposure) or ceramic matrices (high costs associated with special processing requirements) [6, 7]. On the other hand, composites based on geopolymeric matrices are handled easily and do not require high heat, they are fabricated already at room temperature or in a simple autoclave (usually less than 150 °C) during several hours. In addition, most of types of fibers can be used with the geopolymer matrices and especially geopolymer materials can protect carbon from oxidation [6].

Recently, geopolymers has emerged as a promising new material similar to Ordinary Portland Cement (OPC) but with superior features. The process creating geopolymers uses less energy, releases less CO₂ than OPC. Furthermore, it may be utilized waste materials from factories such as: fly ash, glass, stone powder, mine tailings, etc to make geopolymer mortar and concrete. This is beneficial for resource conservation, environmental protection, and preventing ecological damages caused by exploitation of raw materials for making cement [8, 9].

Thanks to the outstanding advantages of geopolymers more and more public and private research institutes and companies are investigating and finding geopolymer applications in all fields of industries, such as civil engineering, plastics industries, waste management, automotive and aerospace industries, non ferrous foundries and metallurgy, etc.[1, 3, 4]. The composites fabricated from geopolymers and woven fabrics are plates

sustainable in the high temperature environments that can be applied for many fields of industries [10]. Therefore, study of the thermo-mechanical properties of geocomposites reinforced by woven fabric will provide the theoretical basis as well as experimental data for the purpose of understanding the nature of the material to applications.

In order to achieve the above objectives, many tasks related to experimental parts and numerical simulations should be implemented, namely some main tasks as follows:

- Microstructure and mechanical properties of geopolymer matrices.
- Properties of commercial reinforcements: carbon, glass and basalt woven fabric in the realistic condition and after different temperature of treatment.
- Mechanical properties of reinforced geopolymer composite system under a room temperature of treatment (tensile, in-plane shear, flexural, interlaminar shear properties).
- Mechanical properties and microstructures of reinforced geopolymer composite system under high temperature of treatment (bending properties).
- Thermal properties of reinforced geopolymer composite system in high temperature of treatment.
- Numerical models and finite element simulation applied to the prediction of thermo-mechanical properties of geocomposites.
- Some recommended application of geopolymers and geocomposites

Outline of the dissertation

The dissertation is organized as follows:

Short introduction to the subject of dissertation thesis is in Chapter 1.

The overview of the recent literature concerning history of geopolymer, geopolymer chemistry and synthesis, the properties of geopolymer binders, and the potential applications of geopolymer is presented briefly in Chapter 2.

Chapter 3 summarizes the theory of the mechanical performance of woven fabric reinforced polymers that will help us to conduct experiments, evaluate the features as well as simulate the mechanical properties of materials.

In the Chapter 4, essential properties of geopolymer matrices and fiber reinforcements which considered as initial materials for geocomposites are presented. Many micro-cracks in cured matrices as natural defects of inorganic matrix are shown by SEM images. The properties of commercial textiles evaluated at real conditions and after high temperature exposing are exhibited as well. Finally, mechanical properties of result geocomposites are tested in different load conditions as well as fire-resistant properties of geocomposites are accounted for especially.

Chapter 5 will devote to represent some numeric simulations of elastic behavior of geocomposite materials. The main goal is to verify the elastic parameters obtained from experiments in previous chapters associating with prediction of initial failures of geocomposite materials.

With the Chapter 6, author will recommend some applications of geopolymers as well as geocomposites reinforced with fabric fibers to practice.

Some conclusions, discussions and future perspectives are presented in Chapter 7.

Appendix A shows some pictures of sample after tests, some typical experimental graphs, and microstructure of geocomposites after heating at elevated temperatures.

Finally, program codes developed in Matlab is illustrated in Appendix B.

Chapter 2

OVERVIEW OF LITERATURE

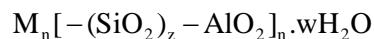
2.1 INTRODUCTION

This chapter provides a brief overview of history of geopolymer, geopolymer chemistry and synthesis, the properties of geopolymer binders, and the potential applications of geopolymer.

2.2 GEOPOLYMER TERMINOLOGY

The term geopolymer has been first coined since 1979 by a French professor Joseph Davidovits, they are inorganic polymeric materials with a chemical composition similar to zeolites but containing an amorphous structure and possessing ceramic-like in their structures and properties [1, 4]. Geopolymer are synthesized and hardened at ambient pressure and temperature [11]. There are two main constituents of geopolymers, namely the source materials and the alkaline liquids. The source materials for geopolymers based on alumina-silicate should be rich on silicon (Si) and aluminum (Al) such as geological, slag, fly ash, rice husk ash, stone powder, ect. The choice of the source materials for making geopolymers depends on factors such as availability, cost, type of application, and specific demand of the end users. The most common alkaline liquid used in geopolymerisation is combination of sodium hydroxide (NaOH) or potassium hydroxide (KOH) and sodium silicate or potassium silicate [12].

To discuss the chemical structure of geopolymers, the term ‘sialate’ is an abbreviation for silicon-oxo-aluminate and is used here to describe the bonding of silicon and aluminum by bridging oxygen. And the term poly(sialate) was suggested as a descriptor of silico-aluminate structure of the type of material [1]. The amorphous to semi-crystalline three dimensional of sialate network consists of SiO_4 and AlO_4 tetrahedral which are linked alternately by sharing all the oxygens to create basic polymeric Si-O-Al bonds. Poly(sialates) are said to have an empirical formula of [1, 2]:



Where M is a monovalent cation such as potassium (K^+) or sodium (Na^+), n is the degree of polycondensation and z is either 1, 2, 3 or $\gg 3$. Poly(sialate) are described as chain and ring

2.3 GEOPOLYMERIZATION

Many researches on the formation mechanism have been made since the invention of geopolymers, but only one formation mechanism was proposed by Prof. Davidovits. Because, geopolymerization is a complicated process, the exact process is not fully understood so far although the involved mechanism has been studied in the last three decades. Therefore, the understanding of geopolymerization process and its effective factors is useful for the application of geopolymeric materials. Davidovits explained that geopolymer synthesis consists of three steps dissolution of aluminosilicate under a strong alkali solution, reorientation of the free ion clusters, and polycondensation but that each step includes many pathways [13-15].

The most proposed mechanisms for the geopolymerization process include the following four main stages [16, 17]:

(i) Dissolution of solid aluminosilicate sources in alkaline sodium silicate solution.

During this stage, Si and Al are transferred from the solid phase to the aqueous one. The dissolution results in the generation of soluble aqueous monomeric species of Si and Al. This type of dissolution is called congruent [13, 18]. For some researchers, the dissolution results in the release of oligomeric molecular units having composition, which is dependent on the type of the solid aluminosilicate raw material. This type of dissolution is called incongruent [19, 20]. There are not enough data to exclude either of the dissolution types. In the case of dissolution of industrial aluminosilicate minerals such as kaolin and feldspars, the incongruent type seems to be predominant. In the case of waste aluminosilicate materials with complex composition, the congruent type seems to be predominate [21].

(ii) Formation of Si and/or Si–Al oligomers in the aqueous phase.

In case of congruent type of dissolution, certain chemical reactions take place between the soluble aqueous monomeric species of Si and Al, resulting in the formation of the geopolymers precursors which are oligomeric species (polynuclear hydroxy-complexes) consisting of polymeric bonds of Si–O–Si and Si–O–Al type [22, 23].

(iii) Polycondensation of the oligomeric species or units in the aqueous phase to form an inorganic polymeric material [21].

(iv) The hardening of the gel that mean bonding of undissolved solid particles in the final geopolymeric structure [16, 21].

Fig. 2.2 presents a highly simplified reaction mechanism for geopolymerization. The reaction mechanism shown in the figure outlines the key processes occurring in the transformation of a solid aluminosilicate source into a synthetic alkali aluminosilicate.

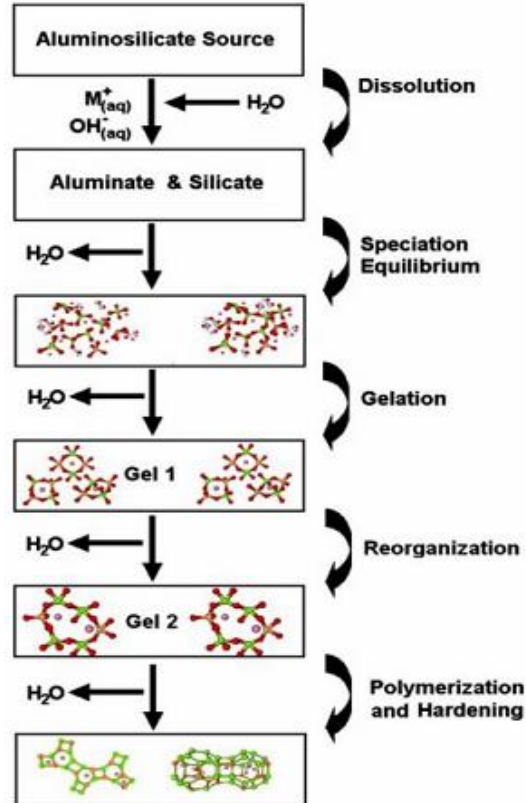


Fig. 2.2 Conceptual model for geopolymerization [13]

2.4 GEOPOLYME PROPERTIES

In order to use geopolymers as an engineering material, knowledge of their chemical, physical, and mechanical properties and so on must be fully understood. While the earlier researches were conducted through industry and kept as proprietary knowledge [1], there have been recently numerous studies attempting to clarify the properties of these materials.

Specifications of geopolymer materials have often been explained in terms of their microstructural properties. These include both the porosity of the materials and extent to which the geopolymerization takes place. Using Nuclear Magnetic Resonance (NMR), a presence of aqueous $Al(OH)_4^-$ was discovered to be trapped inside pores within the geopolymeric binders [24]. This implies that not only is a portion of the aluminum not being

reacted, but this inability to completely react creates porosities [24]. The presence of this aqueous phase was also correlated to the silicon to aluminum ratio used to prepare the sample and found that geopolymers with $\text{Si:Al} \leq 1.40$ cannot be accurately characterized by their Si:Al ratio because the degree of unreacted aluminum is too great. In fact, when curing conditions and source materials are held constant, the Si:Al ratio directly affects the nature of the porosity with higher Si:Al ratios having larger overall pore volumes but lower average pore diameter [25]. The same effect was also analyzed in another study in an attempt to tailor porosity to meet specific properties. It was discovered that choosing an appropriate alkali activator and curing conditions would enable the ability to control the geopolymerization process and obtain desired porosities [26]. Other studies have also presented that Si:Al ratios directly affect the rate and extent of geopolymerization and thereof production. It has also been shown that incomplete geopolymerization can lead to pockets of unreacted metakaolin which act as structural point defects within the material [27]. In order to study the effect of the chemical composition on this phase, Singh and his colleagues determined that when the $\text{SiO}_2:\text{Al}_2\text{O}_3$ ratio is increased, the percent of unreacted metakaolin will be decreased. The unreacted phase, however, was still present even with $\text{SiO}_2:\text{Al}_2\text{O}_3$ ratios as high as 15 [27]. The process of the geopolymerization is carried out more fully; in case additional silica is added to the sample until an equilibrium point is reached, at which the excess silica begins to hinder the alkali cations ability to react with the aluminum. Controlling the $\text{SiO}_2:\text{M}_2\text{O}$ ratio ($\text{M} = \text{Na}$ or K) is another factor that influences the reactivity. It was determined that around $\text{SiO}_2:\text{M}_2\text{O} = 2.00$ the maximum amount of geopolymerization occurs with a decreasing amount of reactivity as $\text{SiO}_2:\text{M}_2\text{O}$ ratios deviate from that point [28]. Still others theorize that the source material itself is responsible for the extent of unreacted materials. It has been discovered that geopolymerization reactions only occur at the surfaces of the particles of source materials [29]. Therefore, the particle size of the source materials will be the main factor in determining the extent of geopolymerization where source materials with high specific surface area will react more homogeneously due to the higher availability of surface molecules which can interact in the reaction [30].

In order to effectively apply geopolymers as an engineering material, especially construction material, many researchers have tried to determine the mechanical and elastic properties of geopolymers such as Young's modulus, compressive strength, and flexural

strength. Recently, the physical and chemical properties, however, have been clarified in many researches.

The two most commonly used aluminosilicates are metakaoline and fly-ash, they are quite much available in nature and forms as a byproduct of industrial process. Many studies have been performed to determine the compressive strength and flexural strength of the derived geopolymers. For kaolin based geopolymers without aggregates, the compressive strengths range from 10 MPa to 100 MPa [30, 31] while fly ash based geopolymers without aggregates have been shown to range between 20 MPa and 100 MPa [32, 33]. Oleg Botnovsky and his colleagues have determined that the flexural strength of geopolymers based on metakaolin without the use of aggregates varies from 9 MPa to 16 MPa [34]; when 4 MPa of compression is used in the molds, however, the bending strength of pure geopolymer could reach at approximately 50 MPa [29]. Fly ash based geopolymers without aggregates, however, have been recorded as having a flexural strength ranging in a quite range from 2.0 MPa to 14.2 MPa [33, 35].

In company with strength, additionally, Young's modulus or elastic modulus of the material is also very important parameter to be investigated for engineering applications. Because the geopolymer materials are porous naturally, complicated fracture mechanics lead to wide ranges of uncertainties when strengths are experimentally evaluated due to the destructive nature of these tests; therefore, it has been suggested that Young's modulus but not the compressive strength is the most effective mean of rating the physical nature of geopolymeric materials [25]. Throughout the literature, the typical values of compressive Young's modulus reported for metakaolin based geopolymers without aggregates range from 1.5 GPa to 6 GPa [25, 31]. Concerning about the Young's modulus of geopolymers based on fly ash without aggregates, however, we found no studies evaluated this value up to now.

2.5 GEOPOLYMER APPLICATIONS

Geopolymer materials with properties such as quick setting, low permeability, acid resistant, high early strength, fire resistant, and low costs have numerous possibilities for industrial applications. The original application of geopolymers was as a fire resistant material [1]. Geopolymers are ideal for high temperature applications because, even though its thermal conductivity increases with temperature, the thermal conductivity still remains lower than that of other structural metals by an order of magnitude or more [36]. Furthermore, while concrete

may explodes at temperatures around 450 °C, geopolymers have been shown to remain structurally stable at temperatures up to 800 °C [36]. When combined with carbon fibers to form a composite material, geopolymers proved to cost less than traditional carbon fiber/resin materials and perform better without any ignition, burning, or smoking and retain 63% of its initial flexural strength at temperatures where resins loose almost all of their strength [37]. Need for green technologies have also created applications for geopolymers in areas involving immobilizing toxic metals and reducing CO₂ emissions [1]. Producing ordinary Portland cement generates a great deal of CO₂. It has been estimated that for every ton of cement that is produced by traditional methods, approximately one ton of CO₂ is also produced [38]. In order to combat this pollution source, geopolymers have been used either as replacements to or as additives to cement because of the similar nature and properties of these materials [38, 39]. The reduction of energy required to produce geopolymers as compared to Portland cement is also significant; clinker, a component of Portland cement requiring calcination, requires 1450 °C whereas, metakaolin can be formed at 750 °C over a shorter period of time and fly-ashes do not require any pre-treatment [40]. Geopolymers are also an environmentally friendly material because they can be formed out of waste materials, such as fly ash, furnace slag, or volcanic ash, that typically are discarded [39]. A third environmental application of geopolymers is as a means to immobilize toxic wastes, such as arsenic, mercury, and lead along with other heavy metals, asbestos, and radioactive wastes, some of which are often thrown into landfills where they pose a risk to local bodies of water and agriculture [41]. Geopolymers are an excellent choice of construction materials whenever landfills and waste sites are being constructed and can be used as a solid basis to prevent leakages and erosions, an effective cap to prevent rain water contamination and provide a safe cover for the purpose of building, and as interior structures to prevent wastes layers from contacting each other or dangerously shifting [41].

In conclusion, the potential application of geopolymers and composites thereof are summerized in Fig. 2.3 [42]. The atomic ratio Si:Al in the poly(sialate) structure determines the properties and application fields. A low Si:Al ratio (1,2,3) initiates a 3D-Network that is very rigid. A high Si:Al ratio confers linear polymeric character on the geopolymeric materials.

The current commercial use of geopolymers alone, compared to plastics, is limited because of the complexity of large scale processing, high density and problems with

machining and molding, and most importantly, their brittleness [43].

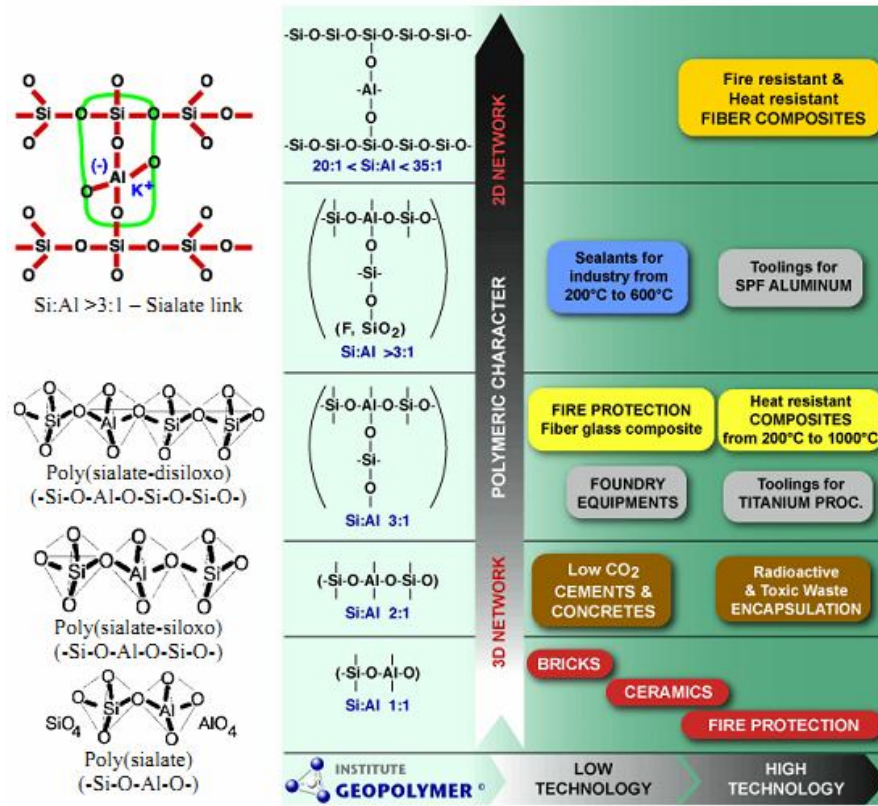


Fig. 2.3 Geopolymers and potential applications [42].

Chapter 3

THEORETICAL FOUNDATION OF 2-D FABRIC REINFORCED COMPOSITE

An overview of the theory of the mechanical performance of woven fabric reinforced polymers will be presented briefly. These facilities help us to conduct experiments, evaluate the features as well as simulate the mechanical properties of materials.

3.1 2-D FABRICS

3.1.1 Overview

Fabrics are made using yarns or fibers as the basic manufacturing unit. *Woven*, *knitted*, and *braided* fabrics are made from yarn. In the textile nomenclature, woven fabrics are formed by *interlacing* yarns, knitted by *interlooping* yarns, and braided by *intertwining* yarns. These fabrics typically have thicknesses very smaller than widths and lengths [44].

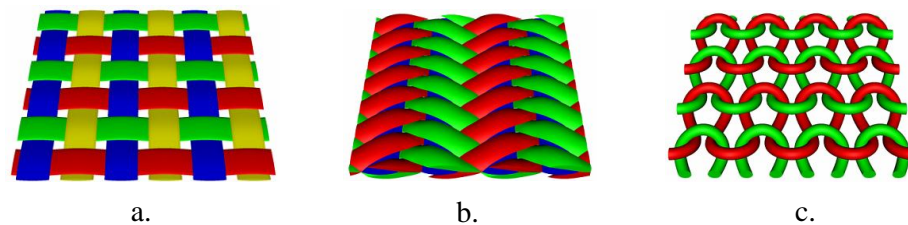


Fig. 3.1 2-D fabrics: a. Woven ; b. Braided ; c. Knitted

Woven fabrics are the most commonly used textile system for composite application. The woven structure is characterized by the orthogonal interlacing of two sets of yarns, called *warp* and *weft* yarns. The warp yarns are aligned with the direction of the fabric leaving the loom, which is also called the warp direction. A warp yarn may also be called an *end*. The weft yarn run perpendicular to the warp direction, and are sometimes called *fill* yarns or *pick* yarns.

Some of the most basic weave structures are illustrated in fig. 3.2. In this figure, the four most common weave structures: *plain* weave, *twill* weave, *satin* weave, and *basket* weave are shown.

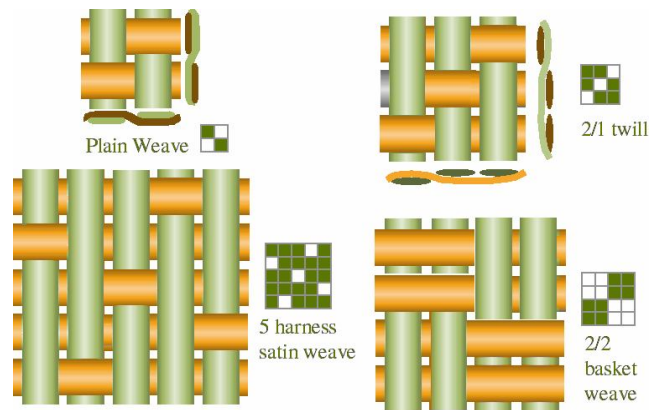


Fig. 3.2 Woven fabrics

3.1.2 Geometrical parameters of plain woven fabric

Investigation of fabric tensile properties starts at definition of relaxed state. It is described in (Lomov et all, 2007) etc. Simple model of plain weave balanced fabric is shown in Fig. 3.3 [45].

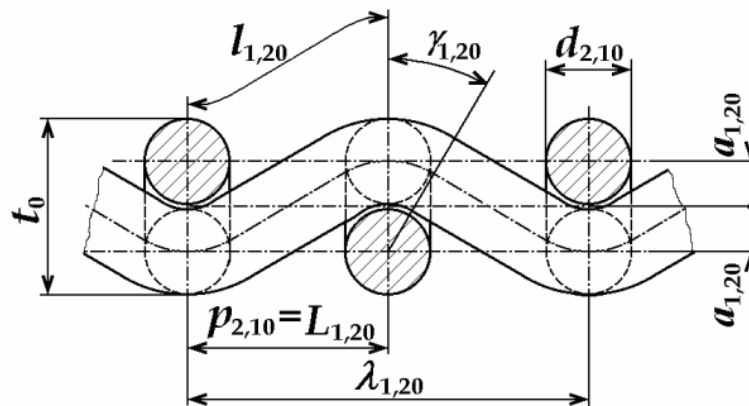


Fig. 3.3 Simple model of plain weave balanced fabric

Wavelength λ_1 of warp is defined by weft pitch p_2 and vice versa. Fabric thickness is t ; and so $\lambda_{1,20} = 2p_{2,10}$ where indices 1, 2, 0 denote warp direction, weft direction, and relaxed state of fabrics. Main parameters of crimp wave are: wavelength λ , wave amplitude a and length of the yarn axis l . Wave amplitudes a are dependent on yarn diameters, imposed load (contemporary or in fabric history) and so on.

Crimp of the yarns in woven fabric as numeric parameter c is defined by equation (3.1); wavelength of warp λ_1 corresponds with pitch of weft p_2 and vice versa.

$$c_{1,20} = \frac{l_{1,20}}{p_{2,10}} - 1 \quad \text{or} \quad l_{1,20} = p_{2,10}(1 + c_{1,20}) \quad (3.1)$$

Crimp levels in woven fabric depend on the texture of weave and the yarn size and influence fiber volume fraction, thickness of fabric, and mechanical performance of fabric. A fabric with high crimp can lead to reduce tensile and compressive properties, to increase shear modulus in the dry fabric and the resulting composite.

It is possible to count crimp of yarn when using Pierce's model

$$c_{1,20} = 2.52 \left(\frac{a_{1,20}}{p_{2,10}} \right)^2 \quad \text{or} \quad c_{1,2} = 2.52 \left(\frac{a_{1,2}}{p_{2,1}} \right)^2 \quad (3.2)$$

Where $c_{1,2}$, $a_{1,2}$, $p_{2,1}$ are crimp, wave amplitude and pitch when the fabric is loaded.

Using equations (3.1) and (3.2) length of the yarn in a crimp wave l can be determined

$$l_{1,20} = (2.52 \cdot a_{1,20}^2 + p_{2,10}^2) / p_{2,10} \quad \text{or} \quad l_{1,2} = (2.52 \cdot a_{1,2}^2 + p_{2,1}^2) / p_{2,1} \quad (3.3)$$

3.1.3 Load in principal directions

Many researchers attempted to analyze fabrics loaded in principal direction in different publications (Hearle et al., 1969; Hu, 2004; Pan, 1996 etc). Some important features are necessary to focus as follows

a. Fabric breaking force, $F_{fb1,2}$ (subscripts 1, 2 specify warp or weft direction of imposed load)

A simple formulas (3.4) to calculate $F_{f1,2}$ (Kovar, 2003) can be used, in which $F_{1,2b}$ are breaking forces of one warp or weft yarn, $C_{1,2u}$ are coefficients of utilization of these forces at fabric break, and $S_{1,2}$ are fabric sett (yarn density) in warp or weft directions.

$$F_{fb1,2} = S_{1,2} \cdot F_{1,2b} \cdot C_{1,2u} \quad (3.4)$$

The coefficients $C_{1,2u}$ are dependent on yarn and fabric unevenness and fabric jamming. Because determination of coefficients $C_{1,2u}$ is not easy, the strength of fabrics is obtained by tensile textile experiments.

b. Fabric breaking strain, $\varepsilon_{fb1,2}$

There are two main resources of fabric elongation (Kovar & Gupta, 2009): yarn straightening (de-crimp) and yarn axial elongation. For principal direction it will be assumed

that all yarns are straight ($c_{1,2} = 0$) and then are broken at breaking strain $\varepsilon_{1,2b}$. So fabric breaking strain can be determined by

$$\varepsilon_{fb1,2} = (1 + \varepsilon_{1,2b})(1 + c_{1,2b}) - 1 \quad (3.5)$$

c. Fabric width

Fabric elongation in principal directions is attached with straightening (de-crimping) of the yarns imposed load, whereas opposite yarns crimp amplitude increases and fabric contracts. We shall assume that lateral contraction is similar as elongation in lateral direction. Original width of the sample b_o will be changed into $b_{b1,2}$ (at breaking) :

$$b_{b1,2} = \frac{b_o}{1 + \varepsilon_{fb1,2}} \quad (3.6)$$

d. Lateral contraction

Fabric Poisson's ratio ν can be counted using

$$\nu_{1,2} = \frac{b_o - b_{b1,2}}{b_o} = \frac{\varepsilon_{fb1,2}}{1 + \varepsilon_{fb1,2}} \quad (3.7)$$

3.2 MECHANICS OF WOVEN REINFORCED COMPOSITES

3.2.1 Mechanical properties for a thin lamina

A thin lamina is considered as a woven layer surrounded by matrix and orthotropic material (Fig. 3.4)

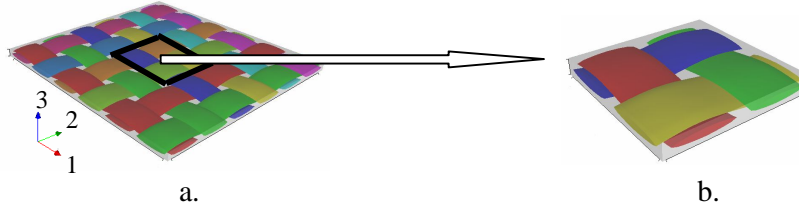


Fig. 3.4 Geometrical model: a. Lamina; b. Unit cell

As known [44], in the case of unidirectional composites, if the textile reinforced composite is to be considered as a homogeneous material it is necessary to determine some set of elastic properties which characterize an effective material, mechanically equivalent to actual material. This approach seems reasonable because the volume of material to be homogenized is small compared to the structural component to be analyzed. However, unlike the unidirectional composite, the basic representative volume element, (RVE or unit cell, Fig.

3.4) associated with textile reinforced composites is typically quite large. In such cases special analytical tools need to be developed to understand the local response within the RVE.

Various analytical techniques have been developed to predict thermo-mechanical properties of textile composite RVEs. Two models selected in this study are the mosaic model and the fiber crimp model. The mosaic model without consideration of the fiber continuity of undulation (crimp) provides a convenient and rough estimate of the thermo-elastic properties of fabric composites while the crimp model describing the actual geometry of unit cell is suitable for plain weave fabrics. These modeling techniques are carried on from averaging of mechanical properties of the constituent materials and the detailed geometric descriptions of the reinforcement. Two methods are used for every model, such as stiffness averaging method and compliance averaging method. For stiffness averaging method, the constitutive equations base upon iso-strain assumption and for compliance averaging method, the constitutive equations base upon iso-stress assumption.

Stiffness averaging method is the one of averaging methods that has attractive feature thanks to continuity of strains or displacements is maintained, although continuity of internal stresses is violated. Bogdanovich et al after comparison a variety of experimental data with various methods of prediction concluded that the stiffness averaging method provides a very good model of elastic properties.

A complementary variant on the stiffness averaging technique is the compliance averaging technique. In this case it is assumed that all components of the materials system are under constant stress. It can be seen that compliance averaging method satisfies continuity of internal stresses while violates continuity of displacements between the phases.

3.2.2 Lamination theory

A laminate is constructed by stacking and bonding a number of laminas in the thickness (z) direction (Fig. 3.5). Intuitively, one can see that the strength, stiffness, and hydrothermal properties of a laminate will depend on: elastic modules, stacking position, thickness, angle of orientation, coefficients of thermal expansion, and coefficients of moisture expansion [46, 47].

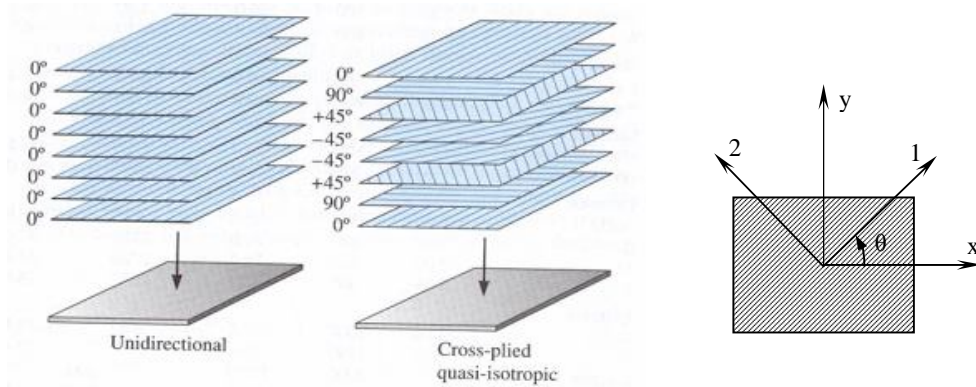


Fig. 3.5 Schematic of a laminate

Lamination theory is used to calculate:

1. Stiffness matrices for the laminate
2. Midplane strains and curvatures for the laminate due to a given set of applied forces and moments
3. In-plane strains ϵ_x , ϵ_y , and γ_{xy} for each lamina
4. In-plane stresses σ_x , σ_y , and τ_{xy} in each lamina

The geometric midplane of the laminate contains the x , y axes, and the z axis defines the thickness direction. The total thickness of the laminate is h , and the thicknesses of various laminas are represented by t_1 , t_2 , t_3 , and so on. The total number of laminas is N . The sketch for the laminate is shown in Fig. 3.6.

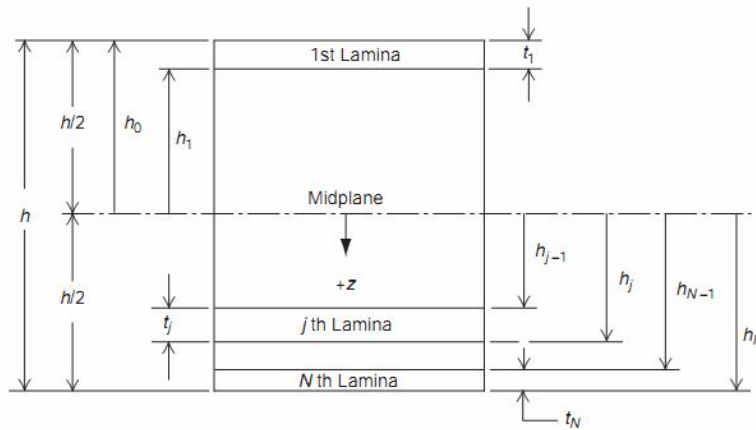


Fig. 3.6 Laminate geometry

Laminate strains are linearly related to the distance from the midplane as

$$\boldsymbol{\varepsilon} = \boldsymbol{\varepsilon}_m^o + z \cdot \mathbf{k} \quad (3.8)$$

Where

$\boldsymbol{\varepsilon} = [\varepsilon_x, \varepsilon_y, \gamma_{xy}]^T$ is vector of laminate strain at layer with the distance z from the midplane

$\boldsymbol{\varepsilon}_m^o = [\varepsilon_x^o, \varepsilon_y^o, \gamma_{xy}^o]^T$ is vector of laminate strain at midplane

$\mathbf{k} = [k_x, k_y, k_{xy}]^T$ is vector of curvatures of the laminate

Applied force and moment resultant (Fig. 3.7) on a laminate are related to the midplane strains and curvatures by the following equations:

$$\begin{bmatrix} \mathbf{N} \\ \mathbf{M} \end{bmatrix} = \begin{bmatrix} \mathbf{A} & \mathbf{B} \\ \mathbf{B} & \mathbf{D} \end{bmatrix} \cdot \begin{bmatrix} \boldsymbol{\varepsilon}_m^o \\ \mathbf{k} \end{bmatrix} \quad (3.9)$$

where

$\mathbf{N} = [N_x, N_y, N_{xy}]^T$ and $\mathbf{M} = [M_x, M_y, M_{xy}]^T$ are applied force and moment resultants

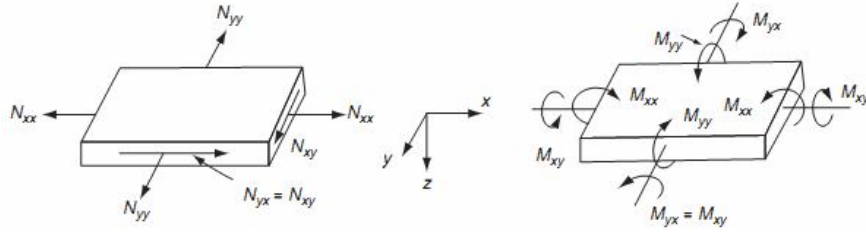


Fig. 3.7 In-plane, bending, and twisting loads applied on a laminate

\mathbf{A} , \mathbf{B} , and \mathbf{D} are extensional stiffness matrix, coupling stiffness matrix, and bending stiffness matrix for the laminate. The elements in \mathbf{A} , \mathbf{B} , and \mathbf{D} matrices are calculated from

$$A_{mn} = \sum_{j=1}^N (Q_{mn})_j (h_j - h_{j-1}) \quad (3.10a)$$

$$B_{mn} = \frac{1}{2} \sum_{j=1}^N (Q_{mn})_j (h_j^2 - h_{j-1}^2) \quad (3.10b)$$

$$D_{mn} = \frac{1}{3} \sum_{j=1}^N (Q_{mn})_j (h_j^3 - h_{j-1}^3) \quad (3.10c)$$

$$m, n = 1, 2, 6$$

Q_{mn} are determined from elements C_{mn} of equation (3.11) and angle θ of lamina orientation

$$(Q_{mn} = Q_{nm})$$

$$\begin{aligned}
Q_{11} &= C_{11} \cos^4 \theta + 2(C_{12} + 2C_{66}) \sin^2 \theta \cos^2 \theta + C_{22} \sin^4 \theta \\
Q_{12} &= C_{12} (\sin^4 \theta + \cos^4 \theta) + (C_{11} + C_{22} - 4C_{66}) \sin^2 \theta \cos^2 \theta \\
Q_{22} &= C_{11} \sin^4 \theta + 2(C_{12} + 2C_{66}) \sin^2 \theta \cos^2 \theta + C_{22} \cos^4 \theta \\
Q_{16} &= (C_{11} - C_{12} - 2C_{66}) \sin \theta \cos^3 \theta + (C_{12} - C_{22} + 2C_{66}) \sin^3 \theta \cos \theta \\
Q_{26} &= (C_{11} - C_{12} - 2C_{66}) \sin^3 \theta \cos \theta + (C_{12} - C_{22} + 2C_{66}) \sin \theta \cos^3 \theta \\
Q_{66} &= (C_{11} + C_{22} - 2C_{12} - 2C_{66}) \sin^2 \theta \cos^2 \theta + C_{66} (\sin^4 \theta + \cos^4 \theta)
\end{aligned} \tag{3.11}$$

3.2.2 Lamination theory including transverse shear stresses

Consider a plate in the (x, y) -plane and assume that all loads are normal to its surface (Fig. 3.8). If the deflections are small in comparison with the thickness of the plate, the following equations can be obtained [48].

$$\frac{\partial Q_x}{\partial x} + \frac{\partial Q_y}{\partial y} + p = 0 \quad ; \quad \frac{\partial M_{xy}}{\partial x} + \frac{\partial M_y}{\partial y} - Q_y = 0 \quad ; \quad \frac{\partial M_{yx}}{\partial y} + \frac{\partial M_x}{\partial x} - Q_x = 0 \tag{3.12}$$

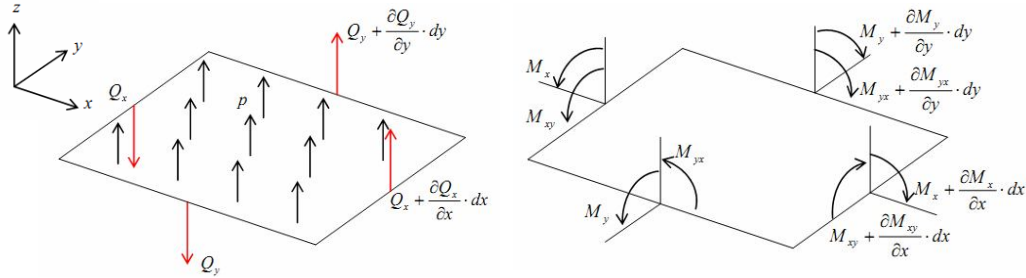


Fig. 3.8 Plate under lateral loading

When only forces in the x -direction are considered without gradients the y -direction ($Q_y = 0$ and $\partial/\partial y = 0$ for all response variables) this reduces to the following two equations:

$$\frac{\partial Q_x}{\partial x} = -p \quad ; \quad \frac{\partial M_x}{\partial x} = Q_x \tag{3.13}$$

The forces and moments acting on the plate cause internal stresses. Now consider an element with dimensions dx, dy, dz . The equilibrium of forces gives the following equations:

$$\frac{\partial \sigma_x}{\partial x} + \frac{\partial \tau_{xy}}{\partial y} + \frac{\partial \tau_{xz}}{\partial z} = 0 \quad ; \quad \frac{\partial \tau_{yx}}{\partial x} + \frac{\partial \sigma_y}{\partial y} + \frac{\partial \tau_{yz}}{\partial z} = 0 \quad ; \quad \frac{\partial \tau_{zx}}{\partial x} + \frac{\partial \tau_{zy}}{\partial y} + \frac{\partial \sigma_z}{\partial z} = 0 \tag{3.14}$$

Equilibrium of moments, neglecting the higher order terms, results in:

$$\tau_{xy} = \tau_{yx} ; \tau_{yz} = \tau_{zy} ; \tau_{zx} = \tau_{xz} \quad (3.15)$$

When only stress gradients in the x-direction and the z-direction are considered ($\partial/\partial y = 0$ for all response variables), this reduces to the following three equations:

$$\frac{\partial \sigma_x}{\partial x} + \frac{\partial \tau_{xz}}{\partial z} = 0 ; \frac{\partial \tau_{xy}}{\partial x} + \frac{\partial \tau_{yz}}{\partial z} = 0 ; \frac{\partial \tau_{xz}}{\partial x} + \frac{\partial \sigma_z}{\partial z} = 0 \quad (3.16)$$

The magnitude of the shearing forces can be calculated with:

$$Q_x = \int_{-h/2}^{h/2} \tau_{xz} dz ; Q_y = \int_{-h/2}^{h/2} \tau_{yz} dz \quad (3.17)$$

Assuming that a short thin beam is loaded like figure 3.9, let us consider the short thin beam as a plate bending in the (x, z)-plane. It can deduce

$$N_x = N_y = N_{xy} = Q_y = M_y = M_{xy} = 0 \quad (3.18)$$

Substituting (3.22) into (3.13), we obtain:

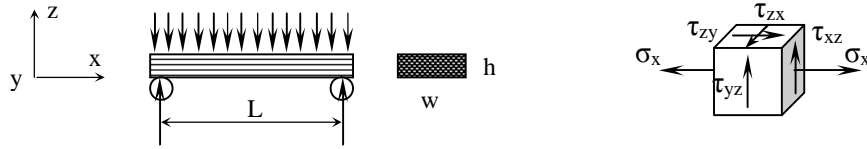


Fig. 3.9 Bending of a short thin beam and stress state of element

$$\begin{Bmatrix} 0 \\ 0 \\ 0 \\ M_x \\ 0 \\ 0 \end{Bmatrix} = \begin{bmatrix} A_{11} & A_{12} & A_{16} & B_{11} & B_{12} & B_{16} \\ A_{21} & A_{22} & A_{26} & B_{21} & B_{22} & B_{26} \\ A_{61} & A_{62} & A_{66} & B_{61} & B_{62} & B_{66} \\ B_{11} & B_{12} & B_{16} & D_{11} & D_{12} & D_{16} \\ B_{21} & B_{22} & B_{26} & D_{21} & D_{22} & D_{26} \\ B_{61} & B_{62} & B_{66} & D_{61} & D_{62} & D_{66} \end{bmatrix} \cdot \begin{Bmatrix} \varepsilon_x^o \\ \varepsilon_y^o \\ \gamma_{xy}^o \\ k_x \\ k_y \\ k_{xy} \end{Bmatrix} \quad (3.19)$$

Inversion of the **ABD**-matrix, here denoted as **abd** with components a_{ij} , b_{ij} , and d_{ij} , gives the strains and curvatures as a function of M_x . From that, the in-plane strains and stresses can be calculated in the global coordinate system (at any location through the thickness):

$$\begin{Bmatrix} \varepsilon_x \\ \varepsilon_y \\ \gamma_{xy} \end{Bmatrix} = \begin{Bmatrix} b_{11} + d_{11} \cdot z \\ b_{21} + d_{21} \cdot z \\ b_{61} + d_{61} \cdot z \end{Bmatrix} \cdot M_x ; \quad \begin{Bmatrix} \sigma_x \\ \sigma_y \\ \tau_{xy} \end{Bmatrix}_{(k)} = [\mathbf{Q}]_{(k)} \cdot \begin{Bmatrix} \varepsilon_x \\ \varepsilon_y \\ \gamma_{xy} \end{Bmatrix} \quad (3.20)$$

The through-thickness lateral shear stresses can be calculated by combining (3.16), (3.17), and (3.20).

$$\left(\frac{\partial \tau_{xz}}{\partial z}\right)_{(k)} = -\left[Q_{11(k)} \cdot (b_{11} + d_{11} \cdot z) + Q_{12(k)} \cdot (b_{21} + d_{21} \cdot z) + Q_{16(k)} \cdot (b_{61} + d_{61} \cdot z)\right] \cdot Q_x$$

$$\left(\frac{\partial \tau_{yz}}{\partial z}\right)_{(k)} = -\left[Q_{61(k)} \cdot (b_{11} + d_{11} \cdot z) + Q_{62(k)} \cdot (b_{21} + d_{21} \cdot z) + Q_{66(k)} \cdot (b_{61} + d_{61} \cdot z)\right] \cdot Q_x$$

With the boundary condition of zero shear stresses at the outer surface, one can deduce:

$$\tau_{xz}^{(k)} = \sum_{j=1}^{k-1} \int_{z_{j-1}}^{z_j} \left(\frac{\partial \tau_{xz}}{\partial z}\right)_{(j)} \cdot dz + \int_{z_{k-1}}^z \left(\frac{\partial \tau_{xz}}{\partial z}\right)_{(k)} \cdot dz \quad ; \quad \tau_{yz}^{(k)} = \sum_{j=1}^{k-1} \int_{z_{j-1}}^{z_j} \left(\frac{\partial \tau_{yz}}{\partial z}\right)_{(j)} \cdot dz + \int_{z_{k-1}}^z \left(\frac{\partial \tau_{yz}}{\partial z}\right)_{(k)} \cdot dz$$

Integration of these equations results in:

$$\begin{aligned} \tau_{xz}^{(k)} = & \\ & -\sum_{j=1}^{k-1} \left[\left(Q_{11(j)} \cdot b_{11} + Q_{12(j)} \cdot b_{21} + Q_{16(j)} \cdot b_{61} \right) \cdot (z_j - z_{j-1}) + \frac{1}{2} \left(Q_{11(j)} \cdot d_{11} + Q_{12(j)} \cdot d_{21} + Q_{16(j)} \cdot d_{61} \right) \cdot (z_j^2 - z_{j-1}^2) \right] \cdot Q_x \\ & - \left[\left(Q_{11(j)} \cdot b_{11} + Q_{12(j)} \cdot b_{21} + Q_{16(j)} \cdot b_{61} \right) \cdot (z - z_{k-1}) + \frac{1}{2} \left(Q_{11(j)} \cdot d_{11} + Q_{12(j)} \cdot d_{21} + Q_{16(j)} \cdot d_{61} \right) \cdot (z^2 - z_{k-1}^2) \right] \cdot Q_x \\ \tau_{yz}^{(k)} = & \end{aligned} \quad (3.21)$$

$$\begin{aligned} & -\sum_{j=1}^{k-1} \left[\left(Q_{61(j)} \cdot b_{11} + Q_{62(j)} \cdot b_{21} + Q_{66(j)} \cdot b_{61} \right) \cdot (z_j - z_{j-1}) + \frac{1}{2} \left(Q_{61(j)} \cdot d_{11} + Q_{62(j)} \cdot d_{21} + Q_{66(j)} \cdot d_{61} \right) \cdot (z_j^2 - z_{j-1}^2) \right] \cdot Q_x \\ & - \left[\left(Q_{61(j)} \cdot b_{11} + Q_{62(j)} \cdot b_{21} + Q_{66(j)} \cdot b_{61} \right) \cdot (z - z_{k-1}) + \frac{1}{2} \left(Q_{61(j)} \cdot d_{11} + Q_{62(j)} \cdot d_{21} + Q_{66(j)} \cdot d_{61} \right) \cdot (z^2 - z_{k-1}^2) \right] \cdot Q_x \end{aligned}$$

3.2.3 Thermal effects in a laminate

Consider a plate in the (x, y)-plane subjected by a change of temperature $\Delta T = T - T_0$, (or is called by thermal load). In such cases, thermal stresses and thermal strains arise that influence severely on laminate strengths. One of the main causes is appearance of thermal deformation mismatch between laminas as well as between matrix and the reinforcements.

The constitutive equation describing thermal behavior of the laminate can be written

$$\begin{bmatrix} N^T \\ M^T \end{bmatrix} = \begin{bmatrix} A & B \\ B & D \end{bmatrix} \cdot \begin{bmatrix} \epsilon_m^o \\ k \end{bmatrix} \quad (3.22)$$

where

N^T and M^T are thermal force and moment resultants.

$$N^T = \left\{ N_x^T, N_y^T, N_{xy}^T \right\}^T = \sum_{j=1}^N (Q_{mm})_j (\alpha_n)_j (h_j - h_{j-1}) \Delta T \quad (3.23a)$$

$$\mathbf{M}^T = \{M_x^T, M_y^T, M_{xy}^T\}^T = \sum_{j=1}^N \frac{1}{2} (Q_{mn})_j (\alpha_n)_j (h_j^2 - h_{j-1}^2) \Delta T \quad (3.23b)$$

α is vector of the coefficients of thermal expansion

3.2.4 Application of lamination theory for studied geocomposites

The case of all orthotropic laminas stacked and bonded together with the same orientation ($\theta = 0$) is considered in figure 3.10a. It can be assumed that number of laminas is $2n$, each lamina has the same thickness h and stiffness matrix \mathbf{C} . We get the coupling stiffness matrix $\mathbf{B} = 0$. The extensional stiffness matrix \mathbf{A} and the bending stiffness matrix \mathbf{D} have elements $A_{16} = A_{26} = D_{16} = D_{26} = 0$. The stiffness matrix \mathbf{Q} will be $\mathbf{Q} = \mathbf{C}$, leads to $Q_{16} = Q_{26} = 0$.

When the result laminate is only subjected force $N_x \neq 0$ (Fig. 3.10b), we derive $\boldsymbol{\varepsilon}_m^o = \mathbf{A}^{-1} \mathbf{N} = \mathbf{a} \mathbf{N}$. From that, we obtain $\varepsilon_x^o = a_{11} N_x$. Therefore, the effective elastic modulus of laminate in x direction can be determined as

$$E_x = \frac{\sigma_x}{\varepsilon_x^o} = \frac{N_x / 2nh}{\varepsilon_x^o} = \frac{1}{2nha_{11}} = \frac{1}{2nh} \cdot \frac{2nh(C_{11}C_{22} - C_{12}^2)}{C_{22}} = E_1 \quad (3.24)$$

When the result laminate is only subjected force $N_{xy} \neq 0$ (Fig. 3.10c), we derive similarly the effective shear modulus of laminate as

$$G_{xy} = \frac{\tau_{xy}}{\gamma_{xy}^o} = \frac{N_{xy} / 2nh}{\gamma_{xy}^o} = \frac{1}{2nha_{66}} = \frac{1}{2nh} \cdot 2nh \cdot C_{66} = G_{12} \quad (3.25)$$

When the result laminate is a short beam subjected flexural load $Q_x \neq 0$ (Fig. 3.9), the lateral shear stresses reduce to

$$\tau_{yz} = 0 \quad ; \quad \tau_{xz}^{(k)} = -\frac{3Q_x}{4n^3h^3} \cdot \left[\sum_{j=1}^{k-1} (z_j^2 - z_{j-1}^2) + (z^2 - z_{k-1}^2) \right] \quad (3.26)$$

where $z_{k-1} \leq z \leq z_k$; $1 < k \leq n$

When the result laminate is only subjected by thermal loads, it leads to $\mathbf{B} = \mathbf{M}^T = 0$. The equation (3.22) gives us the results that the curvatures of the laminate disappears, $\mathbf{k} = 0$, and the vector of laminate strain at midplane, $\boldsymbol{\varepsilon}_m^o$, can be counted by $\mathbf{A} \cdot \boldsymbol{\varepsilon}_m^o = \mathbf{N}^T = \mathbf{A} \cdot \boldsymbol{\alpha} \cdot \Delta T$ leads to

$$\boldsymbol{\alpha} = \frac{1}{\Delta T} \cdot \boldsymbol{\varepsilon}_m^o. \text{ This deduces to}$$

$$\alpha_x = \alpha_1 = \frac{\varepsilon_x^o}{\Delta T} ; \alpha_y = \alpha_2 = \frac{\varepsilon_y^o}{\Delta T} ; \alpha_{xy} = 0 \quad (3.27)$$

From eqns. (3.24)-(3.27), it can be included that in the case of the laminate bonded together with the same orientation ($\theta = 0$) from the orthotropic laminas the thermo-mechanical properties of the laminate are equivalent to those of every lamina.

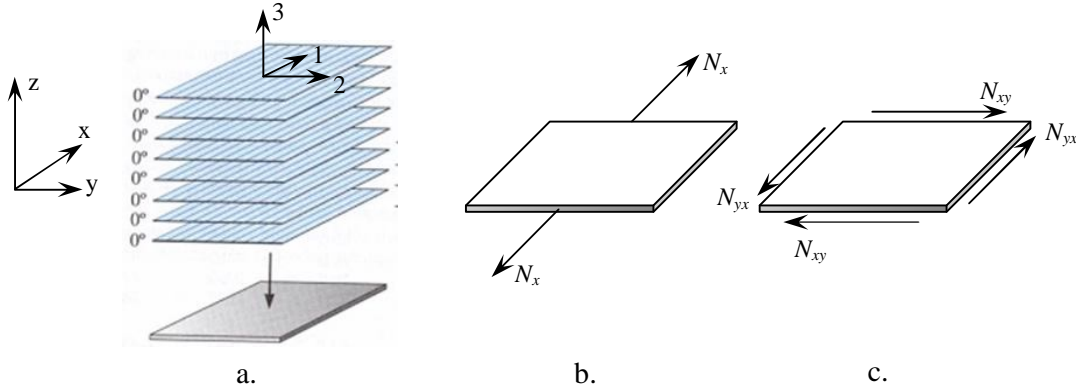


Fig. 3.10 Laminate is subjected by tensile load and shear load

3.2.5 Thermo-mechanical properties of constituents in a repeating unit cell

In order to calculate elastic properties and thermal properties of lamina reinforced with woven fabric, we need to determine elastic properties and thermal properties for a unidirectional rod (presenting a yarn and an equal volume fraction of matrix around it within a unit cell). The matrix encompassing yarns are considered isotropic material while the yarns in a unit cell are attributed orthotropic. Assuming that combination fibers and resin with a good adhesion (Fig. 3.11). Thermo-mechanical properties of yarns can be calculated by theory of unidirectional lamina micromechanics (included fraction of void volume).

The longitudinal elastic modulus

The longitudinal elastic modulus of yarn sections can be counted by the rule of mixtures:

$$E_L = E_f V_f + E_m V_m \quad (3.28)$$

where E_f , E_m are Young's modules of reinforcement fiber and matrix

V_f , V_m are volume fractions of reinforcement fiber and matrix

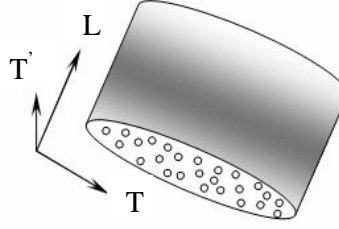


Fig. 3.11 The geometrical model of a yarn section

The transverse elastic modulus

The transverse elastic modulus, $E_T = E_{T'}$, is given by Halphin and Tsai as

$$\frac{E_T}{E_m} = \frac{1 + \xi \eta V_f}{1 - \eta V_f} \quad (3.29)$$

where

$$\eta = \frac{(E_f / E_m) - 1}{(E_f / E_m) + \xi} \quad (3.30)$$

The term ξ is called the reinforcing factor and depends on fiber geometry, packing geometry, loading conditions. For a fiber geometry of circular fibers in a packing geometry of a square array, $\xi = 2$.

The major Poisson's ratio

The equation for the major Poisson's ratio, ν_{LT} , is obtained as follows

$$\nu_{LT} = \nu_f V_f + \nu_m V_m \quad (3.31)$$

where ν_f, ν_m are Poisson's ratios of reinforcement fiber and matrix

The in-plane shear modulus

The Halphin–Tsai equation for the in-plane shear modulus, G_{LT} , is

$$\frac{G_{LT}}{G_m} = \frac{1 + \xi \eta V_f}{1 - \eta V_f} \quad (3.32)$$

where η is determined by (3.30) but ratio of E_f/E_m is replaced by G_f/G_m , with $\xi = 1$ for circular fibers in a square array; G_m is shear modulus of matrix.

Coefficients of thermal expansion (CTE)

Longitudinal and transverse thermal expansion coefficients, α_L, α_T are

$$\alpha_L = \frac{V_f \alpha_f E_f + V_m \alpha_m E_m}{V_f E_f + V_m E_m} ; \quad \alpha_T = V_f \alpha_f + V_m \alpha_m + \frac{\nu_m E_f - \nu_f E_m}{\frac{E_f}{V_m} + \frac{E_m}{V_f}} (\alpha_m - \alpha_f) \quad (3.33)$$

where α_f, α_m are thermal expansion coefficients of reinforcement fiber and matrix

In this section, we will also calculate more five ultimate strength parameters for a yarn within the unit cell from the individual properties of the fiber and matrix (Fig. 3.12). These parameters will be used to verify strength of composite subjected loads. Generally, the strength parameters for a unidirectional lamina are much harder to predict than the stiffnesses because the strengths are more sensitive to the material and geometric nonhomogeneities, fiber–matrix interface, fabrication process, and environment. For these reasons of sensitivity, some theoretical and empirical models are available for some of the strength parameters.

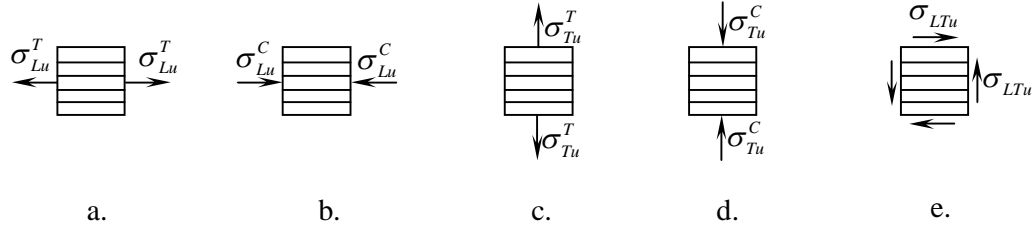


Fig. 3.12 Five ultimate strength parameters for a unidirectional lamina

Longitudinal tensile strength (Fig. 3.12a):

$$\sigma_{Lu}^T = V_f \sigma_{fu}^T + V_m \sigma_{mu}^T \quad (3.34)$$

where $\sigma_{fu}^T, \sigma_{mu}^T$ are ultimate tensile strength of fiber and matrix

Failure of a unidirectional ply under a longitudinal tensile load takes place with three failure modes: fracture of fibers, fracture of fibers with pullout, and fiber pullout with fiber–matrix debonding.

Longitudinal compressive strength (Fig. 3.12b):

Because geopolymers are very brittle, the longitudinal compressive strength can be determined by model of failure tensile strains of the matrix in the transverse direction (Fig. 3.13).

$$\sigma_{Lu}^C = \frac{E_L \varepsilon_{Tu}^T}{V_{LT}}, \quad \varepsilon_{Tu}^T = \varepsilon_{mu}^T \left[\frac{d}{s} \left(\frac{E_m}{E_f} - 1 \right) + 1 \right] \quad (3.35)$$

Where ε_{Tu}^T are the ultimate tensile strain of the unidirectional composites in transverse direction; ε_{mu}^T are the ultimate tensile strain of the matrix; d is diameter of the fibers and s is center-to-center spacing between the fibers. Fraction d/s depends on the packing geometry of fiber. For a packing geometry of a square array, ratio of d/s is

$$\frac{d}{s} = \sqrt{\frac{4V_f}{\pi}} \quad (3.36)$$

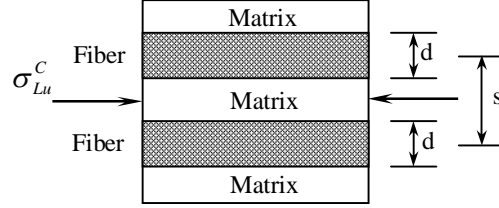


Fig. 3.13 Model of failure tensile strains of the matrix in the transverse direction

Transverse tensile strength (Fig. 3.12c):

Similarly, transverse tensile strength of a unidirectional lamina is also determined by model of failure tensile strains of the matrix in the transverse direction.

$$\sigma_{Tu}^T = E_T \varepsilon_{Tu}^T, \quad \varepsilon_{Tu}^T = \varepsilon_{mu}^T \left[\frac{d}{s} \left(\frac{E_m}{E_f} - 1 \right) + 1 \right] \quad (3.37)$$

Transverse compressive strength (Fig. 3.12d):

Equation to calculate transverse compressive strength of a unidirectional lamina is developed from (3.37).

$$\sigma_{Tu}^C = E_T \varepsilon_{Tu}^C, \quad \varepsilon_{Tu}^C = \varepsilon_{mu}^C \left[\frac{d}{s} \left(\frac{E_m}{E_f} - 1 \right) + 1 \right] \quad (3.38)$$

where ε_{Tu}^C are the ultimate transverse compressive strain of the unidirectional composites and ε_{mu}^C are the ultimate compressive strain of the matrix.

In-plane shear strength (Fig. 3.12e):

Equation to calculate in-plane shear strength of a unidirectional lamina is also formed similarly as equations (3.37), (3.38).

$$\sigma_{LTu} = G_{LT} \gamma_{LTu}, \quad \gamma_{LTu} = \gamma_{mu} \left[\frac{d}{s} \left(\frac{G_m}{G_f} - 1 \right) + 1 \right] = \frac{\tau_{mu}}{G_m} \cdot \left[\frac{d}{s} \left(\frac{G_m}{G_f} - 1 \right) + 1 \right] \quad (3.39)$$

where γ_{LTu} are the ultimate shear strain of the unidirectional composites; γ_{mu} are the ultimate shear strain of the matrix; τ_{mu} are the shear strength of the matrix and can be counted by (3.40).

$$\tau_{mu} = \frac{\sigma_{mu}^T \cdot \sigma_{mu}^C}{\sigma_{mu}^T + \sigma_{mu}^C} \quad (3.40)$$

where σ_{mu}^T , σ_{mu}^C are tensile and compressive strengths of matrix.

In the end of subsection, a failure criterion are needed to select in order to predict the strengths of unit cell, which means to predict the strengths of composites reinforced by woven fabric. There are many failure criteria applied for composite materials such as: maximum stress failure criterion, maximum strain failure criterion, Tsai-Hill failure criterion, Hoffman failure criterion, Tsai-Wu failure criterion but among that criteria the Tsai-Wu failure criterion is prominent with lots of advantages. Firstly, interaction between the strength parameters is treated instead of separate criteria for failure like maximum stress or maximum strain failure criteria. Secondly, a single failure criterion is used in all values of stresses (both positive and negative values) instead of we must distinguish to choose strength in tension or in compression like Tsai-Hill failure criterion. Thirdly, Tsai-Wu failure criterion is more general than Hoffman failure criterion by a choice of parameter F_{12} . It can be said that Tsai-Wu failure criterion is the one of criteria that agrees with experiments best and will be used in this research.

Tsai-Wu failure criterion

Tsai-Wu failure criterion in a simple form can be written as

$$F_1 \sigma_L + F_2 \sigma_T + F_{11} \sigma_L^2 + F_{22} \sigma_T^2 + F_{66} \sigma_{LT}^2 + 2F_{12} \sigma_L \sigma_T = 1 \quad (3.41)$$

where $F_1, F_2, F_{11}, F_{22}, F_{66}, F_{12}$ are determined by equations

$$F_1 = \frac{1}{\sigma_{Lu}^T} - \frac{1}{\sigma_{Lu}^C} ; F_2 = \frac{1}{\sigma_{Tu}^T} - \frac{1}{\sigma_{Tu}^C} ; F_{11} = \frac{1}{\sigma_{Lu}^T \sigma_{Lu}^C} ; F_{22} = \frac{1}{\sigma_{Tu}^T \sigma_{Tu}^C} ; F_{66} = \frac{1}{\sigma_{LTu}^2}$$

$$F_{12} = -\frac{1}{2(\sigma_{Lu}^T)^2} \quad (\text{Tsai-Hill}) ; F_{12} = -\frac{1}{2\sigma_{Lu}^T \sigma_{Lu}^C} \quad (\text{Tsai-Hill}) \quad (3.42)$$

$$F_{12} = -\frac{1}{2} \sqrt{\frac{1}{\sigma_{Lu}^T \cdot \sigma_{Lu}^C \cdot \sigma_{Tu}^T \cdot \sigma_{Tu}^C}} \quad (\text{Mises-Hencky})$$

Chapter 4

EXPERIMENTS AND MATERIAL PARAMETER IDENTIFICATION

4.1 INTRODUCTION

In this chapter, essential properties of geopolymer matrices and fiber reinforcements which considered as initial materials for geocomposites are presented. Many micro-cracks in cured matrices as natural defects of inorganic matrix are shown by SEM images. The properties of commercial textiles evaluated at real conditions and after high temperature exposing are exhibited as well. Finally, mechanical properties of result geocomposites are tested in different load conditions as well as fire-resistant properties of geocomposites are accounted for especially.

4.2 EXPERIMENTAL EQUIPMENTS

4.2.1 Universal testing machine TIRA test 2810

The TIRA test 2810 machine (Fig. 4.1) can be used for tension tests with a high level of technology, accuracy and exact measuring results in the shortest time. The maximum of loading is applied up to 10kN. The machine is controlled by either the remote control unit EDC60/120 box or the “PC-control” mode using the “TIRA test” software.

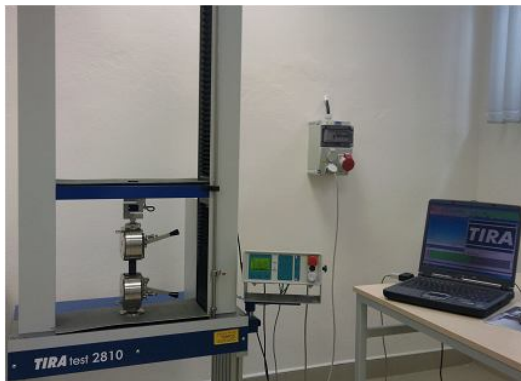


Fig. 4.1 Universal testing machine TIRA test 2810



Fig. 4.2 Universal testing machine INSTRON Model 4202

4.2.2 Universal testing machine INSTRON Model 4202

All samples needed to measure mechanical properties in bending are tested on Universal Testing Machine INSTRON Model 4202 (maximum load of the sensor: 10 kN) (Fig. 4.2). The machine is also controlled by either the remote control unit box or the PC.

4.2.3 System Q-400 digital cameras Dantec Dynamics

The Digital Image Correlation System is an optical instrument for full-field, non-contact and three-dimensional measurement of deformations and strains on components and materials. We use the system with two high resolution digital cameras (Fig. 4.3) to record surface changes of the object under investigation while loaded. The recorded images are analyzed and compared by a special correlation technique which allows the determination of the surface displacements with high local resolution. The measuring principle of the Q-400 system is based on digital image correlation.

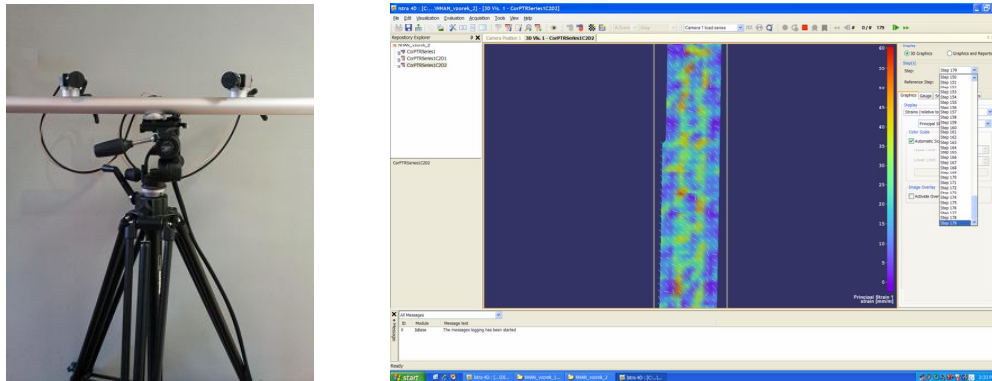


Fig. 4.3 Digital cameras and main window of Istra 4D software

4.2.4 System of TESCAN VEGA 3XM microscope and optical microscope NIKON EPIPHOT 200

Scanning electron microscope (SEM) and Energy Dispersive X-ray Analysis (EDX) on TESCAN VEGA 3XM micro are used to analysis the structure and chemical compositions of geopolymers resin (Fig. 4.4a). Examination of the geopolymer material was made on the SEM with the dispersive radiation spectrometer at the maximum magnification of 2500x, using the secondary electron detection, and the Esprit 1.8 software, using 30 kV acceleration voltages. In addition, geocomposite samples are also investigated about the adhesion between

matrix and fibers on optical microscope NIKON EPIPHOT 200 (macroscopic observation) and used the software NIS Elements to take pictures (Fig. 4.4b).



Fig. 4.4 a. System of TESCAN VEGA 3XM Microscope; b. System of optical microscope NIKON EPIPHOT 200

4.2.5 System of vacuum bagging and drying furnace; Heating oven

All geopolymer and geocomposite samples will be cured by vacuum bagging system and drying furnace ED23 (Fig. 4.5a). A membrane vacuum pump N810.3FT.18 with capacity of 10 liter/min. and low vacuum pressure of 100 kPa is used in the vacuum bagging system. The drying furnace can control curing time and temperature. Heating oven is used to heat samples at desired curing time at desired elevated temperature.

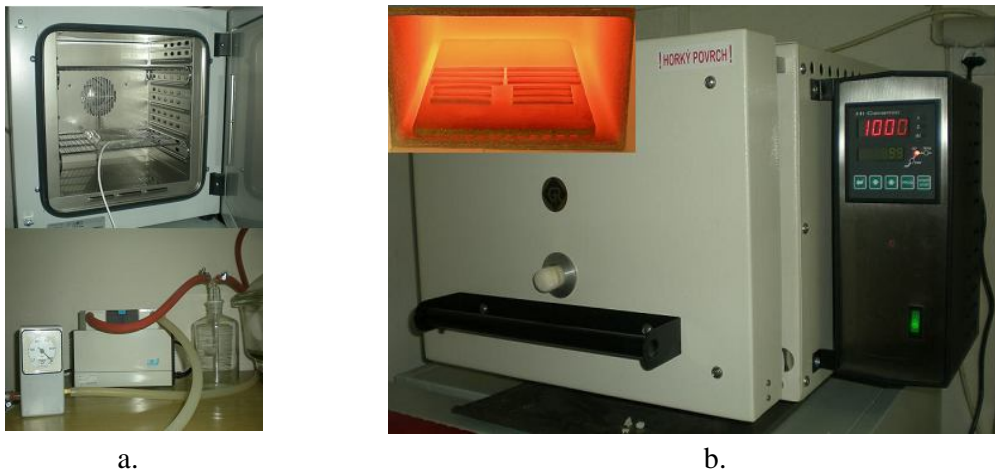


Fig. 4.5 a. System of vacuum bagging and drying furnace ED23; b. Heating oven

4.2.6 System of thermal conductivity NETZSCH model LFA 447 NanoFlash

Thermal conductivity of materials are determined by the thermal diffusivity and specific heat of them. The thermal diffusivity and specific heat are measured using a NETZSCH model LFA 447 NanoFlash® diffusivity apparatus (Fig. 4.6). The unit used in this work is equipped with a furnace, capable of operation from 25 to 300 °C. The system is equipped with a software-controlled automatic sample changer allowing measurement of up to 4 samples at the same time. The temperature rise on the back face of the sample is measured using an InSb detector. Data acquisition and evaluation are accomplished using a comprehensive 32-Bit MS®-Windows™ software package. Various analysis models are integrated in the software. The data can be corrected for finite pulse and (2-dimensional) heat loss effects. The data evaluation software also allows 2- and 3-layer calculations as well as the evaluation of the contact resistance. The instrument is designed to carry out tests fully automatically. The LFA 447 operates in accordance with national and international standards such as ASTM E-1461



Fig. 4.6 System of thermal conductivity NETZSCH model LFA 447 NanoFlash

4.3 GEOPOLYMER RESIN

4.3.1 Specimen preparation

Geopolymer binder were prepared by mixing of 49% alumino-silicate powder namely FC4, 44.12% alkali activator containing NaOH/KOH and 6.88% metakaolin powder namely M4 in mass. Geopolymer were provided by *Research Institute of Inorganic Chemistry, Inc., Ústí nad Labem, Czech Republic*.

Procedure of preparation of geopolymer resin can be described in figure 4.7.

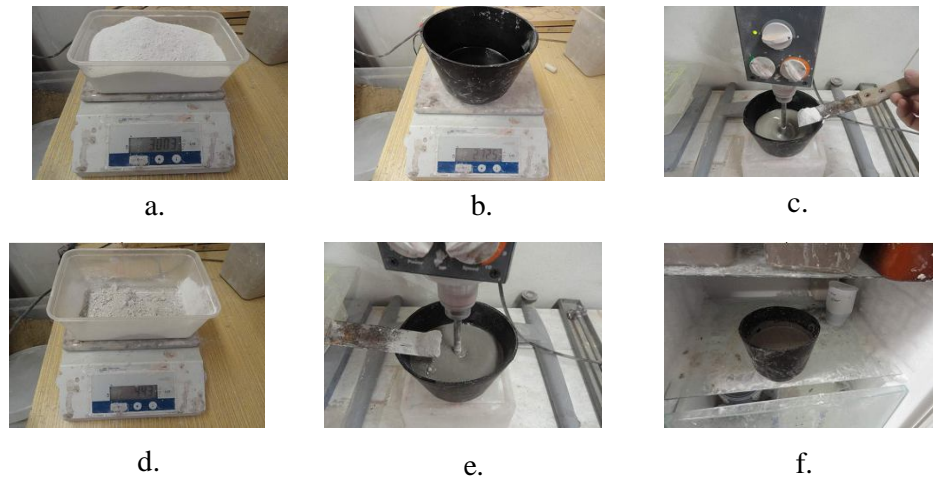


Fig. 4.7 Preparation of geopolymer resin

First of all, the masses of FC4 powder, activator solution, and M4 powder are prepared (Fig. 4.7a, b, d). Then FC4 powder is dropped in the solution. The combination is stirred for 25 minutes by machine in order to generate a completely homogeneous mixture (Fig. 4.7c). Continuously, M4 powder is added to mixture and is stirred until homogeneous mixture is achieved (Fig. 4.7e). After that, we put the mixture in a refrigerator for 24 hours (Fig. 4.7f). Energy-dispersive X-ray spectroscopy (EDX) is used for elemental analysis in a mixture (Fig. 4.8). Table 4.1 shows percentages of chemical elements in resin, corresponds to a Si/Al $\gg 3$, that is poly(sialate-multisiloso).

Table 4.1 Percentages of chemical elements in geopolymers

Elements	Al	Si	P	K	Zr	Na	Ca	O
Percentages (%)	2.04	31.80	0.08	15.15	1.76	0.63	0.24	48.32

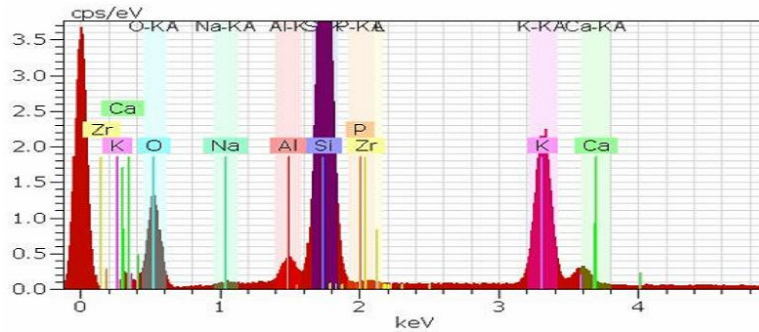


Fig. 4.8 EDX spectrum of geopolymer mixture

For rough estimating of mechanical properties of bare matrix, the bars approximately (15×15×100) mm are prepared for flexural experiment by molding, cured for 1 hour at room conditions (temperature about 20 ± 2 °C and relative humidity 65%), and then cured at 70°C for 10 hours. The sample bars are tested under three-point bending at 80mm of span; the rest samples are properly cut and tested for compression in accordance with ASTM D790(3), (Fig. 4.9a, b). The deflection rate of 2 mm/min is used for both tests.

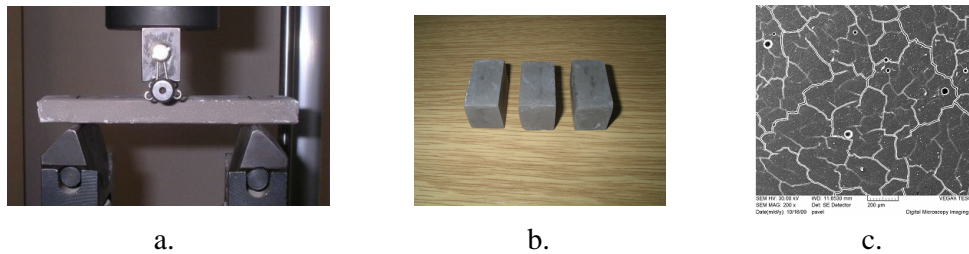


Fig. 4.9 Geopolymer specimens: a. for bending; b. for compressions; c. SEM images

Scanning Electron Microscope (SEM) images of geopolymer matrices show that there are a lot of micro-cracks in side the geopolymer matrix with the maximal width ranging around 2 μm and the length of the micro-cracks may sketch for hundreds of micrometers (Fig. 4.9c). The micro-cracks are determined as inborn defects of inorganic matrix.

4.3.2 Experimental results

Table 4.2 shows some basic physical properties of pure matrix. These materials present quite low density, ranging approximately around 2 g/cm^3 , in comparison with

traditional materials. However, without aggregates or reinforcements the bulk volume shrinkage of pure geopolymer matrix is quite high, about 15%.

Table 4.2 Density and bulk volume shrinkage of pure geopolymer matrix

Density (g/cm ³)	Bulk volume shrinkage (%)
2.01 ± 0.05	15.5 ± 0.8

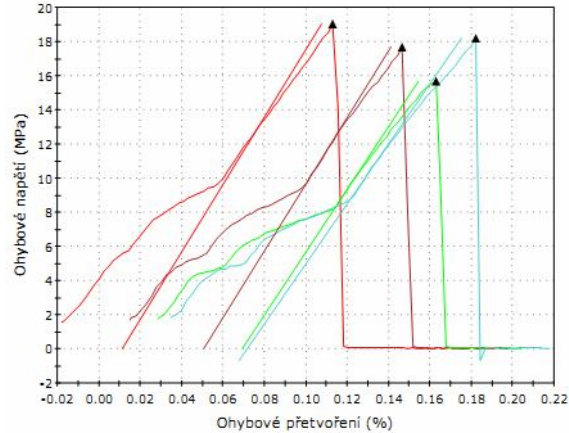


Fig. 4.10 Typical stress vs. strain curves in flexure of geopolymers at span 80 mm

Fig. 4.10 presents the typical stress vs. strain curve in flexure of geopolymers. Observation of flexural cures we can realize that nonlinear behaviors occur at the beginning of tests, that can be attributed brittle nature of material leads to deformation appearance on specimen surfaces at supports. After that, linear behaviors appear until failure of specimens. Generally, similar to other brittle materials geopolymer has bending capacity rather badly. Table 4.3 presents the flexural properties of geopolymer in accordance with different spans of testing. We can see that the properties are dependent on the used span for testing. Because there are a lot of micro-cracks in side the matrices, so when testing at high span it seem there are more changes for fracture, some samples are not broken at the middle. At lower spans, the matrices show nearly the same strength but very different modulus (see Table 4.3).

Table 4.3 The flexural properties of geopolymer

Span of testing								
40 mm			80 mm			120 mm		
R_{mf} [MPa]	E [GPa]	ε_{mf} [%]	R_{mf} [MPa]	E [GPa]	ε_{mf} [%]	R_{mf} [MPa]	E [GPa]	ε_{mf} [%]
26.3	5.4	0.84	27.8	18.5	0.44	16.6	25.7	0.16

Typical diagram of compressive tests of pure geopolymer matrices is shown in Fig. 4.11. The compressive properties of bare matrices are shown in Table 4.4.

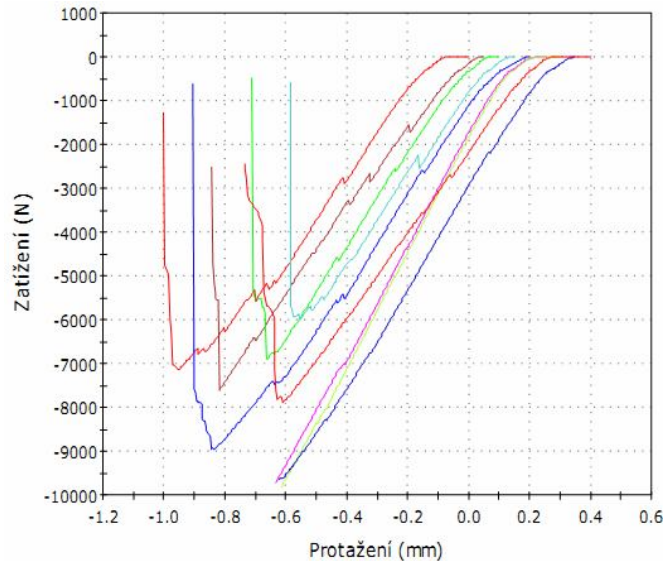


Fig. 4.11 Typical load vs. displacement curve of compressive test of geopolymer

Table 4.4 The compressive properties of geopolymer

R_{mc} [MPa]	E_{mc} [GPa]	ϵ_{mc} [%]
88.9	11.7	3.23

As can be seen from figure 4.11 that there is a quite wide region at the beginning of loading where the materials behave as fitting solid structure and can be called “toe” regions. There are a lot of partial fractures in specimens during the test and geopolymers present very typical behavior of brittle materials when non plastic, hardening regions are determined.

4.4 WOVEN FABRIC REINFORCEMENTS

4.4.1 Overviews

Woven fabrics are the most commonly used textile system for composite applications because the mechanical properties of textiles are more balanced than unidirectional fiber system and technical processes using woven fabric as reinforcement in making composites handle easily and applied for all fields of industries [49]. Now, many fabric kinds of reinforcements are now available, some special ones designed for a particular matrix system

and application. In this research, three kinds of woven fabric like as reinforcements are selected from fibers Carbon, E-glass, Basalt (Fig. 4.12). Physical properties and prices of fabric are shown in Table 4.5.

Table 4.5 Characteristics of reinforced fabrics

Fabrics	Model	Density [g/m ²]	Thickness [mm]	Pitch of [mm]		Price [kč/m ²]	Producers
				warp yarn	weft yarn		
Carbon	plain	200	0.24	2.0	2.0	825	http://www.havel-composites.com
E-glass	plain	486	0.38	2.7	2.3	96	http://www.havel-composites.com
Basalt	plain	200	0.16	1.9	1.9	252	http://www.havel-composites.com

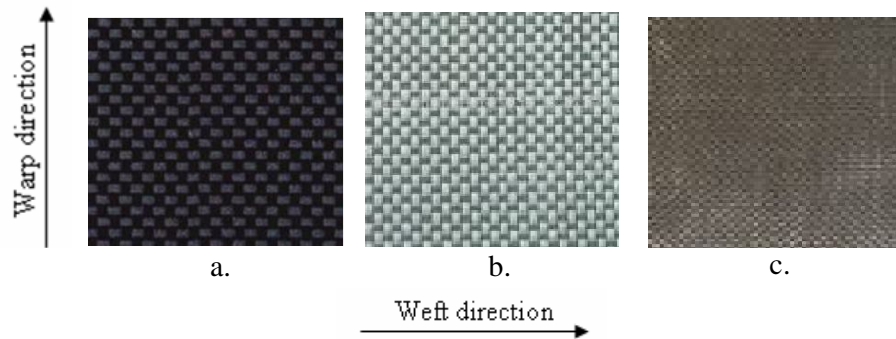


Fig. 4.12 Woven cloths: a. Carbon; b. E-glass; c. Basalt

Carbon fabrics are very expensive because it has many advantages such as light-weight, very high elastic modulus and strength, very low coefficient of linear thermal expansion, high fatigue resistance. However, the disadvantages of them are low impact resistance and high electrical conductivity.

Opposite to carbon fabric, E-glass weaves are nearly nine times cheaper combined with rather good mechanical properties, nonconductive, good resistance to hydrolysis, high chemical resistance, and excellent thermal insulation properties. The biggest drawbacks are the relatively low modulus of elasticity and high density, relatively low fatigue resistance.

Basalt fibers are inorganic fibers made from molten basalt rock. Thanks to its excellent thermo-mechanical properties, basalt textiles are widely used for places that exposure of heat. Besides that, basalt fabrics have also abilities of sound or chemical isolation.

Similar to carbon fabrics, basalt textiles have light-weight, thin thickness but cheaper more three times.

4.4.2 Experiments and identification of mechanical properties of fabrics

Tensile properties of fibers are the average values reported by the fiber manufacturers. Test method is the single filament test and values of the strength and the elastic modulus of fibers are very high. Tensile stress–strain diagrams obtained from single filament test of reinforcing fibers in use are almost linear up to the point of failure, as shown in Figure 4.13. They also exhibit very low strain-to-failure and a brittle failure mode. Although the absence of yielding does not reduce the load-carrying capacity of the fibers, it does make them prone to damage during handling as well as during contact with other surfaces. The high tensile strengths of the reinforcing fibers are generally attributed to their filamentary form in which there are statistically fewer surface flaws than in the bulk form [49].

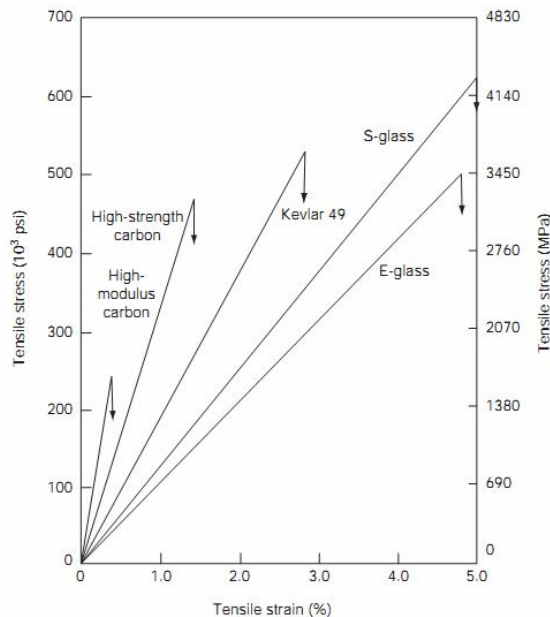


Fig. 4.13 Tensile stress-strain diagrams for various reinforcing fibers

However, tensile properties and behavior of a single fiber or a bundle do not match those of fabric. The tensile diagram of a filament is almost linear up to the point of failure while the tensile curve of fabric is surely nonlinear because all fibers in fabric can not rupture at the time. The weaker filaments in some bundles fail at low stress, and the surviving

filaments continue to carry the tensile load, however, the stress in each surviving filament becomes higher. Some of them fail as the load is increased. After the maximum stress is reached, the remaining surviving filaments continue to carry even higher stresses and start to fail, but not all at one time, thus giving the progressive failure mode. Besides that, one important reason for their lower tensile properties of fabrics is the presence of fiber undulation in woven fabrics as the fiber yarns in the fill (or weft) direction cross over and under the fiber yarns in the warp direction to create an interlocked structure. Another factor to consider is that the fibers in woven fabrics are subjected to additional mechanical handling during the weaving process, which tends to reduce their tensile strength [49]. Therefore, with a goal of estimation of result composite properties, it had better to make the tensile test for fiber fabric.

Fabric samples for tensile testing were cut in warp and weft directions with dimensions according to EN ISO 13934 [52]. Tensile region of samples has 60 mm wide, 120 mm long. The thicknesses are 0.24 mm for carbon textile, 0.38 mm for E-glass textile, 0.16 mm for basalt textile. Two ends of samples were spread geopolymer resin with the purpose of hardening them to grip more easily. The samples were fixed by two special grips inserted rubber pads to protect fabrics from tearing. All samples were tested on Universal testing machine TIRA test 2810 with a rate of 1 mm/min. Figure 4.14a presents carbon fabric sample under tension load and figure 4.14b, c shows tension diagram of fabrics. Table 4.6 shows mechanical properties of carbon, E-glass, and basalt fabrics in warp and weft directions.

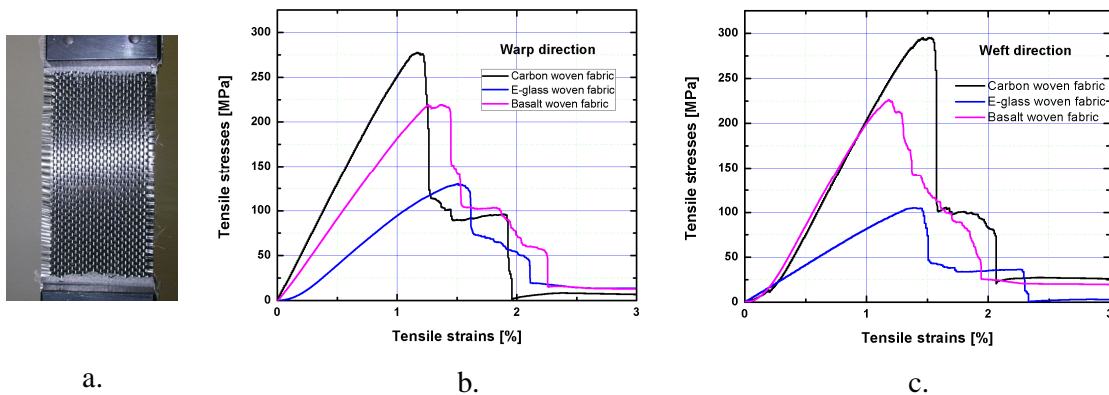


Fig. 4.14 a. Carbon woven fabric sample in tension; b, c. Tensile diagram of fabrics

We can see that stretch properties of carbon and basalt textiles in warp and weft directions are nearly equivalent each other while they are completely different for E-glass textiles. Observing textile structures, we can see also that spaces of warp and weft bundles in carbon and basalt fabrics are approximately the same while they are quite different for E-glass fabric (Fig. 4.15). Thus, the experimental results are fairly consistent with the fact.

Table 4.6 Mechanical properties of carbon, E-glass, and basalt fabrics

Fabrics	Mechanical properties in a warp direction			Mechanical properties in a weft direction		
	R_{mt} [MPa]	E [GPa]	ϵ_{mt} [%]	R_{mt} [MPa]	E [GPa]	ϵ_{mt} [%]
Carbon	282.2	25.1	1.32	288.6	25.3	1.18
E-glass	129.8	19.6	1.51	104.6	16.4	1.43
Basalt	219.4	24.2	1.26	224.6	23.2	1.21

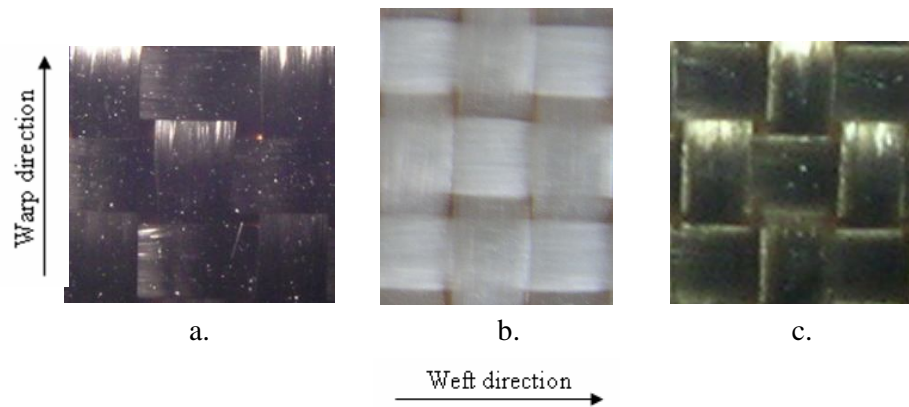


Fig. 4.15 Structure of woven textile: a. Carbon b. E-glass c. Basalt

Hung T.D et al investigated mechanical properties of commercial single fiber filaments of origin and after exposing to high temperature tested at real ambient conditions, in accordance with JIS R 7601 at gauge length 25 mm summed up in the Table 4.7.

Three kinds of fiber used in three woven fabrics are highlighted in Table 4.7. From that, we can show out two ideas. Firstly, as noted above, tensile material parameters of filaments are much higher than those of fabrics in ambient condition. Thus, the mechanical properties of geocomposites should be calculated on tensile material parameters of fabrics and matrix. This is why we conducted experiments measuring mechanical properties of the fabrics. Secondly, after 3 hours sustained at different levels of temperature (200 °C, 400 °C, 700 °C, and 1000 °C), mechanical properties of most fibers reduce. Carbon and basalt fibers

are destroyed until 700 °C while E-glass fiber retains strength after exposing up to 700 °C.

Table 4.7 Mechanical properties of filaments in accordance with Japanese Industrial Standard (JIS R 7601)

Fiber	d ₀	20 °C			200 °C			400 °C			700 °C			1000 °C		
		ε	R _{mt}	E	ε _{mt}	R _{mt}	E	ε _{mt}	R _{mt}	E	ε _{mt}	R _{mt}	E	ε _{mt}	R _{mt}	E
	[μm]	[%]	[MPa]	[GPa]	[%]	[MPa]	[GPa]	[%]	[MPa]	[GPa]	[%]	[MPa]	[GPa]	[%]	[MPa]	[GPa]
Carbon HTS 5631 800tex 12K	7	1.75	3120	178	1.72	3120	181	2.24	3640	163	Fibers were destroyed totally (nearly disappeared)					
Carbon HTS 5631 1600tex 24K	7	1.84	3120	170	1.33	2340	176	1.66	2861	172						
ARG 2400tex	27	3.32	1293	39	3.22	1241	39	1.63	769	47	The fibers still remained in the furnace, but too brittle (*)					
ARG 2500tex	14	2.68	1560	58	2.24	1820	81	0.63	390	62						
Basalt BCF13 - 2520tex - KV12 Int	13	3.98	2563	64	3.44	2111	61	1.7	1281	75						
E-glass	24	4.72	1504	32	3.26	1106	34	2.08	995	48	1.03	575	56	(*)		
Ceramic 3M-312 fiber	10	1.48	1995	140	2.06	2378	128	1.36	1745	117	1.39	1818	123	0.82	1161	99.7

4.5 GEOCOMPOSITES

4.5.1 Fabrication of geocomposite samples

Sample was prepared by the hand lay-up technique. Each of fabric was manually filled with geopolymer matrix, stacked together in the same direction, pressed by a handing roller, and we repeat process like that until to achieve desired thickness. Continuously, the sample were placed in a vacuum bag and dried using techniques known as "pressing a vacuum" (-1atm at ambient temperature 20 °C) for 2 hours. The bag was placed in a drying furnace at 80 °C and 0.3 MPa pressure for a period of 2 hours. After that, the bag was removed from the sample and then the samples were still dried for 20 hours at the same condition. Finally, the samples were cut using of vibration blade. (see Fig. 4.16a, b, c, d, e, f).

4.5.2 Volume fractions of fibers and voids in geocomposites

Generally, percentages of fibers and pore appearance in result composites influence strongly on mechanical properties of composites which get better with increasing fiber volume and get worse if rising number of voids. So, in a research, author attempt to estimate volume fractions of fibers and voids present in composite. With composite combined to organic matrix, the cured resin is burn off from a small test sample or dissolved away in a suitable liquid medium and then the fiber weight fraction is determined by comparing the

weights of the test sample before and after the removal of the matrix. But for composite coated by geopolymer it can not ignite nor dissolve away matrix. Here, it is possible to determine volume ratios of fibers, voids, and matrices by formulae as follow.

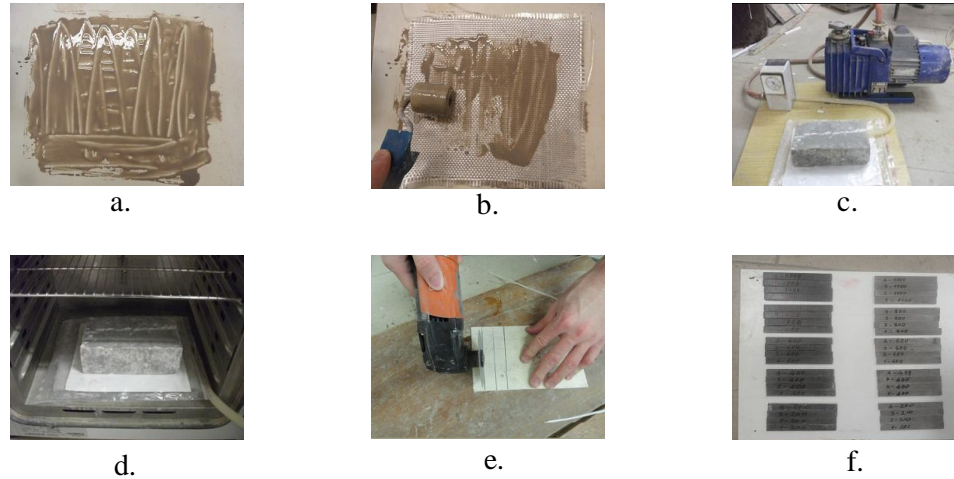


Fig. 4.16 Process for the preparation of test samples

$$V_f = \frac{n\rho_w}{t\rho_f} \cdot 100\% \quad , \quad V_m = \frac{1}{t\rho_m} \left(\frac{m_c}{Lb} - n\rho_w \right) \cdot 100\% \quad , \quad V_v = 100 - (V_f + V_m) \quad (4.1)$$

Where V_f , V_m , V_v are volume fractions of fibers, matrix, and voids in a sample

n is number of fiber layers in a composite sample

t , L , b are thickness, length, width of a composite sample

m_c is mass of a composite sample

ρ_w is density of fiber layer, mass per unit of area

ρ_f is density of a single fiber, mass per unit of volume

ρ_m is density of matrix, mass per unit of volume

From formulae (4.1) volume ratio of fibers, matrix, voids as well as density of each kind of geocomposites can be shown in Table 4.8.

Table 4.8 Physical properties of geocomposites

Geocomposite with	Density [g/cm ³]	Volume fraction of fiber [%]	Volume fraction of matrix [%]	Volume fraction of voids [%]
Carbon	1.51	39	40	21
Basalt	1.97	40	45	15
E-glass	1.80	41	37	22

4.5.3 Mechanical properties of geocomposites in tension

Coupons were tested in tension mode according to ASTM C1275-00 [53]. Figure 4.17 presents tensile stress-strain diagram of geocomposites. Table 4.9 shows tensile properties of three types of geocomposites.

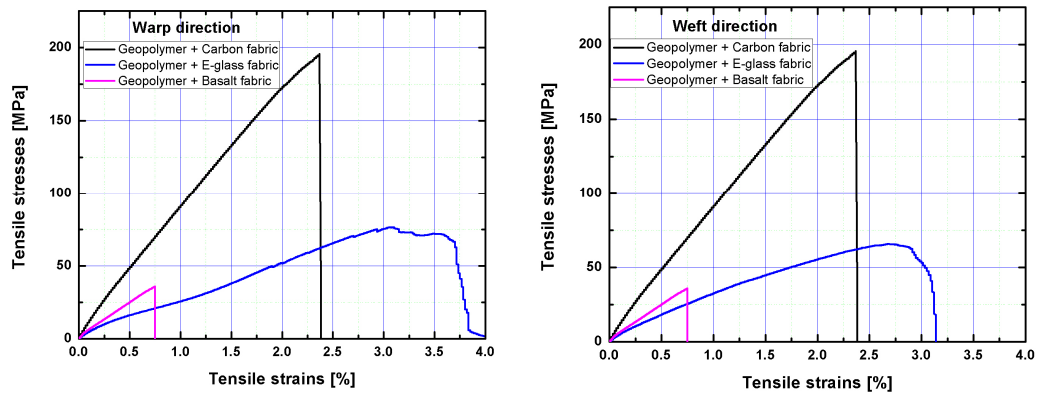


Fig. 4.17 Tension diagram of geocomposites in warp and weft directions

Table 4.9 Tensile properties of geocomposites

Geocomposites with fabrics	Mechanical properties in a warp direction			Mechanical properties in a weft direction		
	R_{mt} [MPa]	E [GPa]	ϵ_{mt} [%]	R_{mt} [MPa]	E [GPa]	ϵ_{mt} [%]
Carbon	191.4	12.6	2.40	190.4	12.5	2.43
E-glass	76.3	9.6	3.19	65.6	8.5	2.72
Basalt	35.8	10.2	1.75	35.6	11.3	1.72

Obviously, the strength and Young's modulus values of carbon geocomposite expected are higher than those of E-glass and basalt geocomposites. To compare with two direction (warp and weft), the values of elastic modulus and strengths of geocomposites reinforced with carbon and basalt woven fabrics are relatively similar while there are a big difference in a case of E-glass geocomposite, tensile properties in warp direction are better than in weft direction. Surprisingly, the strength of basalt geocomposite is too low while

basalt fibers are more toughness than E-glass fibers. We should investigate microstructures at the damage surfaces of each material (Fig. 4.18).

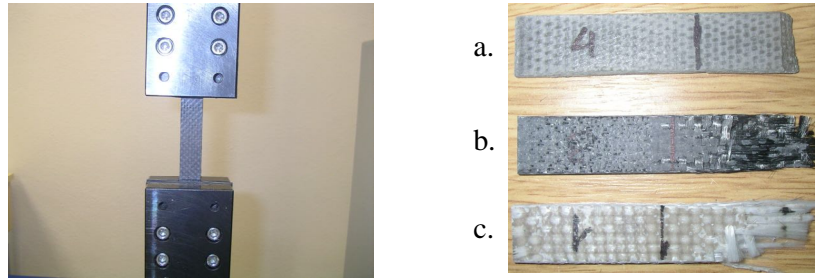


Fig. 4.18 Tensile failure of geocomposites with fabrics: a. Basalt; b. Carbon; c. E-glass

It is clear to the naked eye we can see that the failure trace of basalt geocomposite is definitely different from those of carbon and E-glass geocomposites. At the damage place the bundles of carbon and E-glass fibers still exist while basalt fibers disappear. In other words, carbon and E-glass textiles are still main constituents to carry loads. In contrast, maybe basalt fibers can interact chemically with the geopolymer and they create a completely new material look hard and brittle like ceramics.

4.5.4 In-plane shear properties of geocomposites

Series of the V-shaped notched samples fabricated are used to measure in-plane shear properties of geocomposite. Specimens were gripped by four halves of Arcan fixture and mounted on testing machine [54]. One DIC camera of Dantec Dynamics Company was used to analyze strain field of specimens thanks to a good speckle pattern on them (Fig. 4.19). All shear tests were performed at the same loading speed of 1mm/min and at room temperature (20-25 °C), approximately 70% relative humidity.

Due to high structural heterogeneity of material, it leads to the state of stress at a center of a specimen is not completely a pure shear states. However, plane shear stress can be measured thanks to loads recorded from a load cell of a testing machine and plane shear strain of the central part of a specimen can be determined optically by the Q-400 camera system. The optical device was set up to take one picture per one second. Both testing machine and the optical device were synchronized together.

Here, magnitude of shear stress was able to calculate approximately by an equation (4.2)

$$\tau_{xy} = \frac{F}{b.t} \quad (4.2)$$

where F is a value of loads; b and t is dimension of the middle cross section of a specimen. $b = 40$ mm for all coupons; $t = 4.47$ mm for carbon geocomposite coupon; $t = 3.73$ mm for carbon geocomposite coupon; $t = 4.63$ mm for basalt geocomposite coupon.



Fig. 4.19 Geocomposite specimens for shear and experiments

And shear deformation of specimen, γ_{xy} , was based on principles comparing positions of particles on a specimen with the reference position of particles when a specimen was not deformed [55]. Value of shear strain component can be determined from displacements of particles as well as from current positions of them on the surface of a sample.

For small strains
$$\gamma_{xy} = \frac{\partial u}{\partial Y} + \frac{\partial v}{\partial X} \quad (4.3a)$$

and for finite strains
$$\gamma_{xy} = \frac{\partial x}{\partial X} \cdot \frac{\partial x}{\partial Y} + \frac{\partial y}{\partial X} \cdot \frac{\partial y}{\partial Y} \quad (4.3b)$$

or
$$\gamma_{xy} = \frac{\partial u}{\partial Y} + \frac{\partial v}{\partial X} + \frac{\partial u}{\partial X} \cdot \frac{\partial u}{\partial Y} + \frac{\partial v}{\partial X} \cdot \frac{\partial v}{\partial Y} \quad (4.3c)$$

where (x, y) and (X, Y) are instantaneous and reference positions of particles on a specimen.

$u = x - X$ and $v = y - Y$ are displacements of particles on a specimen.

A program written in Matlab language is used to read displacement and coordinate of points on digital images produced from camera (see Appendix B.1). In order to save time and memory for computer, we only focused on sub-region envelop by a mask which was large enough to represent deformation of materials at a center of a specimen. Outputs of the program were shear strains of a specimen corresponding to every load step in accordance with equations (4.3a), (4.3b).

Figure 4.20a shows in-plane shear stress-strain diagrams of carbon and E-glass geocomposites with the exception of basalt geocomposite failed very early because of being very brittle.

Figure 4.20b presents distribution of the first principal strain on a middle zone of specimen. Generally, shear deformation is not uniform and pure because of the color spectrum displaying values of principal strain and directions of them.

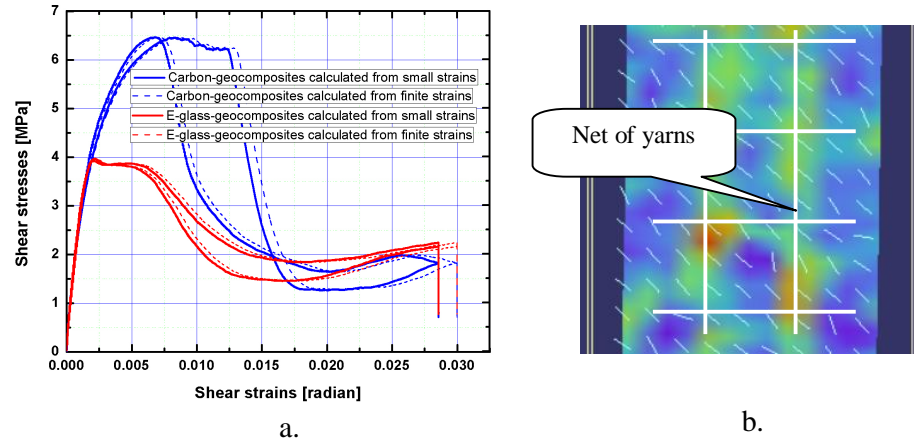


Fig. 4.20 a. In-plane shear stress-strain diagrams of geocomposites;

b. The first principal strain field of geocomposites from DIC camera

From the shear graphs, the elastic shear modulus and the shear strengths of geocomposites can be determined and shown in Table 4.10.

Table 4.10 In-plane shear properties of geocomposites

Materials	In-plane shear modulus [GPa]	In-plane shear strengths [MPa]
Carbon geocomposite	5.0	6.45
E-glass geocomposite	5.0	3.82
Basalt geocomposite	Failed early because of being too brittle	

The interesting character here is that modulus of two geocomposites are the same while strengths of them differ completely. Carbon woven geocomposite have shear resistance with 70% higher than E-glass woven geocomposite. We can explain this phenomenon as follow. With a very brittle nature and to form many micro-cracks when dried, geopolymer resin has low shear and tensile abilities. Therefore, when deformation of two geocomposites is small, shear occurs mainly in resin leading to the same as capacities of shear resistance of them. However, when deformation is big enough, shear resistance depends on adhesion between fiber and resin. Here, adhesive ability of carbon fiber and geopolymer is much better than E-glass and geopolymer.

Failure mode of geocomposite samples by shear loads illustrates in a figure 4.21. Specimen was not torn into two parts as usual but a narrow band of swell appeared on both surfaces of the sample and then delamination phenomena occurred. It is possible to explain as follows. With load condition, the plane stress state occurs in a sample equivalent to a principal plane stress state, in which, one principal stress is tensile and the other is compressive. Under compression, layers in specimen was buckled and delaminated. Finally, one narrow band of swell was formed and accompanying samples were destroyed. However, shear stress did not reduce to zero but remained minimum value and increased a little because fibers in a specimen still carried loads.

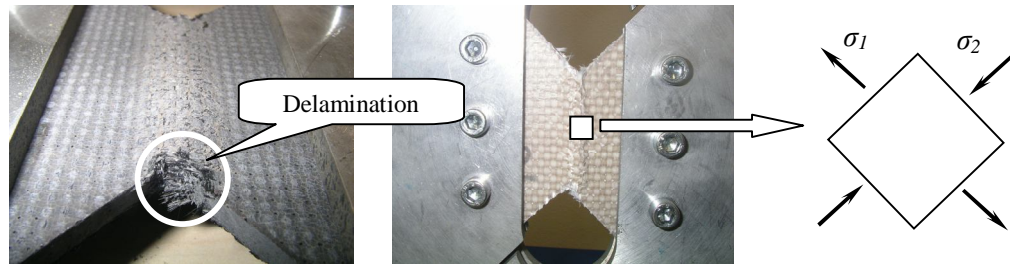


Fig. 4.21 Failure mode of geocomposite samples under shear loads

4.5.5 Interlaminar shear strength of geocomposites

Interlaminar shear strength (ILSS) refers to the shear strength parallel to the plane of lamination. It is measured in a short-beam shear test in accordance with ASTM D2344 [56]. A flexural specimen of small span–depth or thickness (S/t) ratio is tested in three-point bending to produce a horizontal shear failure between the laminas [56]. To explain the short-beam shear test, let us consider the following homogeneous beam equations:

$$\text{Maximum normal stress:} \quad \sigma_M = \frac{3PS}{2bt^2} = \frac{3P}{2bt} \cdot \left(\frac{S}{t} \right) \quad (4.4a)$$

$$\text{Maximum interlaminar shear stress:} \quad \tau_M = \frac{3P}{4bt} \quad (4.4b)$$

where P is loads; S is the span of a beam; b and t are the width and thickness of a beam. From equation (4.4), it can be seen that the maximum normal stress in the beam decreases with decreasing S/t ratio and the maximum shear stress (at the neutral axis) is not affected by the S/t ratio. Thus, for sufficiently small S/t ratios, the maximum shear stress in the beam will reach the ILSS of the material even though the maximum normal stress is still quite low.

Thus, the beam will fail in the interlaminar shear mode by cracking along a horizontal plane between the laminas (Fig. 4.22).

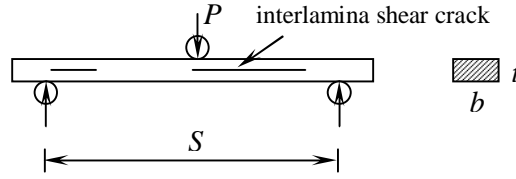


Fig. 4.22 Failure mode of geocomposite samples under shear loads

E. Sideridis et al. [57] discussed the the effects of S/t ratios on the failure mode of beams as follows. From equation (4.4a) and (4.4b), the two stresses are related:

$$\frac{\sigma_M}{\tau_M} = \frac{2S}{t} \quad \text{or} \quad \frac{\sigma_M}{2\tau_M} = \frac{S}{t} \quad (4.5)$$

If σ_F and τ_F are called the failure stress in flexure and in shear of materials, the failure of the specimen in shear occurs when

$$\tau_M = \tau_F \quad \text{and} \quad \sigma_M < \sigma_F \quad (4.6)$$

Combine (4.5) and (4.6), we have

$$\frac{S}{t} < \frac{\sigma_F}{2\tau_F} \quad (4.7)$$

The inequality (4.7) is a condition for the specimen will fail by interlaminar shear that means S/t ratios must be limited by $\sigma_F/2\tau_F$ ratio. Here, τ_F is determined by (4.4b) and σ_F equals to tensile strength of materials in the Table 4.9. However, if S/t ratios satisfy the condition (4.7), we need also to observe the type of failure in shear that is cracks at the middle of the thickness. In practice, with short-beam shear tests of many laminates, maximum shear stress may occur in an area where other stresses may exist. As a result, a combination of failure modes, such as fiber rupture, microbuckling, and interlaminar shear cracking, are observed. Interlaminar shear failure may also not take place at the laminate midplane.

Sample series of three geocomposites were fabricated with 15mm width and 3mm thickness for interlaminar shear tests. These samples were tested in three-point bending with span 64mm. Results obtained from experiments are graphs of flexural stress and strain relations (Fig. 4.23). We can see that behaviors as well as the maximum stresses of all geocomposites are almost similar. To verify the condition for the short-beam shear test, values of σ_F in the equation (4.7) are taken from Table 4.9 with the tension strengths of

geocomposite in warp direction, values of τ_F are calculated by equation (4.4b). The way to verify is carried on below.

For carbon geocomposites:

$$\sigma_F = 193.4 \text{ MPa}, \tau_F = 1.75 \text{ MPa} \text{ leads to } S/t = 64/3 = 21.33 < \sigma_F / (2\tau_F) = 55.26$$

For E-glass geocomposites:

$$\sigma_F = 76.3 \text{ MPa}, \tau_F = 1.66 \text{ MPa} \text{ leads to } S/t = 64/3 = 21.33 < \sigma_F / (2\tau_F) = 23$$

For basalt geocomposites:

$$\sigma_F = 35.8 \text{ MPa}, \tau_F = 1.76 \text{ MPa} \text{ leads to } S/t = 64/3 = 21.33 > \sigma_F / (2\tau_F) = 10.17$$

We can see that only carbon geocomposite samples and E-glass geocomposite samples are suitable for the short-beam shear test. We continue to check the failure modes for each type of geocomposites (Fig. 4.24). Obviously, microbuckling and interlaminar shear cracks occurred in thickness of carbon geocomposite specimens and E-glass geocomposite specimens. On the contrary, for basalt geocomposite samples, due to brittle character there was not any interlaminar shear cracks exception of fiber and matrix ruptures.

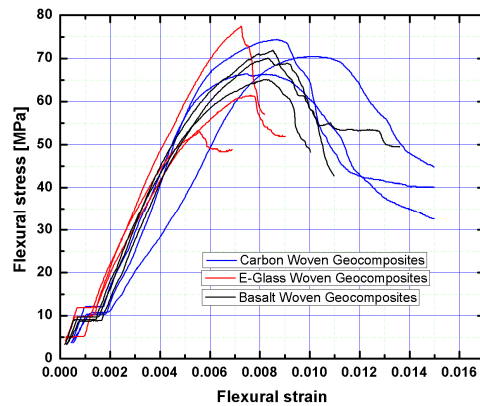


Fig. 4.23 The stress-strain diagrams for a three-point bending tests of short-beam

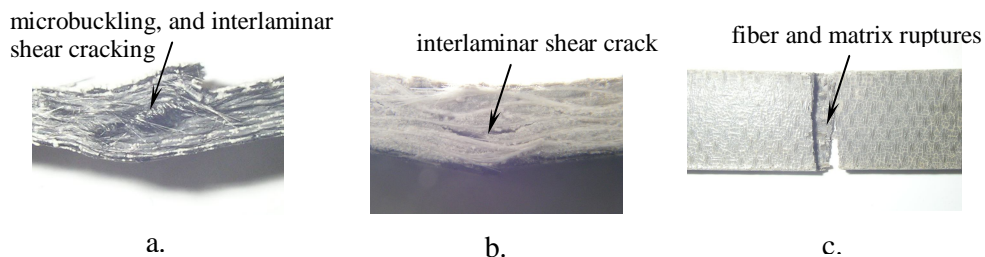


Fig. 4.24 Failure modes of geocomposites with: a. Carbon; b. E-glass; c. Basalt

In conclusion, measured values of ILSS for geocomposites reinforced by carbon and E-glass woven fabrics are shown in Table 4.11. Generally, ILSS depends primarily on the matrix properties and fiber–matrix interfacial shear strengths rather than the fiber properties.

Table 4.11 Interlaminar shear strengths of geocomposites

Geocomposites with fabric	ILSS [MPa]
Carbon	1.75
E-glass	1.66

4.5.6 Fire-resistant properties of geocomposites

Geopolymers are still considered as a new material for coatings and adhesives, a new binder for fiber composites, and new cement for concrete. They are mineral polymers and the essence of all mineral polymers is never burn [58]. Therefore, we can state that geopolymer materials are ideal for high temperature and fire applications.

In order to study the fire-resistant properties of geocomposites, three following groups of specifications of materials should be investigated, including: ignitability, heat release and smoke for the first group; the second group includes flame spread index and the last one is residual flexural strength [59]. Among these parameters, researchers determined that perhaps the most important fire behavior parameter for structure applications is the strength retention of the composite after fire exposure [59]. The research will focus on the analysis of the flexural mechanical properties remaining of geocomposites after suffering fire.

Because the price per one square meter of carbon fabric is 3.2 times higher than of basalt fabric and 8.6 times higher than of E-glass fabric (Table 4.5), and in order to produce geocomposite materials with a low cost, total six kinds of geopolymer composites consisting of three pure woven fabric kinds and three hybrid woven fabric kinds based on geopolymer binders (Table 4.12). All samples have nominal dimension of 3x14x90mm with fiber volume fraction varying from 39% to 41%.

Samples were heated to 200 °C, 400 °C, 600 °C, 800 °C and 1000 °C in an oxidizing environment by the furnace with a 25 kW/m² radiant heat source for a duration of 30 minutes according to ASTM E-662 protocol for smoke generation in a flaming mode (see Fig. 4.25). After heating, the samples were cooled spontaneously in room temperature (see Appendix

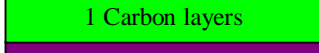
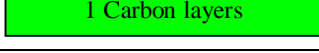
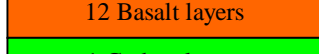
A.1). Then samples were prepared for mechanical tests on three-point bending strength bending.

The residual mechanical properties of composites after exposing up to high temperature are measured on Universal Tensile Testing machine Instron Model 4202 in accordance with ASTM C1314-06 [60]. The machine plots graph of stress-strain automatically. Values of stress, strain, modulus of elasticity of a beam are calculated from equations (4.8):

$$\sigma = \frac{3PS}{2bt^2} ; \quad \varepsilon = \frac{6Dt}{S^2} ; \quad E = \frac{d\sigma}{d\varepsilon} = \frac{S^3}{4bt^3} \cdot \frac{dP}{dD} \quad (4.8)$$

where σ is maximum stress in the outer fiber at a given force; S is support span; b , t is test specimen width and thickness of test specimen; D is deflection at beam center; ε is maximum strain in the outer fiber; E is modulus of elasticity in bending; dP/dD is ratio of force difference and deflection difference at beam center, are measured on a linear elastic segment of graph. The flexural strengths are measured at the maximum loads.

Table 4.12 Six kinds of samples for experiments of fire-resistant properties of geocomposites

Materials	Name	Stack order
Geocomposite with 7 E-glass layers	7E	
Geocomposite with 10 Carbon layers	10C	
Geocomposite with 15 Basalt layers	15B	
Geocomposite with 5 E-glass layers and 2x2 Basalt layers on both surfaces	5E+2x2B	  
Geocomposite with 5 E-glass layers and 2x1 Carbon layers on both surfaces	5E+2x1C	  
Geocomposite with 12 Basalt layers and 2x1 Carbon layers on both surfaces	12B+2x1C	  

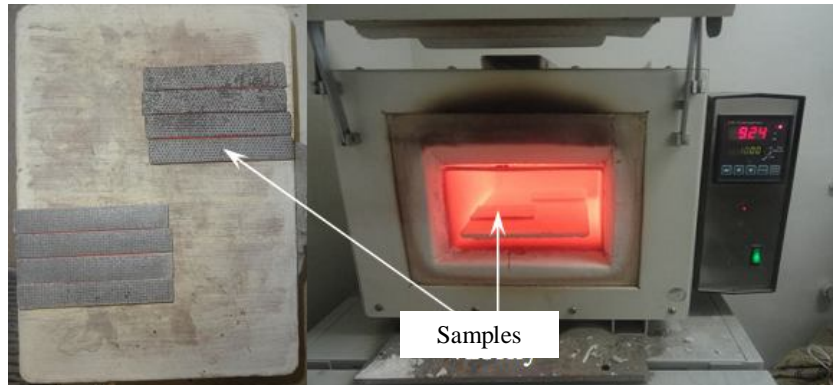


Fig. 4.25 Heating the samples at 1000 °C

Outputs of research need to be determined:

- Thermal thickness expansion, mass loss and densities of geocomposites after heating levels.
- Variation of flexural property retention (modulus of elasticity, flexural strengths, strains in the outer fiber at flexural strength) of geocomposites after heating levels.

Data of tests for each of geocomposite types are presented in Table 4.13a, b, c, d, e, and f.

Table 4.13a Experiment results of geocomposite 7E

Temperature	Density	Thickness	Strain at flexural strength	Flexural strength	Flexural modulus	Mass loss	Thickness expansion
[°C]	[g/cm ³]	[mm]	[%]	[MPa]	[GPa]	[%]	[%]
20	1.88	3.30	0.70	73.2±4.4	14.0±1.5	0.00	100.0
200	1.60	3.82	0.80	19.4±3.2	4.6±0.8	2.26	115.8
400	1.20	4.87	1.09	9.1±1.5	1.2±0.2	4.32	145.5
600	1.07	5.24	0.57	8.3±0.5	2.0±0.7	5.15	162.4
800	1.07	5.58	0.49	17.2±2.3	5.5±0.7	5.26	168.6
1000	0.73	8.88	Samples still exist, but have low mechanical properties			5.03	261.9

Table 4.13b Experiment results of geocomposite 10C

Temperature	Density	Thickness	Strain at flexural strength	Flexural strength	Flexural modulus	Mass loss	Thickness expansion
[°C]	[g/cm ³]	[mm]	[%]	[MPa]	[GPa]	[%]	[%]
20	1.63	3.14	0.81	70.4±4.0	14.8±2.5	0.00	100.0
200	1.54	3.24	0.60	39.3±2.9	11.7±2.2	5.02	103.4
400	1.21	4.11	1.16	25.6±1.3	2.8±0.5	7.40	123.2
600	1.08	4.13	1.33	17.8±0.8	1.5±0.1	14.97	128.2
800	1.07	4.11	0.73	43.3±6.3	9.2±1.5	16.08	123.6
1000	1.13	3.90	0.79	55.8±1.9	10.7±0.5	14.16	120.3

Table 4.13c Experiment results of geocomposite 15B

Temperature	Density	Thickness	Strain at flexural strength	Flexural strength	Flexural modulus	Mass loss	Thickness expansion
[°C]	[g/cm ³]	[mm]	[%]	[MPa]	[GPa]	[%]	[%]
20	1.95	3.50	1.23	95.7±7.7	9.7±1.5	0.00	100.0
200	1.38	4.82	0.38	22.1±0.8	14.8±1.0	7.78	137.0
400	0.89	6.97	0.60	9.5±0.7	3.9±0.9	11.27	211.7
600	0.77	8.00	0.81	9.3±0.2	3.0±0.7	11.99	232.1
800	0.75	8.00	0.70	9.1±0.4	3.9±0.6	11.95	233.3
1000	0.65	9.00	0.71	5.3±0.4	2.9±0.2	11.73	272.7

Table 4.13d Experiment results of geocomposite 5E+2x2B

Temperature	Density	Thickness	Strain at flexural strength	Flexural strength	Flexural modulus	Mass loss	Thickness expansion
[°C]	[g/cm ³]	[mm]	[%]	[MPa]	[GPa]	[%]	[%]
20	2.00	3.10	0.74	77.7±5.9	12.1±1.4	0.00	100.0
200	1.74	3.30	0.95	44.3±6.6	5.9±1.2	7.04	105.4
400	1.32	4.26	1.29	29.1±1.7	6.2±0.7	9.09	134.6
600	1.23	4.50	0.43	19.5±2.0	3.8±1.7	9.60	146.4
800	1.11	4.97	0.22	15.6±1.2	3.1±0.8	9.86	157.1
1000	0.74	7.71	0.33	6.0±1.4	2.3±1.0	10.41	243.0

Table 4.13e Experiment results of geocomposite 5E+2x1C

Temperature	Density	Thickness	Strain at flexural strength	Flexural strength	Flexural modulus	Mass loss	Thickness expansion
[°C]	[g/cm ³]	[mm]	[%]	[MPa]	[GPa]	[%]	[%]
20	1.90	3.02	0.83	62.9±4.8	12.4±0.8	0.00	100.0
200	1.65	3.33	0.77	67.1±4.1	12.4±0.7	7.60	104.8
400	1.20	4.37	0.83	18.6±1.8	3.6±0.8	9.49	142.9
600	1.10	4.65	0.56	13.5±0.5	3.9±0.4	12.36	151.3
800	1.03	4.90	0.55	11.7±0.5	3.2±0.6	13.99	159.8
1000	0.76	7.15	0.51	6.3±2.1	1.1±0.2	13.27	231.7

Table 4.13f Experiment results of geocomposite 12B+2x1C

Temperature	Density	Thickness	Strain at flexural strength	Flexural strength	Flexural modulus	Mass loss	Thickness expansion
[°C]	[g/cm ³]	[mm]	[%]	[MPa]	[GPa]	[%]	[%]
20	2.02	2.90	0.88	80.1±9.4	10.4±1.1	0.00	100.0
200	1.46	4.04	1.24	66.6±7.4	6.7±1.0	5.38	128.8
400	1.21	4.90	0.92	22.4±5.5	4.5±1.8	8.80	155.8
600	0.82	6.45	1.34	10.3±1.0	2.9±0.9	13.42	212.6
800	0.76	7.14	1.33	5.5±2.2	3.1±1.3	14.52	224.5
1000	0.63	8.79	Samples still exist, but have low mechanical properties			13.14	280.0

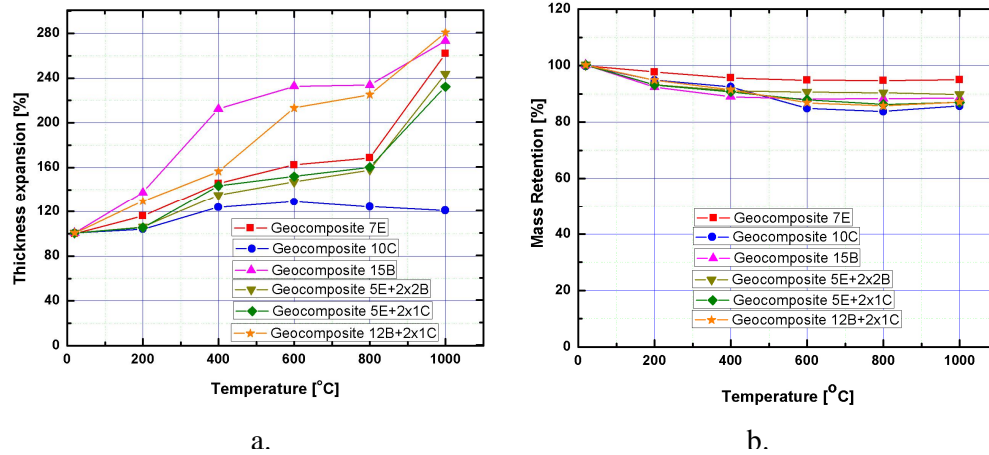


Fig. 4.26 a. Thickness expansion of geocomposites; b. Mass retention of geocomposites

Figure 4.26 shows comparison of thermal expansion in thickness and comparison of mass loss of geocomposite samples after heating levels. Generally, almost all sample thicknesses increases drastically while lengths and widths of them vary insignificantly by heating. Geocomposites reinforced with only basalt fabrics or combined with two carbon layer on surfaces have the highest thickness increase to 180% after heating to 1000 °C. Geocomposites with E-glass fabrics (pure or hybrid) have the same of thermal expansion in thickness at intermediate level, about 50% rising compared to originals after heat exposure from 400 °C to 800 °C, but reach approximate 2.4 times at 1000 °C than at room condition. In the opposite tendency, carbon geocomposite arise with thermal stability has the lowest thickness increase, only 20% than original thickness.

Thermal expansion in sample thickness is accompanied with mass loss by temperature effect. The graph shows that the mass of geocomposites reinforced with basalt and carbon fabrics decrease rapidly with the mass loss approximate 15% when they were heated to 600 °C and remain constantly when the temperature is above 600 °C. Mass loss of composites reinforced with glass fabrics is lowest, about 5% after heating to 1000 °C. The graph also shows that the value of all the weight of composites is almost unchanged when heated above 600 °C. Reduced mass can be explained by the evaporation of water from the geopolymer matrix or decomposition of impurities within the composite, and the oxidation of carbon fiber parts in the outer layers. Due to the chemical curing process of geopolymer materials, the

mass loss could also be due to the curing of unreacted elements, which would also suggest insufficient post-cure temperatures were achieved during composite manufacture.

Figure 4.27 presents residual mechanical properties (bending strengths and elastic modules) of all the different composites after exposure in an oven at different temperature. Generally, geocomposite materials after high temperature exposure became more brittle and degraded.

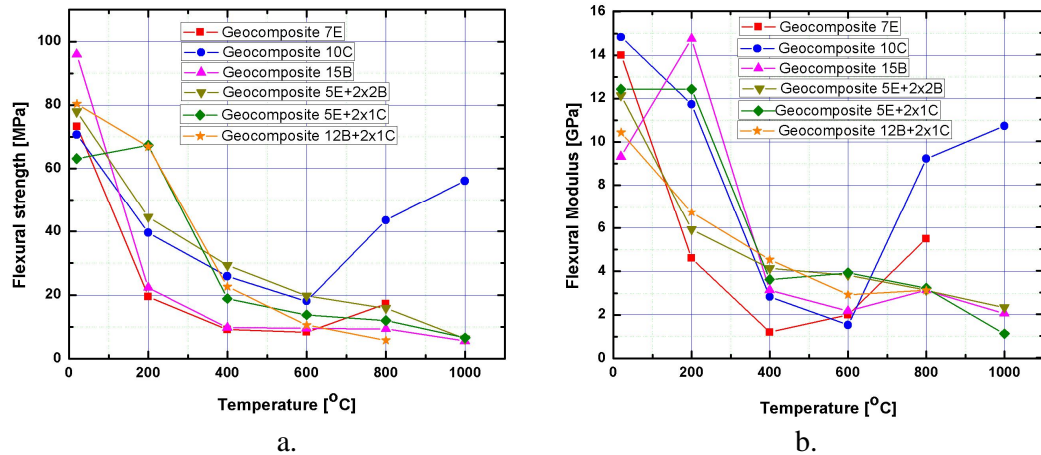


Fig. 4.27 Residual flexural properties of geocomposites after heating

The graph shows that the highest value of flexural strength was measured in geocomposite named 15B at room temperature to 95MPa. The bending strengths of the other composites at 20 °C vary from 60 to 80MPa and elastic modulus of all composites at 20 °C achieve 9 to 15GPa. Of course, it can be seen that the residual strength of all geocomposites decreases severely after heating at different levels of 200 °C, 400 °C, 600 °C, 800 °C, and 1000 °C for 30 minutes. At level of 400°C, geocomposite 10C remains 36% of original ultimate strength; hybrid geocomposites 5E+2x1C, 5E+2x2B, 12B+2x1C kept 29%, 37%, 27% of strengths in room temperature while for geocomposites 7E and 15B are only 12% and 10%. After level of 400 °C, ultimate strength retention seems to reduce with much smaller gradients. Interestingly, the remaining strength of composites 10C increases when the temperature is above 600 °C and has good toughness of approximate 79% after heating at 1000 °C. Rising strength at temperatures above 600 °C can be explained as homogenization mechanism between the geopolymer matrix and reinforced fabrics, thereby improving adhesion. We can also observe that the residual flexural strengths of the hybrid geocomposites

such as 5E+2x2B, 5E+2x1C, 12B+2x1C are much higher than of the geocomposites 7E, 15B after heating from 200 °C to 600 °C.

Similar to the flexural strength trends the flexural modules of almost geocomposites also reduce after being heated to a temperature higher than 200 °C for 30 minutes exception of the modulus of composites 10C increases when the burn temperature is above 600 °C and has good stiffness to 1000 °C.

As known in Table 4.7, carbon and basalt fibers are destroyed until 700 °C; E-glass fiber retains strength after exposing up to 700 °C. However, when combined to geopolymer matrix, these fibers can sustain higher temperatures; especially carbon fiber impregnated with geopolymer resin can bear up to 1000 °C. Hung T.D et al got also similar results that strength retention about 60% when studying composites combined geopolymer and carbon unidirectional fibers. They assumed that one initial reaction layer was generated on a surface of carbon fiber and protected fiber from oxidation environments.

Optical microscopy allows observing microscopic objects and structures up to 1000-times magnification without special treatment under normal microscope and sample preparation by grinding and polishing. Figures 4.28 taken by using higher resolution optical microscope (NIKON EPIPHOT 200) shows microstructure of the geocomposite 7E+2x1C, 15B, 10C when heated to the temperature 1000 °C. Some microstructure of the geocomposite 7E, 15B, 10C when burned in different temperatures can be seen in Appendix A8-A10.

Observing figure 4.28b we can see that geocomposite 15B had the highest thickness expansion due to high temperature, which is also a cause of degradation for both matrix and fiber when heated above 200 °C. The microstructural analysis shows that due to the high temperatures a lot of pores were created in geopolymer matrix, this leads to an expansion of composite samples. Composites reinforced with glass, and basalt fabrics have similar characteristics when heated to temperature of 1000 °C, in which the fibers melted and the composites was homogenized.

However, composite 10C has good thermal stability with increasing temperature; the structure is almost unchanged after heating to 800 °C. No cavities exist in the matrix. This may be attributed towards the good wetting properties exhibited between carbon fabric and polymer matrix. At a temperature of 1000 °C there has been a chemical change in the matrix, thus increasing the mechanical properties of the composite (see Fig. 4.28c).

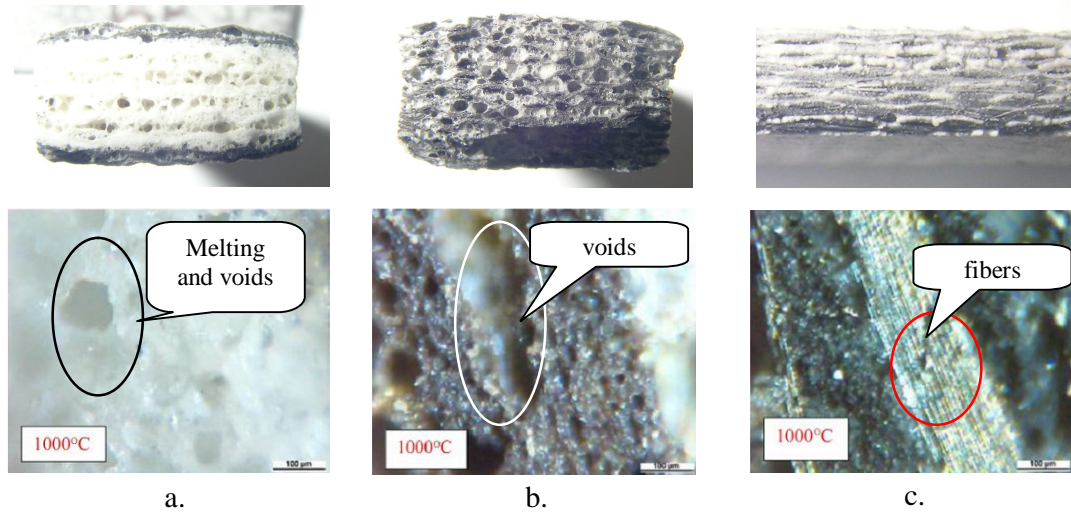


Fig. 4.28 Observation of the microstructure of the geocomposite when heated to the temperature 1000 °C: a. geocomposite 7E+2x1C; b. geocomposite 15B; c. geocomposite 10C

4.5.7 Thermal conductivity of geocomposites

For the measurement of low conductivity materials such as thermal insulations, geocomposite materials need to be measured thermal conductivity in temperature environment from 25 °C to 250 °C. In this section, we conduct to evaluate thermal conductivities of materials combined geopolymer with fiber fabric carbon, E-glass, and basalt. The dimensions of all the samples for thermal experiment were (12.6 x 12.6) mm². The samples were coated with graphite in order to increase the absorption of flash light on the front surface and to increase the emissivity on the back surface. The samples were measured five times at each temperature. The specific heat was measured with the LFA 447 by a comparative method. For this, the system was calibrated with a reference sample (Pyroceram 12.6 mm in diameter, 2.5 mm thick). The density of the samples at room temperature was determined by measuring of mass and volume.

The measured data was used to compute the thermal conductivity by following equation [61]:

$$\lambda = \rho \cdot C_p \cdot \alpha \quad (4.9)$$

where λ is thermal conductivity, W/(m.K); C_p is specific heat, J/(g.K)

α is thermal diffusivity, mm²/s;

ρ is bulk density, g/cm³, see Table 4.8

Table 4.14a, b, c show thermo-physical data of three geocomposites. Figure 4.29 illustrate dependences of thermal properties on temperature.

Table 4.14a Thermo-physical properties of carbon geocomposite

Density (25 °C): 1.51 g/cm³ ; Thickness (25 °C): 2.270 mm			
Temperature [°C]	Thermal Diffusivity [mm²/s]	Specific Heat [J/(g.K)]	Thermal Conductivity [W/(m.K)]
25	0.415	1.055	0.661
100	0.346	1.272	0.665
150	0.311	1.432	0.672
200	0.281	1.568	0.665
250	0.268	1.633	0.661

Table 4.14b Thermo-physical properties of E-glass geocomposite

Density (25 °C): 1.80 g/cm³ ; Thickness (25 °C): 2.210 mm			
Temperature [°C]	Thermal Diffusivity [mm²/s]	Specific Heat [J/(g.K)]	Thermal Conductivity [W/(m.K)]
25	0.278	0.942	0.471
100	0.242	1.080	0.470
150	0.227	1.137	0.465
200	0.213	1.180	0.452
250	0.207	1.211	0.451

Table 4.14c Thermo-physical properties of basalt geocomposite

Density (25 °C): 1.97 g/cm³ ; Thickness (25 °C): 3.490 mm			
Temperature [°C]	Thermal Diffusivity [mm²/s]	Specific Heat [J/(g.K)]	Thermal Conductivity [W/(m.K)]
25	0.334	0.952	0.626
100	0.242	1.105	0.527
150	0.210	1.217	0.503
200	0.197	1.292	0.501
250	0.191	1.313	0.494

In a general, the specific heat capacity increases with temperature as expected from Debye theory for three kinds of geocomposites. But specific heat gradient of carbon geocomposite to temperature achieves maximum value while those of two the other seemed much lower. Specific heat capacity rises almost linearly from 950 to 1650 J/(kg.K) over the temperature range.

Through thickness thermal conductivity was fairly static over the 25-250 °C range at approximately 0.46 W/mK for E-glass geocomposite and 0.66 W/mK for carbon geocomposite. However, for basalt geocomposite, through thickness thermal conductivity decreases rapidly from 0.625 W/mK at room temperature to 0.500 W/mK at 150 °C and then

keeps constantly to 250 °C. Although the thermal conductivity of the geopolymer matrix is yet unknown, but the thermal conductivity of result geocomposite is rather low like an engineering ceramic material and is consider as thermal insulation materials.

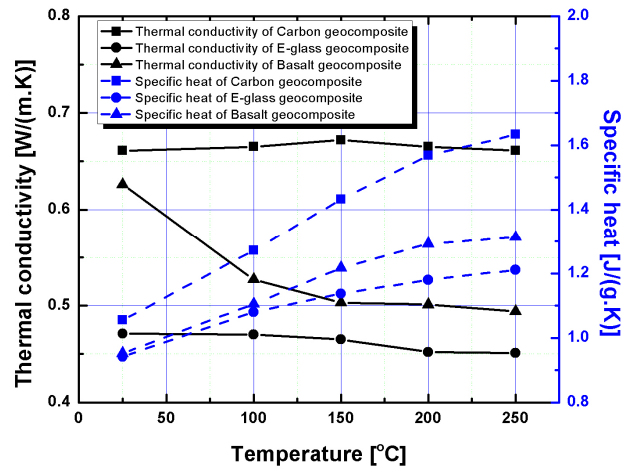


Fig. 4.29 Thermal conductivity and specific heat of geocomposites

4.5.8 Micro-structural evolution

The phase and microstructure of the samples were analysed before and after firing test of 1000 °C in a furnace to assess the effect of high temperature exposure to fabric reinforced geocomposite. Figure 4.30 shows the SEM microstructure of the geopolymer and the composites before fire test. Geopolymer shows the less porosity on the surface of the matrix. Geocomposite before firing shows the good adhesion of the matrix that minimizes pores in matrix.

Figure 4.31 shows the microstructure of the geocomposite after fire test at 600 and 1000 °C. After fire test, the porosity enlarges and wet ability between the matrix and fiber varies widely. The gap between fiber and matrix increases during firing due to the shrinkage and dehydration of moisture from the matrix. Carbon fiber exhibits good adhesion between fiber and matrix in compare with E-glass fiber. Basalt reinforced fiber in the geocomposite showed good adhesion and interaction between basalt fiber and geo polymer. The interaction during the fire test may be attributed towards the mineral composition of basalt and geopolymer composition. The ionic exchange between the basalt fiber and matrix has been observed in developing agglomeration and coarse concrete like structure. E-glass fiber

detachment from the matrix of the geopolymer is observed may be due to the wide difference coefficient of thermal expansion between fiber and E-glass. Carbon reinforced fiber before and after fire test shows good adhesion although minor crack is observed in the fired composite. This gap would create dehydration pathway for moisture upon firing. Thermal stability in carbon reinforced geocomposite increases with temperature with increasing the homogeneities of the matrix within fiber distribution. Carbon induced the mechanical strength of the composite with increasing temperature, although some mass loss observed during the high temperature. After firing the binding phase appeared more homogeneous and dense due to sintering at high temperatures.

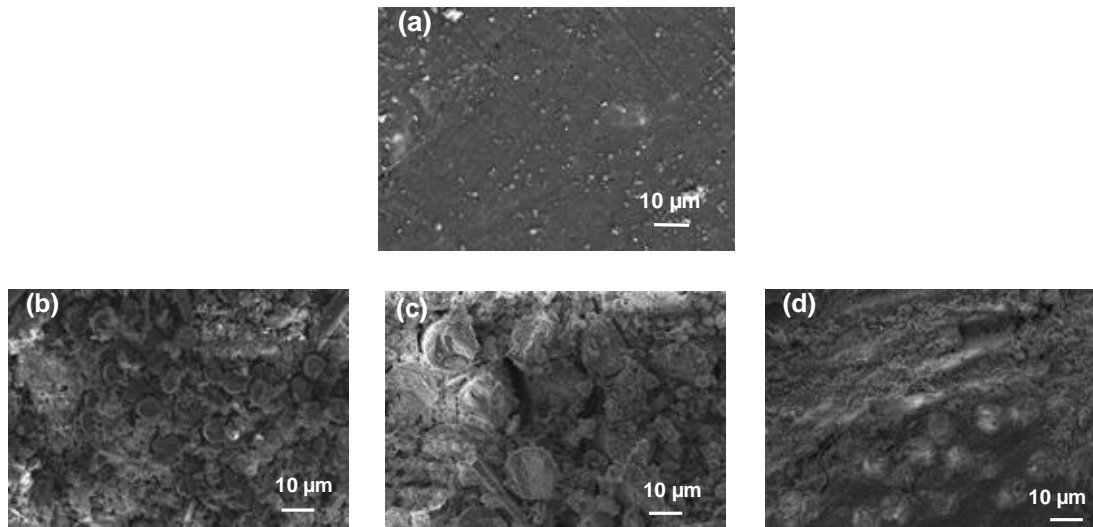


Fig. 4.30 SEM images of (a) geopolymer and geocomposites with fiber reinforced; (b) Carbon, (c) E-glass and (d) Basalt, without fire test.

4.5.9 Conclusion

Carbon reinforced geopolymers were found to be suitable geocomposite among the others fiber reinforced geo composites with suitable mechanical strength at higher temperature. Fire testing of the samples revealed the dissolution and degradation of the fiber in the composite at higher temperature. The fire testing showed that the time taken for the samples to exceed the failure condition was dependent on sample density. The lower density samples contained less water as they had a lower portion of the hydrated geopolymer phase. Water evaporates during the fire test which absorbs energy from the furnace that would have

otherwise been imparted to the sample. This is beneficial for fire resistant materials as it reduces the temperature of the sample.

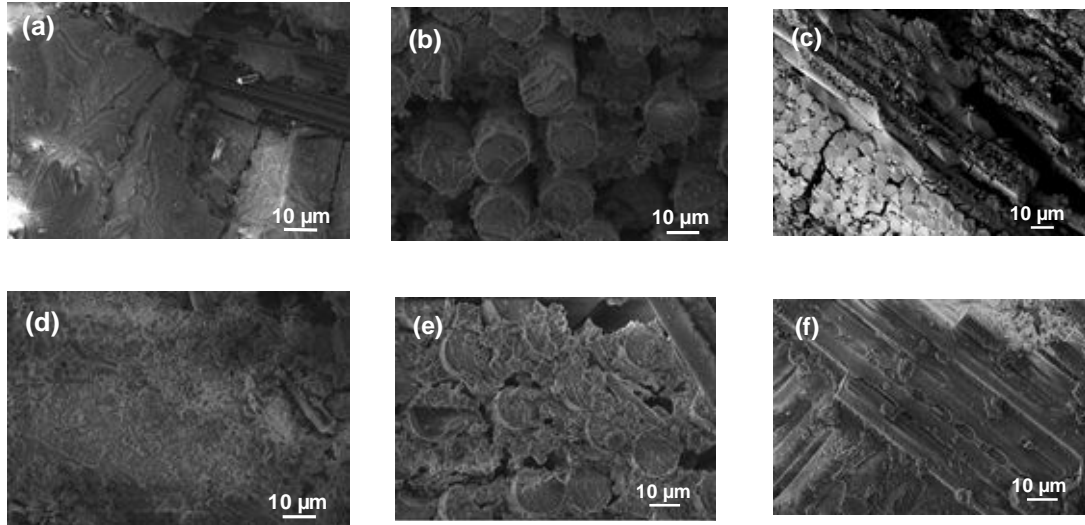


Fig. 4.31 SEM images of fired geo composites at 600 and 1000 °C, with respect as follows (a) carbon-reinforced geo composite, (b) E-glass reinforced geo composite, and (c) Basalt reinforced geo composite at 600 °C, (d) Carbon reinforced, (e) E-glass reinforced and (f) basalt reinforced geo composite at 1000 °C

Thermal conductivity is an intrinsic property of a material and will remain relatively constant for the duration of a fire test. Whereas water content drops quickly during a fire test and as such the longer a fire test continues, the greater the proportional influence the thermal conductivity will have on the fire rating. Carbon fibers showed best adhesion properties to the geo polymer matrix, whereas the E-fiber showed the pull out and dissolution within the matrix at high temperature. Basalt reinforced fiber may be induced the chemical reaction with matrix, as a result agglomeration and sintering behaviour observed in the geocomposite. The final product with basalt reinforced becomes hard, porous in nature. The matrix of the basalt reinforced geo composite is very porous in nature. The strong bonding and bridging effect of carbon fiber with the matrix hinders the pull out and increases the strengths of the materials. Amongst these fabrics, carbon fabric not only offers maximum extent of strength and resistance properties but also boost the thermal conductivity at elevated temperature that is the crucial point from tribo point of view. The rapid dissipation of frictional heat produced at the

contacts protects the matrix from degradation and fibers from delamination and helps in achieving of all performance properties.

Chapter 5

NUMERICAL SIMULATION OF ELASTIC BEHAVIOR OF GEOCOMPOSITES

5.1 INTRODUCTION

In this chapter we will devote to represent some numeric simulations of elastic behavior of geocomposite materials. The main goal is to verify the elastic parameters obtained from experiments in previous chapters associating with prediction of initial failures of geocomposite materials. However, all materials are laminates stacked and bonded together with the same orientation. According to equations (3.24) and (3.27), mechanical properties of laminate are the same as those of one thin lamina. But the lamina is considered as construction from numerous basic representative unit cells (or RVEs). Therefore, techniques are given out in this chapter to predict the elastic properties of one representative unit cell.

5.2 GEOMETRICAL MODEL OF UNIT CELLS

In general, a unit cell of lamina reinforced plain woven fabric is the rectangular parallelepiped which contains two yarn couples orthogonal interlaced and surrounded matrix. Assuming that, matrix and void amount distributes evenly both in yarn and between yarns. Matrix plays a role of adhesion for filament-filament and yarn-yarn (Fig. 5.1a).

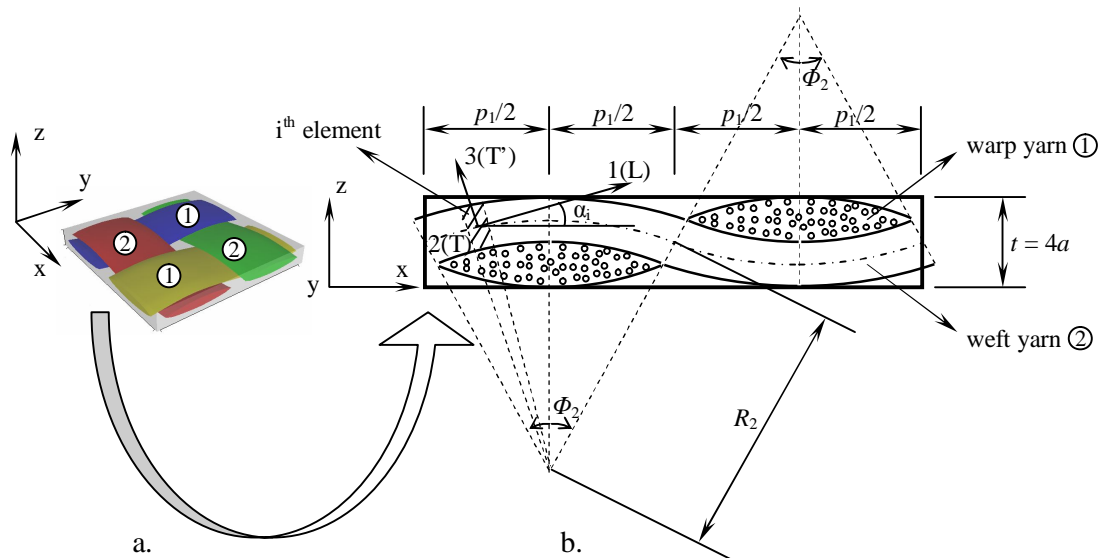


Fig. 5.1 a. Unit cell; b. Geometrical model of unit cell (view from y-direction)

Figure 5.1b illustrates geometrical model of unit cell viewed from y-direction. We need to consider general case that the geometrical parameters of warp yarn (denoted by index 1), and weft yarn (denoted by index 2) are different but have the same thickness (equal a half of lamina thickness). Because thickness and pitch of fabric are rather small, it is possible to hypothesize that each of yarn in a unit cell is composed of two arcs have the same radius, but in opposite directions; two systems of warp and weft yarns overlap ideally. Thus, the cross section of yarns is assumed to be lenticular.

We denote parameters:

- R_1, R_2 are the radii of warp and weft yarns.
- Φ_1, Φ_2 are the angles of warp and weft yarn arcs.
- p_1, p_2 are the center-to-center spaces (or pitches) of warp yarns and weft yarns.
- l_1, l_2 are the lengths of the warp and weft yarn axis.
- A_1, A_2 are the cross sections of warp and weft yarns.
- c_1, c_2 are the crimps of warp and weft yarns.
- $2a$ is the thickness of yarns.
- $t = 4a$ is the thickness of lamina.
- Ω_y is total volume of yarn within a unit cell.
- Ω_c is volume of unit cell.
- V_y is the total fiber volume fraction from model.

Among the above parameters, fabric thickness and pitch are known. The remaining parameters are dependent on these main parameters and are determined as follows.

From figure 5.1b, we have

$$\left\{ \begin{array}{l} \sin(\phi_2 / 2) = \frac{p_1}{2R_2} \\ \cos(\phi_2 / 2) = \frac{R_2 - a}{R_2} \end{array} \right. \text{ leads to } 1 = \sin^2(\phi_2 / 2) + \cos^2(\phi_2 / 2) = \left(\frac{p_1}{2R_2} \right)^2 + \left(\frac{R_2 - a}{R_2} \right)^2$$

After simplifying, we get $R_2 = \frac{4p_1^2 + t^2}{8t}$. Similarly, it can be written as $R_1 = \frac{4p_2^2 + t^2}{8t}$.

Consequently, the radii of warp and weft yarns will be

$$R_1 = \frac{4p_2^2 + t^2}{8t} ; \quad R_2 = \frac{4p_1^2 + t^2}{8t} \quad (5.1)$$

Form R_1, R_2 , the angles of warp and weft yarn arcs will be counted

$$\phi_1 = 2 \arcsin \left(\frac{4p_2 t}{4p_2^2 + t^2} \right); \quad \phi_2 = 2 \arcsin \left(\frac{4p_1 t}{4p_1^2 + t^2} \right) \quad (5.2)$$

The cross sections of warp and weft yarns:

$$A_1 = \left(\frac{4p_2^2 + t^2}{8t} \right)^2 (\phi_2 - \sin \phi_2); \quad A_2 = \left(\frac{4p_1^2 + t^2}{8t} \right)^2 (\phi_1 - \sin \phi_1) \quad (5.3)$$

The lengths of the warp and weft yarn axis within a unit cell:

$$l_1 = \frac{(4p_2^2 + t^2)\phi_1}{4t}; \quad l_2 = \frac{(4p_1^2 + t^2)\phi_2}{4t} \quad (5.4)$$

The crimps of warp and weft yarns:

$$c_1 = \frac{(4p_2^2 + t^2)\phi_1}{8p_2 t} - 1; \quad c_2 = \frac{(4p_1^2 + t^2)\phi_2}{8p_1 t} - 1 \quad (5.5)$$

Total volume of yarn within a unit cell:

$$\Omega_y = 2(A_1 l_1 + A_2 l_2) \quad (5.6)$$

The volume of unit cell:

$$\Omega_c = 4p_1 p_2 t \quad (5.7)$$

The total yarn volume fraction from model:

$$V_y = \frac{\Omega_y}{\Omega_c} \cdot 100\% = \frac{(A_1 l_1 + A_2 l_2)}{2p_1 p_2 t} \cdot 100\% \quad (5.8)$$

Applying this geometrical model for geocomposites reinforced carbon, basalt, E-glass we will obtain results of important quantities such as crimps, arc angles of warp and weft yarns, total yarn volume fraction shown in Table 5.1.

Table 5.1 The basic geometrical parameters of geocomposites

Geocomposite with	Thickness of unit cell t [mm]	Pitches of		Crimps of		Arc angles of		Total yarn volume fraction V_y [%]
		Warp yarn p_1 [mm]	Weft yarn p_2 [mm]	Warp yarn c_1	Weft yarn c_2	Warp yarn Φ_1 [degree]	Weft yarn Φ_2 [degree]	
Carbon	0.29	2.0	2.0	0.0035	0.0035	16.60	16.60	67
Basalt	0.19	1.9	1.9	0.0017	0.0017	11.46	11.46	67
E-glass	0.45	2.7	2.3	0.0064	0.0046	22.36	19.06	67

Comparing the total yarn volume fraction from model (in Table 5.1) with the volume ratio of fibers from experimental samples (in Table 4.8), we can realize that total fiber volume is smaller than total yarn volume. It proves that a portion of matrix must exist in a space of yarns. From hypothesis of equal distribution of matrix and voids, we are easy to calculate percentages of matrix and void volumes contained inside and outside yarn. Finally, the distribution of fibers, matrix, and voids in each of unit cells are presented in Table 5.2.

Table 5.2 The distribution of fibers, matrix, and voids in each of unit cells

Geocomposite with	Volume fraction of fiber [%]	Volume fraction of matrix [%]		Volume fraction of voids [%]	
		Inside yarn	Outside yarn	Inside yarn	Outside yarn
Carbon	39	18.3	21.7	9.6	11.4
Basalt	40	20.1	24.9	6.7	8.3
E-glass	41	16.4	20.6	9.7	12.3

5.3 IMPLEMENTATION OF SIMULATING MODELS

Various analytical techniques have been developed to predict thermo-mechanical properties of textile composite RVEs. Two models selected in this study are the mosaic model and the fiber crimp model. The mosaic model provides a convenient and rough estimate of the thermo-elastic properties of fabric composites while the crimp model is suitable for plain weave fabrics. These modeling techniques carry on from averaging of mechanical properties of the constituent materials and the detailed geometric descriptions of the reinforcement. Two methods are used for every model, such as stiffness averaging method and compliance averaging method. For stiffness averaging method, the constitutive equations base upon iso-strain assumption and for compliance averaging method, the constitutive equations base upon iso-stress assumption. The constitutive equations of these models can be used to obtain the bounds of the thermo-elastic properties.

Stiffness averaging method is the one of averaging methods that has attractive feature thanks to continuity of strains or displacements is maintained, although continuity of internal stresses is violated. Bogdanovich et al after comparison a variety of experimental data with various methods of prediction concluded that the stiffness averaging method provides a very good model of elastic properties.

A complementary variant on the stiffness averaging technique is the compliance averaging technique. In this case it is assumed that all components of the materials system are

under constant stress. It can be seen that compliance averaging method satisfies continuity of internal stresses while violates continuity of displacements between the phases.

5.3.1 The mosaic model

Prediction of elastic constants

The basis of idealization of the mosaic model of unit cell can be seen from fig. 5.2a. The key simplification of the mosaic model is the omission of the fiber continuity of undulation (crimp) that exists in an actual fabric. In general, a fabric composite idealized by the mosaic model can be regarded as an assemblage of pieces of asymmetric cross-ply laminates. The elastic stiffness constants of a cross-ply laminate (Fig. 5.2b) can be derived on the basis of equation (3.10), in which Q_{mn} is the stiffness matrix of a unidirectional lamina that has orthotropic symmetry in the xy plane. Assuming that fibers are aligned along the x direction

$$Q_{mn} = \begin{bmatrix} E_L / D_v & \nu_{LT} E_T / D_v & 0 \\ \nu_{TL} E_L / D_v & E_T / D_v & 0 \\ 0 & 0 & G_{LT} \end{bmatrix} \quad (5.9)$$

where $D_v = 1 - \nu_{LT} \nu_{TL}$ (5.10)

Here, E_L and E_T are the Young's moduli, G_{LT} is the in-plane shear modulus, ν_{LT} denotes Poisson's ratio relating the transverse strain in the y direction and the applied strain in the x direction. The Q_{mn} constants are symmetrical, i.e., $Q_{mn} = Q_{nm}$.

From (3.28) to (3.32), we can calculate the elastic properties, including E_L (of warp and weft yarns), E_T , G_{LT} , ν_{LT} , for a unidirectional lamina (combining with fiber volume fraction and matrix volume fraction inside yarn in Table 5.2). Results are presented in Table 5.3.

Table 5.3 Values of unidirectional elastic parameters

Geocomposite with fabrics	$E_{L\text{-warp}}$ [GPa]	$E_{L\text{-weft}}$ [GPa]	E_T [GPa]	ν_{LT}	G_{LT} [GPa]
Carbon	17.2	17.2	9.6	0.16	6.4
Basalt	18.5	18.5	9.4	0.15	6.7
E-glass	14.1	12.8	8.4	0.09	6.3

From eqns. (3.10) and (5.9), the elastic stiffness constants of the cross-ply laminate shown in Fig. 5.2b can be derived. The laminate is composed of two unidirectional laminas of thickness $t/2$. The total laminate thickness is t and the xy coordinate plane is positioned at the

geometrical mid-plane of the laminate. Thus, $j = 1$ and 2 in eqn. (3.10) defines, respectively, lamina with fiber in the y and x directions.

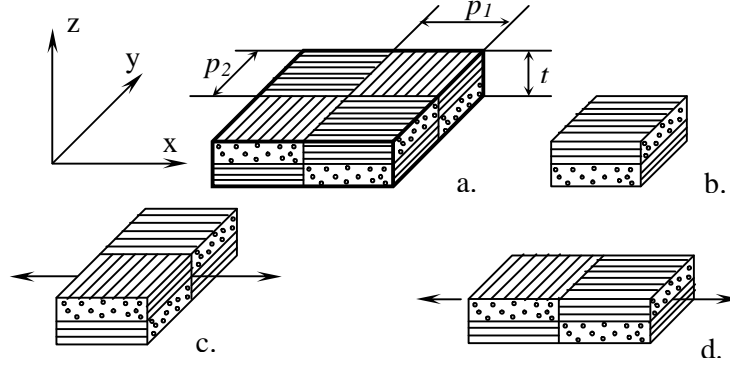


Fig. 5.2 Mosaic model of : a. Unit cell b. The basic cross-ply laminate
c. Parallel model d. Series model

The non-vanishing stiffness constants are

$$\begin{aligned} A_{11} = A_{22} &= (E_L + E_T)t / 2D_v ; & A_{12} &= \nu_{LT} E_T t / D_v ; & A_{66} &= G_{LT} t \\ B_{11} = -B_{22} &= (E_L - E_T)t^2 / 8D_v ; & D_{11} = D_{22} &= (E_L + E_T)t^3 / 24D_v \\ D_{12} &= \nu_{LT} E_T t^3 / 12D_v ; & D_{66} &= G_{LT} t^3 / 12 \end{aligned} \quad (5.11)$$

It is understood that A_{mn} , B_{mn} , D_{mn} are symmetrical constants ($m, n = 1, 2, 6$).

Using eqn. (5.11), the constitutive equations of the basic cross-ply laminate can be rewritten in the following explicit form

$$\begin{Bmatrix} N_x \\ N_y \\ N_{xy} \end{Bmatrix} = \begin{bmatrix} A_{11} & A_{12} & 0 \\ A_{12} & A_{11} & 0 \\ 0 & 0 & A_{66} \end{bmatrix} \begin{Bmatrix} \varepsilon_x^o \\ \varepsilon_y^o \\ \gamma_{xy}^o \end{Bmatrix} + \begin{bmatrix} B_{11} & 0 & 0 \\ 0 & -B_{11} & 0 \\ 0 & 0 & 0 \end{bmatrix} \begin{Bmatrix} k_x \\ k_y \\ k_{xy} \end{Bmatrix} \quad (5.12a)$$

$$\begin{Bmatrix} M_x \\ M_y \\ M_{xy} \end{Bmatrix} = \begin{bmatrix} B_{11} & 0 & 0 \\ 0 & -B_{11} & 0 \\ 0 & 0 & 0 \end{bmatrix} \begin{Bmatrix} \varepsilon_x^o \\ \varepsilon_y^o \\ \gamma_{xy}^o \end{Bmatrix} + \begin{bmatrix} D_{11} & D_{12} & 0 \\ D_{12} & D_{11} & 0 \\ 0 & 0 & D_{66} \end{bmatrix} \begin{Bmatrix} k_x \\ k_y \\ k_{xy} \end{Bmatrix} \quad (5.12b)$$

Inverting eqn. (5.12), we obtain

$$\begin{Bmatrix} \varepsilon_x^o \\ \varepsilon_y^o \\ \gamma_{xy}^o \end{Bmatrix} = \begin{bmatrix} a_{11} & a_{12} & 0 \\ a_{12} & a_{11} & 0 \\ 0 & 0 & a_{66} \end{bmatrix} \begin{Bmatrix} N_x \\ N_y \\ N_{xy} \end{Bmatrix} + \begin{bmatrix} b_{11} & 0 & 0 \\ 0 & -b_{11} & 0 \\ 0 & 0 & 0 \end{bmatrix} \begin{Bmatrix} M_x \\ M_y \\ M_{xy} \end{Bmatrix} \quad (5.13a)$$

$$\begin{Bmatrix} k_x \\ k_y \\ k_{xy} \end{Bmatrix} = \begin{bmatrix} b_{11} & 0 & 0 \\ 0 & -b_{11} & 0 \\ 0 & 0 & 0 \end{bmatrix} \begin{Bmatrix} N_x \\ N_y \\ N_{xy} \end{Bmatrix} + \begin{bmatrix} d_{11} & d_{12} & 0 \\ d_{12} & d_{11} & 0 \\ 0 & 0 & d_{66} \end{bmatrix} \begin{Bmatrix} M_x \\ M_y \\ M_{xy} \end{Bmatrix} \quad (5.13b)$$

According to the iso-strain or iso-stress conditions, the unit cell of the two-dimensional extent is simplified by considering two one-dimensional models where the pieces of cross-ply laminates are either in parallel or in series as shown in Figs. 5.2c and d. In the parallel model, a uniform state of strain, ε_m^o , and curvature, k , in the laminate midplane is assumed as a first approximation. For the one-dimensional repeating region of length $2p_1$ or $2p_2$, where p_1 or p_2 denotes the warp or weft yarn width, the average stress resultants can be written in a form

$$\begin{aligned} \overline{N}_x &= \frac{1}{2p_2} \int_0^{2p_2} N_x dy = A_{11}\varepsilon_x^o + A_{12}\varepsilon_y^o \quad ; \quad \overline{N}_y = \frac{1}{2p_1} \int_0^{2p_1} N_y dx = A_{12}\varepsilon_x^o + A_{11}\varepsilon_y^o \\ \overline{N}_{xy} &= \frac{1}{2p_2} \int_0^{2p_2} N_{xy} dy = A_{66}\gamma_{xy}^o \quad ; \quad \overline{M}_x = \frac{1}{2p_2} \int_0^{2p_2} M_x dy = D_{11}k_x + D_{12}k_y \\ \overline{M}_y &= \frac{1}{2p_1} \int_0^{2p_1} M_y dx = D_{12}k_x + D_{11}k_y \quad ; \quad \overline{M}_{xy} = \frac{1}{2p_2} \int_0^{2p_2} M_{xy} dy = D_{66}k_{xy} \end{aligned} \quad (5.14)$$

Here, after integration, the term B_{II} is vanished itself. Therefore, in the parallel model the constitutive equations can be rewritten in a compact form

$$\begin{bmatrix} \overline{N} \\ \overline{M} \end{bmatrix} = \begin{bmatrix} \overline{A} & 0 \\ 0 & \overline{D} \end{bmatrix} \cdot \begin{bmatrix} \varepsilon_m^o \\ k \end{bmatrix} \quad (5.15)$$

where \overline{A} , \overline{D} are the effective extensional stiffness matrix and the effective bending stiffness matrix for unit cell. Here: $\overline{A}_{mn} = A_{mn}$; $\overline{D}_{mn} = D_{mn}$ are determined thanks to equations (5.11).

In the series model, the disturbance of stress and strain near the interface of the interfaced region is neglected. The assumption of constant stress leads to the definition of the average midplane strain, ε_m^o , and curvature, \overline{k} . For instance, if the model is subjected to a uniform in-plane force, N_x , in the longitudinal direction, the average curvature, \overline{k}_x , along the x direction is

$$\bar{k}_x = \frac{1}{2p_1} \int_0^{2p_1} k_x dx = \frac{1}{2p_1} \left[\int_0^{p_1} b_{11} N_x dx + \int_{p_1}^{2p_1} b_{11} N_x dx \right] = 0 \quad (5.16)$$

Other average curvature and midplane strain expressions can be written similar to eqn. (5.16) for uniformly applied N and M . Let \bar{a}_{mn} , \bar{b}_{mn} , \bar{d}_{mn} be the effective compliance constant relating the average midplane strain, $\bar{\epsilon}_m^o$, and curvature, \bar{k} , with the stress resultant, N , and moment resultant, M . Thus, in the series model the constitutive equations can be rewritten in a compact form

$$\begin{bmatrix} \bar{\epsilon}_m^o \\ \bar{k} \end{bmatrix} = \begin{bmatrix} \bar{a} & 0 \\ 0 & \bar{d} \end{bmatrix} \cdot \begin{bmatrix} N \\ M \end{bmatrix} \quad (5.17)$$

Also, after integration, the term b_{11} is vanished itself and $\bar{a}_{mn} = a_{mn}$; $\bar{d}_{mn} = d_{mn}$. From the condition: $\bar{a} = \bar{A}^{-1}$ and $\bar{d} = \bar{D}^{-1}$, it will lead to $\bar{a} = \bar{A}^{-1}$ and $\bar{d} = \bar{D}^{-1}$. Thus, the parallel model is equivalent to the series.

The effective elastic modulus of unit cell in x , y directions and the Poisson's ratio can be derived from eqn. (5.17) in the case of $N_x \neq 0$ and $N_{xy} = N_y = 0$

We have $\epsilon_x^o = a_{11} N_x$ and $\epsilon_y^o = a_{12} N_x$ leads to

$$E_x = \frac{N_x / t}{\epsilon_x^o} = \frac{1}{t a_{11}} = \frac{1}{t} \left(A_{11} - \frac{A_{12}^2}{A_{11}} \right) = E_y \quad (5.18)$$

$$\text{and } \nu_{xy} = -\frac{\epsilon_y^o}{\epsilon_x^o} = -\frac{a_{12}}{a_{11}} = \frac{A_{12}}{A_{11}} \quad (5.19)$$

Similarly, the effective in-plane shear modulus of unit cell is determined in the case of $N_{xy} \neq 0$ and $N_x = N_y = 0$

$$\text{We have } \gamma_{xy}^o = a_{66} N_{xy} \text{ leads to } G_{xy} = \frac{N_{xy} / t}{\gamma_{xy}^o} = \frac{1}{t a_{66}} = \frac{A_{66}}{t} \quad (5.20)$$

Substituting eqns. (5.11) into (5.18)-(5.20), we obtain

$$E_x = \frac{E_L + E_T}{2D_v} - \frac{2\nu_{LT}^2 E_T^2}{D_v (E_L + E_T)} \quad (5.21)$$

$$E_y = \frac{E_L + E_T}{2D_v} - \frac{2\nu_{LT}^2 E_T^2}{D_v (E_L + E_T)} \quad (5.22)$$

$$v_{xy} = \frac{2\nu_{LT}E_T}{E_L + E_T} ; G_{xy} = G_{LT} \quad (5.23)$$

Note that E_x is respective to $E_{L\text{-weft}}$, E_y is respective to $E_{L\text{-warp}}$.

Prediction of thermal expansion coefficients

The constitutive equations of a laminated plate taking into account the effects due to a small uniform temperature change are given in eqns. (3.22) and (3.23). Inverting eqn. (3.22) we can calculate the midplane strain and curvature in the terms of thermal force and moment resultants.

$$\begin{bmatrix} \boldsymbol{\varepsilon}_m^o \\ \mathbf{k} \end{bmatrix} = \begin{bmatrix} \mathbf{a} & \mathbf{b} \\ \mathbf{b} & \mathbf{d} \end{bmatrix} \begin{bmatrix} \mathbf{N}^T \\ \mathbf{M}^T \end{bmatrix} \quad (5.24)$$

$$\text{From eqns. (3.23a) and (3.23b) we can rewrite } \begin{bmatrix} \mathbf{N}^T \\ \mathbf{M}^T \end{bmatrix} = \Delta T \begin{bmatrix} \widetilde{\mathbf{A}} \\ \widetilde{\mathbf{B}} \end{bmatrix} \quad (5.25)$$

$$\text{where } \widetilde{\mathbf{A}}_m = \sum_{j=1}^2 (Q_{mn})_j (\alpha_n)_j (h_j - h_{j-1}) ; \widetilde{\mathbf{B}}_m = \sum_{j=1}^2 \frac{1}{2} (Q_{mn})_j (\alpha_n)_j (h_j^2 - h_{j-1}^2) \quad (5.26)$$

$$(m, n = 1, 2, 6)$$

Substituting eqn. (5.24) into (5.25), we get

$$\begin{bmatrix} \boldsymbol{\varepsilon}_m^o \\ \mathbf{k} \end{bmatrix} = \begin{bmatrix} \mathbf{a} & \mathbf{b} \\ \mathbf{b} & \mathbf{d} \end{bmatrix} \Delta T \begin{bmatrix} \widetilde{\mathbf{A}} \\ \widetilde{\mathbf{B}} \end{bmatrix} = \Delta T \begin{bmatrix} \widetilde{\mathbf{a}} \\ \widetilde{\mathbf{b}} \end{bmatrix} \quad (5.27)$$

$$\text{where } \begin{bmatrix} \widetilde{\mathbf{a}} \\ \widetilde{\mathbf{b}} \end{bmatrix} = \begin{bmatrix} \mathbf{a} & \mathbf{b} \\ \mathbf{b} & \mathbf{d} \end{bmatrix} \begin{bmatrix} \widetilde{\mathbf{A}} \\ \widetilde{\mathbf{B}} \end{bmatrix} \quad (5.28)$$

The average strains and curvatures of one-dimensional strip of width p_1 or p_2 in Fig. 5.2a along the weft or warp direction due to a uniform temperature change, ΔT , can be expressed in the following forms:

$$\overline{\varepsilon}_i^o = \frac{1}{2p} \int_0^{2p} \Delta T \widetilde{a}_i(\xi) d\xi = \Delta T \widetilde{a}_i \quad (i = 1, 2) \quad (5.28)$$

$$\overline{k}_i = \frac{1}{2p} \int_0^{2p} \Delta T \widetilde{b}_i(\xi) d\xi = 0 \quad (i = 1, 2) \quad (5.29)$$

Because of the nature of the cross-ply laminates \widetilde{a}_6 and \widetilde{b}_6 vanish. From eqn. (5.29), it can be stated that the average curvatures of unit cell due to thermal equal zero if based on the mosaic

model. Also, from eqn. (5.28), we can derive the average thermal expansion for the mosaic model.

$$\alpha_x = \frac{\overline{\varepsilon_1^0}}{\Delta T} = \tilde{a}_1 = \frac{E_L \alpha_L + E_T \alpha_T + \nu_{LT} E_T (\alpha_L + \alpha_T)}{E_L + E_T + 2\nu_{LT} E_T} \quad (5.30)$$

$$\alpha_y = \frac{\overline{\varepsilon_2^0}}{\Delta T} = \tilde{a}_2 = \frac{E_L \alpha_L + E_T \alpha_T + \nu_{LT} E_T (\alpha_L + \alpha_T)}{E_L + E_T + 2\nu_{LT} E_T} \quad (5.31)$$

Also, note that α_x is respective to E_{L-weft} , α_y is respective to E_{L-warp} . Here, α_L , α_T are CTEs of yarns in the longitudinal and transverse directions and can be calculated by eqn. (3.33).

Table 5.4 shows CTEs of carbon yarn, basalt yarn, E-glass yarn.

Table 5.4 CTEs of carbon yarn, basalt yarn, E-glass yarn

Materials	CTE of fibers α_f [$1/^\circ\text{C}$]	CTE of yarns	
		α_L [$1/^\circ\text{C}$]	$\alpha_T = \alpha_T^*$ [$1/^\circ\text{C}$]
Carbon	1.8×10^{-6}	5.0×10^{-6}	3.2×10^{-6}
Basalt	8.0×10^{-6}	9.7×10^{-6}	6.1×10^{-6}
E-glass	5.4×10^{-6}	7.9×10^{-6}	4.6×10^{-6}

5.3.2 The crimp model

Prediction of elastic constants

The crimp model is developed in order to consider continuity and undulations of fibers in a fabric composite. To calculate the elastic and thermal properties of lamina reinforced woven fabrics, we need to determine elastic and thermal properties of for unidirectional tows in unit cell. After that we apply the stiffness averaging method or the compliance averaging method and thermal expansion averaging method for unit cell in lamina.

The stiffness averaging method as well as the compliance averaging method consists of subdividing the reinforcement system into distinct sets of rods (yarns) in a unit cell. Each yarn sub-system is considered to be a unidirectional composite with some spatial orientation. The individual yarn sub-systems are assumed to interact with each other, and the unit cell as a whole is assumed to be subjected to a constant strain state (for the stiffness averaging method) or a constant stress state (for the compliance averaging method).

Stiffness averaging method is based on averaging of mechanical properties of the constituent materials associated with detailed geometric descriptions of each constituent. This method is attractive with keeping continuity of strains although continuity of internal stress is

violated. Intuitively, from mechanic point of view, less error should be realized when maintaining continuity of displacements only than when maintaining continuity of stresses only [44].

After describing geometry of the unit cell with a consideration of the crimp parameters, we can apply the stiffness averaging method and the compliance averaging method for predicting elastic properties of unit cell in the following steps:

- Dividing every half of yarns in a unit cell into 10 elements ($n = 10$). (See Fig. 5.1b)
- Each yarn element is considered to be a unidirectional composite (or a rod) with the same elastic properties.
- Using the in-plane elastic properties in Table 5.3 and adding more hypotheses to calculate the out-plane elastic properties.

$$E_{T'} = E_T \quad ; \quad G_{LT'} = G_{LT} \quad ; \quad G_{TT'} = \frac{E_T}{2(1+v_{TT'})} \quad ;$$

$$v_{LT'} = v_{LT} \quad ; \quad v_{TT'} = v_m \quad (5.32)$$

where v_m is Poisson's ratio of matrix (see Table 5.5).

Table 5.5 The material parameters of geopolymer

Extension modulus E_m [GPa]	Shear modulus G_m [GPa]	Poisson's ratio v_m	Strength in tension σ_{mu}^T [MPa]	Strength in compression σ_{mu}^C [MPa]	Thermal expansion coefficient α [$1/^\circ\text{C}$]
11.7	5.6	0.05	27.8	88.9	15.0×10^{-6}

- Construct the local unidirectional compliance and stiffness matrices $S_{yarn}^{(i)}$, $C_{yarn}^{(i)}$ from the elastic properties of unidirectional rod.

$$S_{yarn}^{(i)} = \begin{bmatrix} 1/E_L & -v_{TL}/E_T & -v_{T'L}/E_T & 0 & 0 & 0 \\ -v_{LT}/E_L & 1/E_T & -v_{T'T}/E_T & 0 & 0 & 0 \\ -v_{LT'}/E_L & -v_{TT'}/E_T & 1/E_T & 0 & 0 & 0 \\ 0 & 0 & 0 & 1/G_{TT'} & 0 & 0 \\ 0 & 0 & 0 & 0 & 1/G_{LT'} & 0 \\ 0 & 0 & 0 & 0 & 0 & 1/G_{LT} \end{bmatrix} \quad (5.33)$$

$$C_{yarn}^{(i)} = (S_{yarn}^{(i)})^{-1} \quad (5.34)$$

- Setting the local coordinate system (1, 2, 3) associated with the i^{th} element, see Fig. 5.1b, and establishing the strain and stress transformation matrices \mathbf{T}_ε , \mathbf{T}_σ between the local coordinate system and the global coordinate system (x, y, z).

$$\mathbf{T}_\varepsilon = \begin{bmatrix} l_1^2 & m_1^2 & n_1^2 & m_1 n_1 & n_1 l_1 & l_1 m_1 \\ l_2^2 & m_2^2 & n_2^2 & m_2 n_2 & n_2 l_2 & l_2 m_2 \\ l_3^2 & m_3^2 & n_3^2 & m_3 n_3 & n_3 l_3 & l_3 m_3 \\ 2l_2 l_3 & 2m_2 m_3 & 2n_2 n_3 & m_2 n_3 + n_2 m_3 & l_2 n_3 + n_2 l_3 & l_2 m_3 + m_2 l_3 \\ 2l_1 l_3 & 2m_1 m_3 & 2n_1 n_3 & m_1 n_3 + n_1 m_3 & l_1 n_3 + n_1 l_3 & l_1 m_3 + m_1 l_3 \\ 2l_1 l_2 & 2m_1 m_2 & 2n_1 n_2 & m_1 n_2 + n_1 m_2 & l_1 n_2 + n_1 l_2 & l_1 m_2 + m_1 l_2 \end{bmatrix} \quad (5.35)$$

$$\mathbf{T}_\sigma = \begin{bmatrix} l_1^2 & m_1^2 & n_1^2 & 2m_1 n_1 & 2n_1 l_1 & 2l_1 m_1 \\ l_2^2 & m_2^2 & n_2^2 & 2m_2 n_2 & 2n_2 l_2 & 2l_2 m_2 \\ l_3^2 & m_3^2 & n_3^2 & 2m_3 n_3 & 2n_3 l_3 & 2l_3 m_3 \\ l_2 l_3 & m_2 m_3 & n_2 n_3 & m_2 n_3 + n_2 m_3 & l_2 n_3 + n_2 l_3 & l_2 m_3 + m_2 l_3 \\ l_1 l_3 & m_1 m_3 & n_1 n_3 & m_1 n_3 + n_1 m_3 & l_1 n_3 + n_1 l_3 & l_1 m_3 + m_1 l_3 \\ l_1 l_2 & m_1 m_2 & n_1 n_2 & m_1 n_2 + n_1 m_2 & l_1 n_2 + n_1 l_2 & l_1 m_2 + m_1 l_2 \end{bmatrix} \quad (5.36)$$

where the general linear orthogonal coordinate transformation matrix of the local system {1, 2, 3} to the global system {x, y, z} to has the form:

$$\mathbf{M} = \begin{bmatrix} l_1 & m_1 & n_1 \\ l_2 & m_2 & n_2 \\ l_3 & m_3 & n_3 \end{bmatrix} \quad (5.37)$$

For elements belong to the weft yarn system (Fig. 5.3a):

$$\mathbf{M}_{\text{weft}}^{(i)} = \begin{bmatrix} \cos(\alpha_i) & 0 & \sin(\alpha_i) \\ 0 & 1 & 0 \\ -\sin(\alpha_i) & 0 & \cos(\alpha_i) \end{bmatrix} \quad (5.38)$$

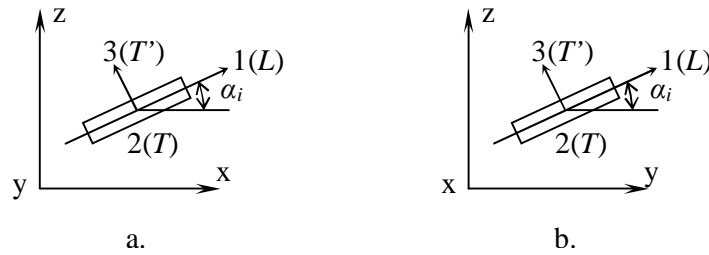


Fig. 5.3 Direction of yarn element in the global system:

a. Weft yarn; b. Warp yarn

For elements belong to the warp yarn system (Fig. 5.3b):

$$\mathbf{M}_{warp}^{(i)} = \begin{bmatrix} 0 & \cos(\alpha_i) & \sin(\alpha_i) \\ 1 & 0 & 0 \\ 0 & -\sin(\alpha_i) & \cos(\alpha_i) \end{bmatrix} \quad (5.39)$$

- Calculate the global compliance and stiffness matrices $\mathbf{S}_{g-yarn}^{(i)}$, $\mathbf{C}_{g-yarn}^{(i)}$ of the unidirectional yarn elements thanks to the strain and stress transformation matrices \mathbf{T}_ε , \mathbf{T}_σ :

$$\mathbf{S}_{g-yarn}^{(i)} = \mathbf{T}_\varepsilon \cdot \mathbf{S}_{yarn}^{(i)} \mathbf{T}_\varepsilon^{-1} ; \mathbf{C}_{g-yarn}^{(i)} = \mathbf{T}_\sigma \cdot \mathbf{C}_{yarn}^{(i)} \mathbf{T}_\sigma^{-1} \quad (5.40)$$

- Average volumetrically the compliance and stiffness matrices of all unidirectional elements and proportion of matrix between yarns to obtain the total compliance and stiffness matrices \mathbf{S}_t , \mathbf{C}_t :

$$\mathbf{S}_t = \sum_{i=1}^{10} (4k_{warp} \mathbf{S}_{g-warp}^{(i)} + 4k_{weft} \mathbf{S}_{g-weft}^{(i)}) + k_m \mathbf{S}_{g-matrix} \quad (5.41)$$

$$\mathbf{C}_t = \sum_{i=1}^{10} (4k_{warp} \mathbf{C}_{g-warp}^{(i)} + 4k_{weft} \mathbf{C}_{g-weft}^{(i)}) + k_m \mathbf{C}_{g-matrix} \quad (5.42)$$

where $\mathbf{S}_{g-matrix}$, $\mathbf{C}_{g-matrix}$ are the global compliance and stiffness of proportion of matrix between yarns and are independent on coordinate system.

k_{warp} and k_{weft} are the relative volumetric proportion of the warp and weft yarn subsystem in unit cell; k_m is the relative volumetric proportion of matrix between yarns in unit cell. k_{warp} , k_{weft} , k_m can be determined by following and shown in Table 5.6.

$$k_{warp} = \frac{A_1 l_1}{20 \Omega_c} ; k_{weft} = \frac{A_2 l_2}{20 \Omega_c} ; k_m = 1 - 40(k_{warp} + k_{weft}) \quad (5.43)$$

Here, A_1 , A_2 , l_1 , l_2 , Ω_c are referred from the eqns. (5.3), (5.4), and (5.7).

Table 5.6 Values of relative volumetric factors

Unit cell of geocomposites with fabrics	k_{warp}	k_{weft}	k_m
Carbon	0.00840	0.00840	0.3280
Basalt	0.00835	0.00835	0.3320
E-glass	0.00840	0.00839	0.3284

- Inverting of \mathbf{C}_t , we get the total compliance matrix of unit cell from the stiffness averaging method

$$S_t^* = (C_t)^{-1} \quad (5.44)$$

Note that $S_t^* \neq S_t$

- From the two global compliance matrices of unit cell, we obtain elastic properties:

$$E_x = \frac{1}{S_{11}} ; \quad E_y = \frac{1}{S_{22}} ; \quad \nu_{xy} = -\frac{S_{12}}{S_{22}} ; \quad G_{xy} = \frac{1}{S_{66}} \quad (5.45)$$

$$E_x = \frac{1}{S_{11}^*} ; \quad E_y = \frac{1}{S_{22}^*} ; \quad \nu_{xy} = -\frac{S_{12}^*}{S_{22}^*} ; \quad G_{xy} = \frac{1}{S_{66}^*} \quad (5.46)$$

Prediction of thermal expansion coefficients

Similar to calculation of elastic constants of unit cell, the determination of unit cell thermal expansion coefficients bases on the thermal expansion averaging of elements in unit cell.

The thermal expansion coefficient vector of a unidirectional yarn element in the local system can be written in a form:

$$\alpha_{yarn}^{(i)} = (\alpha_L, \alpha_T, \alpha_T, 0, 0, 0)^T \quad (5.47)$$

The thermal expansion coefficient vector of a unidirectional yarn element in the global system is determined thanks to the strain transformation matrix, T_ε .

$$\alpha_{g-yarn}^{(i)} = T_\varepsilon^{-1} \alpha_{yarn}^{(i)} \quad (5.48)$$

The total thermal expansion coefficient of unit cell is calculated as averaging volumetrically the thermal expansion coefficients of all unidirectional elements and proportion of matrix between yarns.

$$\alpha_t = \sum_{i=1}^{10} (4k_{warp} \alpha_{g-warp}^{(i)} + 4k_{weft} \alpha_{g-weft}^{(i)}) + k_m \alpha_{g-matrix} \quad (5.49)$$

where $\alpha_{g-matrix}$ is the global thermal expansion coefficient of matrix between yarns.

Finally, the thermal expansion coefficients of unit cell are:

$$\alpha_x = \alpha_{t1} ; \quad \alpha_y = \alpha_{t2} ; \quad \alpha_z = \alpha_{t3} \quad (5.50)$$

5.3.3 Result and Discussion

The results received from the mosaic and crimp models are listed in Table 5.7. Matlab functions used in the crimp model can be seen in Appendix B.2-B.4.

Table 5.7 Analytical and experimental results for composites

Material parameters of unit cell of geopolymer with fabrics		The mosaic model	The crimp model		The experiment
			From the averaging stiffness method	From the averaging compliance method	
Carbon	E_x [GPa]	13.4	12.9	12.1	12.5
	E_y [GPa]	13.4	12.9	12.1	12.6
	G_{xy} [GPa]	6.4	6.1	6.1	5.0
	ν_{xy}	0.12	0.09	0.09	---
	α_x [1/°C]	4.33×10^{-6}	7.67×10^{-6}		---
	α_y [1/°C]	4.33×10^{-6}	7.67×10^{-6}		---
	α_z [1/°C]	---	7.08×10^{-6}		3.28×10^{-4}
Basalt	E_x [GPa]	14.0	13.2	12.2	11.3
	E_y [GPa]	14.0	13.2	12.2	10.2
	G_{xy} [GPa]	6.7	6.3	6.3	---
	ν_{xy}	0.10	0.09	0.08	---
	α_x [1/°C]	8.43×10^{-6}	10.25×10^{-6}		---
	α_y [1/°C]	8.43×10^{-6}	10.25×10^{-6}		---
	α_z [1/°C]	---	9.06×10^{-6}		15.72×10^{-4}
E-glass	E_x [GPa]	10.6	11.0	10.6	8.5
	E_y [GPa]	11.3	11.4	10.9	9.6
	G_{xy} [GPa]	6.3	6.1	6.0	5.0
	ν_{xy}	0.07	0.06	0.06	---
	α_x [1/°C]	6.57×10^{-6}	9.11×10^{-6}		---
	α_y [1/°C]	6.64×10^{-6}	9.11×10^{-6}		---
	α_z [1/°C]	---	8.04×10^{-6}		14.77×10^{-4}

As can be seen, in comparison with experiment, the mosaic and crimp models give results reliably. The differences between the models are relatively small across the entire range of elastic parameters maybe due to very low fabric undulation. However, for the mosaic model, because the fabric composite is idealized as an assemblage of pieces of asymmetric cross-ply, it looks like harder, so the elastic parameter values is highest. The crimp model, which is a one-dimensional approximation and takes into account fiber continuity and undulation, is particularly suited for predicting elastic properties of plain weave composites. The analytical results based upon the crimp model demonstrate that fiber undulation leads to a softening in the in-plane stiffness as compared to the mosaic model. Although the two of the averaging methods with contrary meaning are used in the crimp model, but the upper bound (for the averaging stiffness method) and lower bound (for the averaging compliance method) of elastic

parameters are not much distinct, maybe due to very low fabric undulation. Lastly, we can see that the differences between thermal expansion coefficients of composite from models and from experiment are very big.

5.4 FEM IMPLEMENTATION WITH ANSYS AND TEXGEN

The complex structure of textile composite comprises several hierarchical levels: macro (composite component or sub-component) – meso (unit cell of the reinforcement structure) –micro (fiber placement inside yarns and fibrous plies). The most specific to textile composites is meso-level, where the structure-dependent behavior of the material is most pronounced [62]. TexGen is a software package of modeling the 3D geometry of textiles at the level of the unit cell [63]. TexGen is designed to be flexible and multi-functional aiming to be able to accurately model as many types of textiles as possible (e.g. woven, knitted, knotted, non-woven, etc...) with as many techniques as possible (e.g. finite element method, finite difference method) for applications such as solid mechanics. Ansys is a scientific and CAE design analysis software environment for the modeling and simulation of any problem of physics. This software allows analyzing easily deformation and stress in a unit cell exported from TexGen. Combination of two softwares is used to predict and to verify behavior as well as failure of composite materials.

5.4.1 Model of internal architecture of woven laminate in 3-D geometry

A geometrical model of woven fabric can describe actual placement of the yarns in unit cell space and can calculate dimensions and waviness (crimp) of the yarns. The data inputs are given to the geometrical model: type of interlacing, number of warp yarns and weft yarns and number of layers in a unit cell, yarn width, yarn height, shape of yarn cross section, fabric thickness... All the parameters can be showed in a unit cell by TexGen software.

In order to save time and memory of a computer, two geometrical models used in a research are unit cell with two skew-symmetrical layers and with symmetrical layers (Fig. 5.4). Both models used the geometrical parameters in Table 5.1. The cross section of yarns was assumed elliptical shape.

5.4.2 Mechanical properties of constituents in a repeating unit cell

The matrix encompassing yarns are considered isotropic material while the yarns in a unit cell are attributed orthotropic. Assuming that combination fibers and resin with a good adhesion is illustrated in fig. 3.9 in the chapter 3. The five ultimate strength parameters for a yarn within the unit cell are also necessary to calculate from the individual properties of the fiber and matrix according to equations from (3.34) to (3.39) and shown in Tablet 5.8. The material parameters of resin can be also listed in Table 5.5.

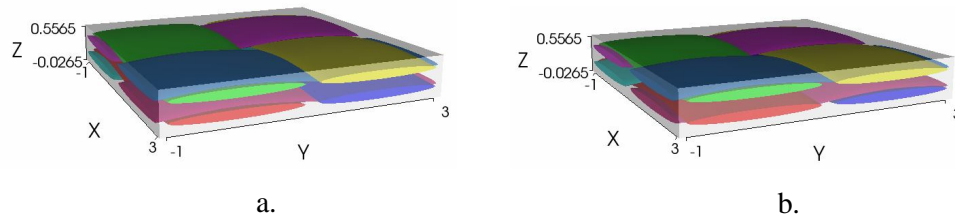


Fig. 5.4 The geometrical models of a repeating unit cell of composite with carbon fabric

a. Two skew-symmetrical layers b. Two symmetrical layers

Table 5.8 The strengths of yarns in geocomposites

Geocomposites with fabrics	Strength of warp yarns					Strength of weft yarns				
	σ_{Lu}^T [MPa]	σ_{Lu}^C [MPa]	σ_{Tu}^T [MPa]	σ_{Tu}^C [MPa]	σ_{LTu} [MPa]	σ_{Lu}^T [MPa]	σ_{Lu}^C [MPa]	σ_{Tu}^T [MPa]	σ_{Tu}^C [MPa]	σ_{LTu} [MPa]
Carbon	122	395	36	261	19	are the same as strength of warp yarns				
Basalt	101	348	27	195	19					
E-glass	64	523	28	207	20	53	474	28	207	20

5.4.3 Prediction of geocomposite elastic properties in tension

After creating geometric models of a unit cell, we import them to Ansys and assigned mechanical properties to the yarns and the matrix. The next steps are to mesh the parts in the model and to make boundary conditions. Models are meshed with total 36173 nodes and 40701 elements. The boundary conditions can be described as followings: for two faces that are orthogonal to x-axis, one face is fixed in the x-direction while the other moves translationally in the x-direction. Models are solved in a linear manner. Outputs from models are:

- $\sum RF_x$ is the total reaction force at the displaced edge. From this, the average stress in the x-direction in a unit cell is calculated

$$\sigma_{ave} = \frac{\sum RF_x}{w_c \cdot t_c} \quad (5.51)$$

where $w_c = 2p$; $t_c = 2t$ are the width and thickness of a unit cell with two layers.

- The average strain in the x-direction in a unit cell are also calculated

$$\varepsilon_{ave} = \frac{\delta w_c}{w_c} \quad , \quad \text{where } \delta w_c \text{ is the prescribed displacement}$$

- The Young modulus is determined: $E = \frac{\sigma_{ave}}{\varepsilon_{ave}}$ (5.52)
- A failure index is calculated at each point for matrix and yarns:

$$FI_m = \frac{\sigma_{vonMise}^T}{\sigma_{mu}}, \quad FI_y = F_1\sigma_x + F_2\sigma_y + F_{11}\sigma_x^2 + F_{22}\sigma_y^2 + F_{66}\tau_{xy}^2 + 2F_{12}\sigma_x\sigma_y \quad (5.53)$$

where FI_m is the VonMise criterion for matrix and FI_y is the Tsai-Wu criterion for yarns; the factors $F_1, F_2, F_{11}, F_{22}, F_{66}, F_{12}$ are determined in accordance with (3.42) and using parameters in Table 5.8 and 5.5.

After repeating to prescribe the x-displacements (δw_c) to the unit cell with values: 0.01 mm, 0.02 mm, ...0.1 mm and solving the problem by Ansys, we obtained the total reaction force at the displacement edge of the cell, the longitudinal and transverse stresses at a point in cell, the failure indices at each point in matrix and in yarns. Finally, we calculated the average strains and stresses in the cell.

Figure 5.5 shows tension graphs of geocomposite reinforced carbon fabric from experiment and from simulation. We can realize that the behaviors of geocomposite from simulation of two geometrical models (skew-symmetrical and symmetrical two-layer placements) are nearly similar with the same elastic modulus and equivalent to elastic modulus measured from experiment. However, if observing totally, these behaviors rather differ because the graph from experiment has nonlinear tendency.

Thanks to failure indices FI_m and FI_y as well as crimp value of fabric, tension behavior of geocomposite materials can be divided into four stages: damage of surrounding resin corresponding to $FI_m = 1$, process of fabric de-crimp, failure of yarns corresponding to $FI_y = 1$ and total damage stage. With carbon geocomposite: $\varepsilon_I = 0.0018$, $\sigma_I = 23$ MPa ; $\varepsilon_{II} = 0.0035$, $\sigma_{II} = 45$ MPa ; $\varepsilon_{III} = 0.0138$, $\sigma_{III} = 178$ MPa.

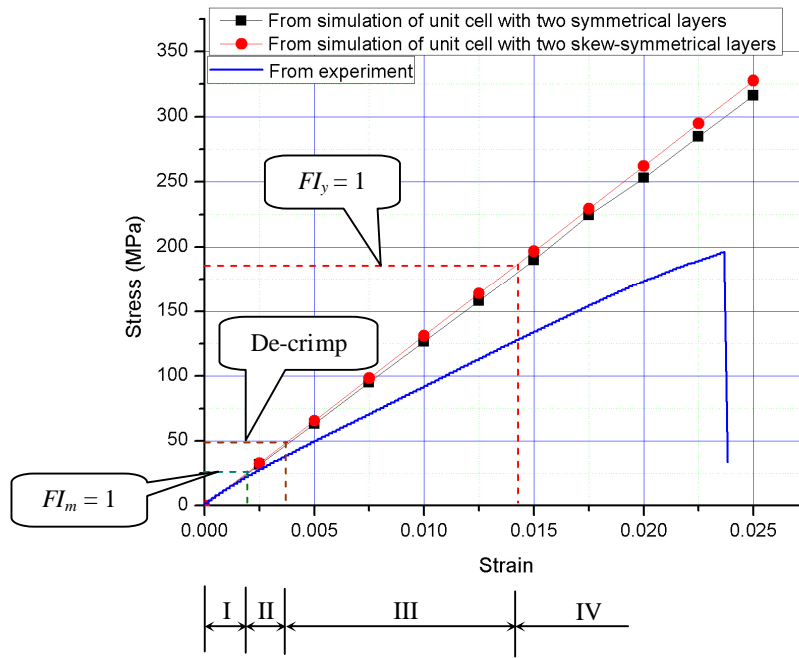


Fig. 5.5 Tension graphs of carbon geocomposites

Figure 5.6 describes spectra of distribution of Von-Mise stress on matrix and tension stress on yarns. We can see that the maximum stresses occur in matrix and longitudinal yarns, where are the middle of transverse yarns. Additionally, when observing two fabric layers, we can see also that tensile load shares equally on them, but in each layer the longitudinal yarns are mainly subjected loads.

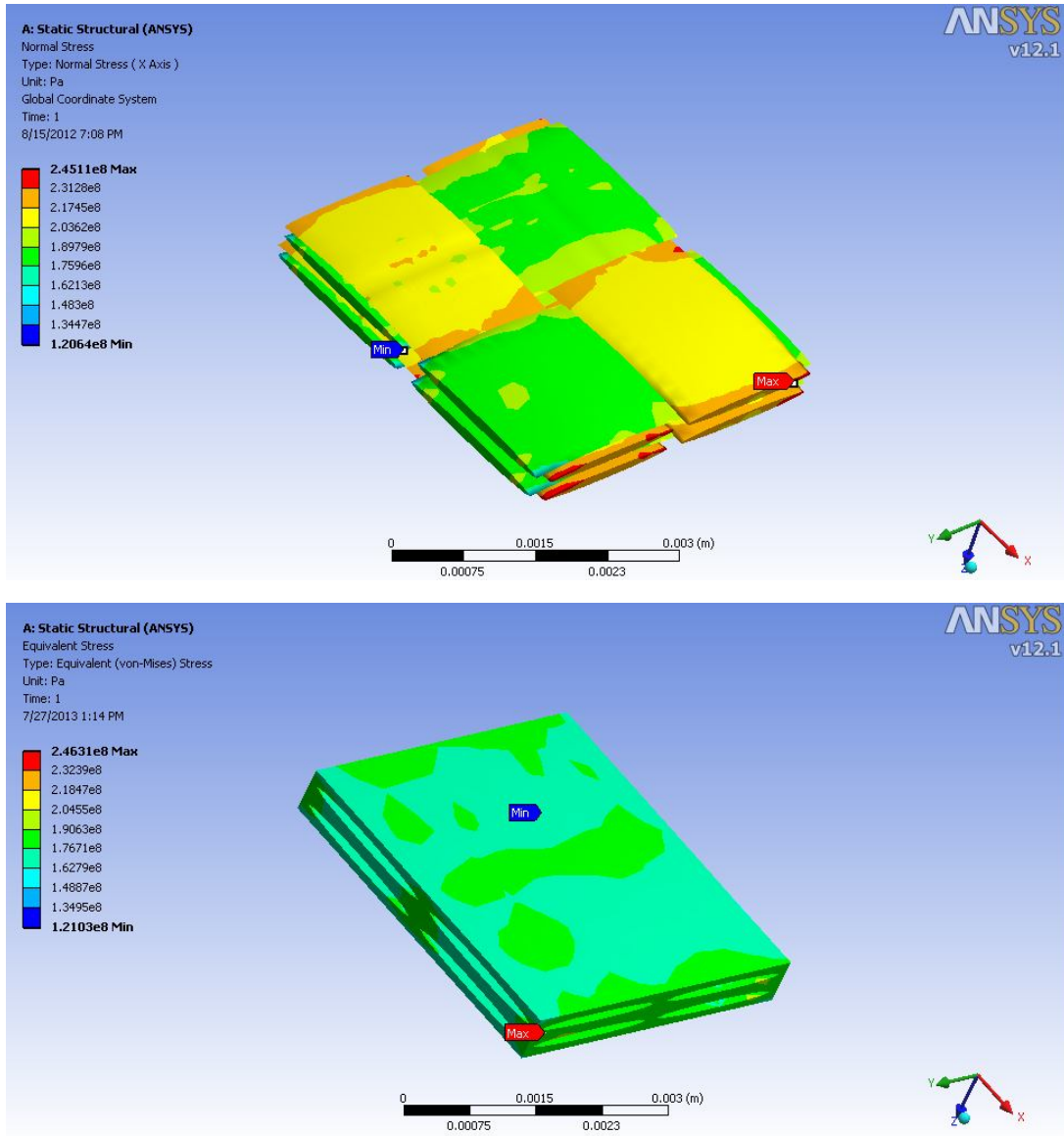


Fig. 5.6 The spectra of distribution of Von-Mise stress on matrix (below) and tension stress on yarns (above) in tensile model.

Such a procedure of elastic properties prediction is also applied for two geocomposites with basalt and E-glass fabrics. In a final, we obtain tensile material parameters shown in Table 5.9. In comparison with experiment data, we can see that the material parameters obtained from simulations are quite consistent with experiment for geopolymers reinforced carbon and E-glass fabrics. However, the strain at the ultimate stress is much lower than experiment. This can be understood that the specimen could slip at grips.

Table 5.9 Tensile properties of geocomposites from simulation

Geocomposites with	Mechanical properties in a warp direction			Mechanical properties in a weft direction		
	R_{mt} [MPa]	E [GPa]	ϵ_{mt} [%]	R_{mt} [MPa]	E [GPa]	ϵ_{mt} [%]
Carbon	178	13.0	1.37	178	13.0	1.37
E-glass	75	9.5	0.78	66	8.3	0.80
Basalt	117	11.1	1.05	117	11.1	1.05

5.4.4 Prediction of geocomposite elastic properties in in-plane shear

Unlike the previous case, for in-plane shear of unit cell the boundary conditions are described as: with two faces that are orthogonal to x-axis, one face is fixed in the y-direction while the other moves translationally in the y-direction; procedure is also similarly applied for two faces orthogonal to y-axis. Models are solved in a linear manner. Outputs from models are:

- $\sum RF_y$ is the total reaction force at the displaced edge. From this, the average stress in the x-direction in a unit cell is calculated

$$\tau_{ave} = \frac{\sum RF_y}{w_c t_c} \quad (5.54)$$

- The average strain in the x-direction in a unit cell are also calculated

$$\gamma_{ave} = \frac{2\delta w_c}{w_c} \quad (5.55)$$

where δw_c is the prescribed displacement

- The shear modulus is determined: $G = \frac{\tau_{ave}}{\gamma_{ave}}$ (5.56)
- The failure index is also calculated at each point for matrix and yarns by equation (5.53)

Figure 5.7 shows shear graphs of geocomposite reinforced carbon fabric from experiment and from simulation. We can realize that the behaviors of geocomposite from simulation of two geometrical models (skew-symmetrical and symmetrical two-layer stacks) are nearly similar with the same elastic modulus and equivalent to elastic modulus measured from experiment. However, if observing totally, these behaviors differ very much because the graph from experiment has nonlinear tendency.

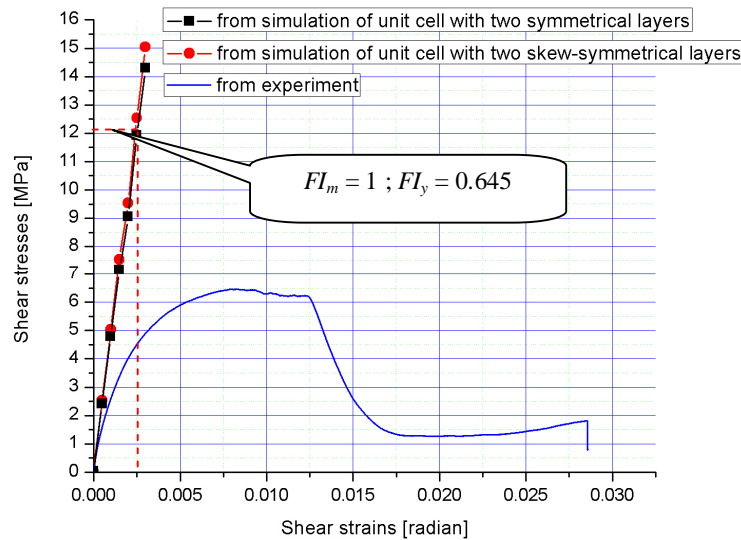


Fig. 5.7 Shear graphs of carbon geocomposites

Results from prediction of in-plane shear strength are too much higher than experiment as figure 5.7. Unlike the tension, when shear stress from simulation is greater than twice shear stress from experiment, the surrounding matrix layer is destroyed ($FI_m=1$) while load carrying capacity of the yarns is just over half ($FI_y=0.645$). This thing can be attributed that shear failure is due to adhesion between yarns and resin not imperfective like assumption. In other words, shear strength depends mainly on the adhesion between yarns and resin. Figure 5.8 shows spectra of distribution of Von-Mise stress on matrix and failure index value on yarns. We can see that for matrix the maximum stresses occur between yarns and between two layers. When observing two fabric layers, we can see also that shear load shares equally on them.

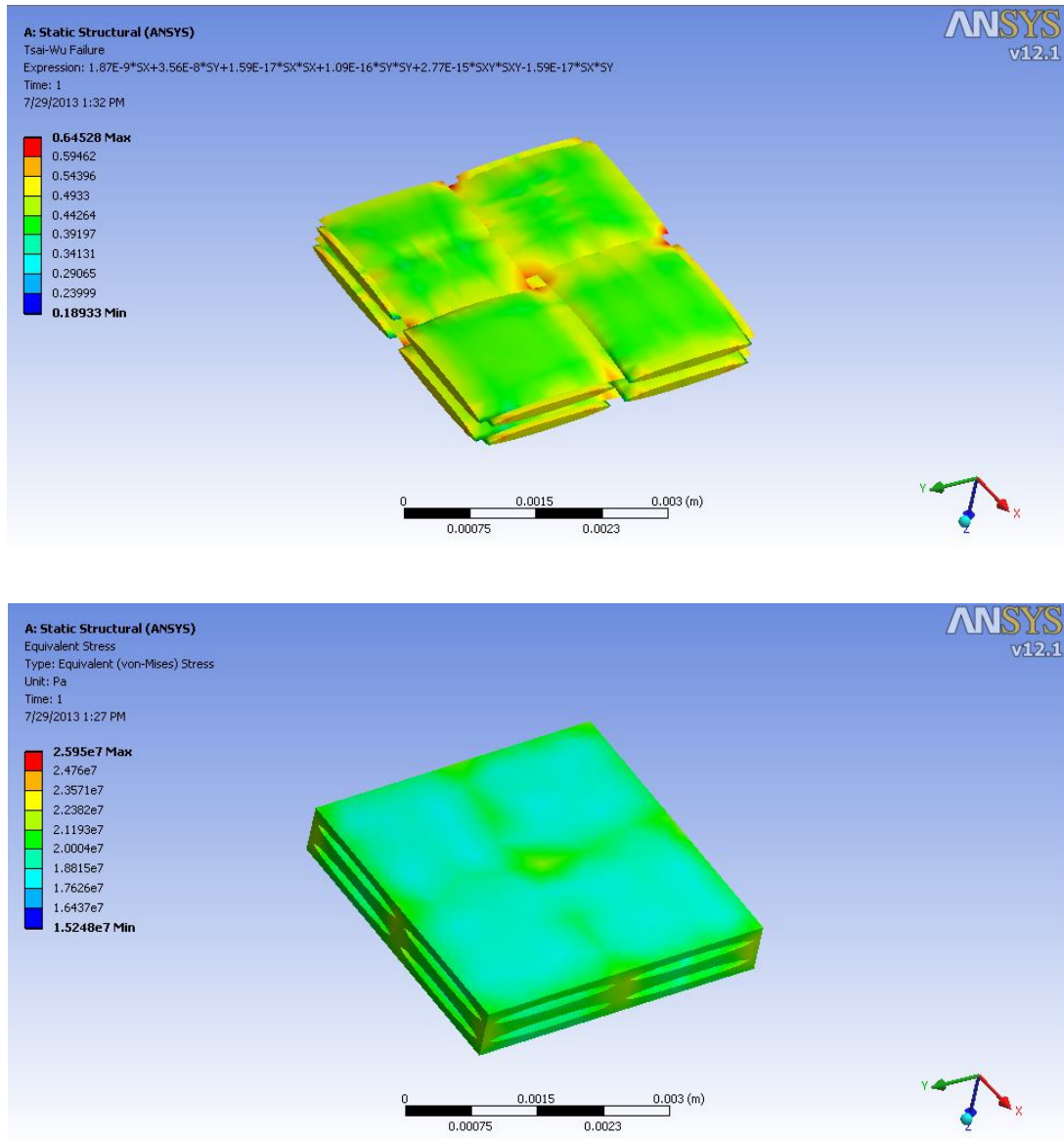


Fig. 5.8 The spectra of distribution of Von-Mise stress on matrix (below) and failure index value on yarns (above) in in-plane shear model.

5.4.5 Prediction of geocomposite interlaminar shear strength

For interlaminar shear of unit cell, the boundary conditions were described as follows. Z-direction displacements of two faces that are orthogonal to x-axis are fixed. One face oriented perpendicular to the z-axis is subjected by pressure p .

Assuming that the interlaminar shears occur between two layers within unit cell equal to values of failure stress obtained from experiments. From equation (3.26), we can derive a formula:

$$\tau_F = \frac{3}{4} \cdot \frac{pw_c^2}{w_c t_c} \quad \text{leads to} \quad p = \frac{4\tau_F t_c}{3w_c} \quad (5.57)$$

With carbon geocomposite $\tau_F = 1.75$ MPa (see Table 4.11), we get $p = 0.338$ MPa

Models are solved in a linear manner in Ansys. Outputs from models are Von-Mise stress in matrix and failure index value in yarns. The Tsai-Wu failure criterion applied for yarns in model of interlaminar shear strength prediction can be written as

$$FI_y = F_1\sigma_x + F_2\sigma_y + F_{11}\sigma_x^2 + F_{22}\sigma_y^2 + F_{55}\tau_{xz}^2 + F_{66}\tau_{xy}^2 + 2F_{12}\sigma_x\sigma_y \quad (5.58)$$

where coefficient $F_{55} = F_{66} = \frac{1}{\sigma_{LTu}^2}$

Figure 5.9 shows spectra of distribution of Von-Mise stress in matrix and failure index value in yarns. Observing pictures we can realize that the Von-Mise stress in matrix reaches the tensile strength of geopolymer, occurs at the middle zone of unit cell and the contact surface between matrix and yarns. This reason explains why delamination usually appears of composite materials. The color spectrum illustrating failure index scatter in yarns tells that the yarns seem not to be destroyed at all. It can prove that the results from simulation are agreement with tests.

5.4.5 Prediction of geocomposite thermo-mechanical behaviors

Thermal strains and stresses constitute an important part of the application of geocomposite for many practical engineering problems. They become especially critical because geopolymer and reinforcement with different coefficients of thermal expansion form interfaces. If neglecting thermal degradation of materials, we are able to analyze thermo-mechanical behavior of a geocomposite unit cell. A common cause of failure in composite materials is the thermal stresses at elevated temperatures caused by a coefficient of thermal expansion mismatch.

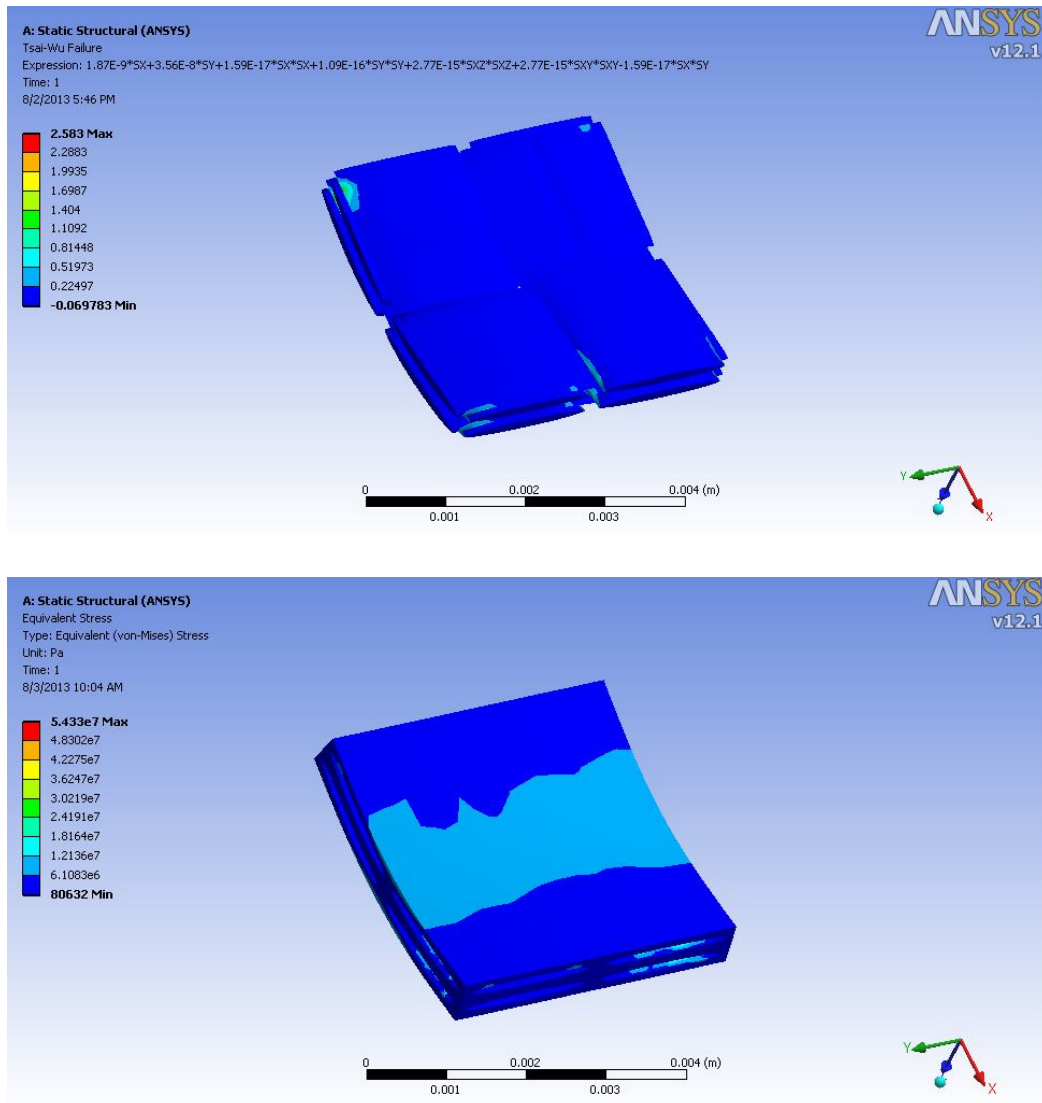


Fig. 5.9 The spectra of distribution of Von-Mise stress on matrix (below) and failure index value on yarns (above) in interlaminar shear model.

The goal of themomechanical analysis is to obtain displacement and stress fields. Then, we are able to calculate the effective CTE of unit cell as well as to evaluate strain and stress fields within unit cell.

Similar to above prediction, firstly, we need to determine thermal properties for components in a unit cell. Geopolymer matrix is considered as thermal isotropic material with

an average coefficient of thermal expansion (CTE) of approximately $15 \times 10^{-6} 1/^{\circ}\text{C}$ suggested by He et al. [64]. Four yarns in the unit cell are assumed as thermal orthotropic materials that have CTE dependent on the longitudinal and transverse directions of yarns. The equations calculating CTE are referred in equation (3.33), with $\alpha_T \approx \alpha_T$ and V_m is volume fraction of matrix occupied inside yarn volume. CTEs of carbon yarn, basalt yarn, E-glass yarn are referred in Table 5.4.

Continuously, thermomechanical model is analyzed linearly in Ansys environment at elevated temperatures 200°C , 400°C , 600°C , 800°C , and 1000°C . Outputs from models are:

- Δt_c^T , Δw_c^T are thermal expansion of thickness and width of a unit cell. From this, the average thermal strains of thickness and width of a unit cell can be calculated

$$\varepsilon_{tc}^T = \frac{\Delta t_c^T}{t_c} ; \varepsilon_{wc}^T = \frac{\Delta w_c^T}{w_c} \quad (5.59)$$

- The effective CTE of unit cell in through thickness and in-plane are also calculated

$$\alpha_{tc} = \frac{\varepsilon_{tc}^T}{\Delta T} ; \alpha_{wc} = \frac{\varepsilon_{wc}^T}{\Delta T} \quad (5.60)$$

where $\Delta T = T - T_o$, $T_o = 20^{\circ}\text{C}$

- The failure index is also calculated at each point for matrix and yarns by equation (5.53)

Figure 5.10 presents thermal strain graphs of geocomposite reinforced carbon fabric dependent on temperature levels after simulation of skew-symmetrical two-layer model. We can see that thermal deformation of plate thickness is higher than thermal deformation in plane of plate. On the other hand, through thickness coefficient of thermal expansion ($\alpha_{tc} = 14 \times 10^{-6} 1/^{\circ}\text{C}$) is higher than in-plane coefficient of thermal expansion ($\alpha_{wc} = 8.9 \times 10^{-6} 1/^{\circ}\text{C}$). However, if comparing with experiment, we can recognize that thermal model underestimates very low thickness expansion of sample. This problem can be explained that high temperature influenced on geopolymer matrix to generate many bubbles to make sample thickness expanded.

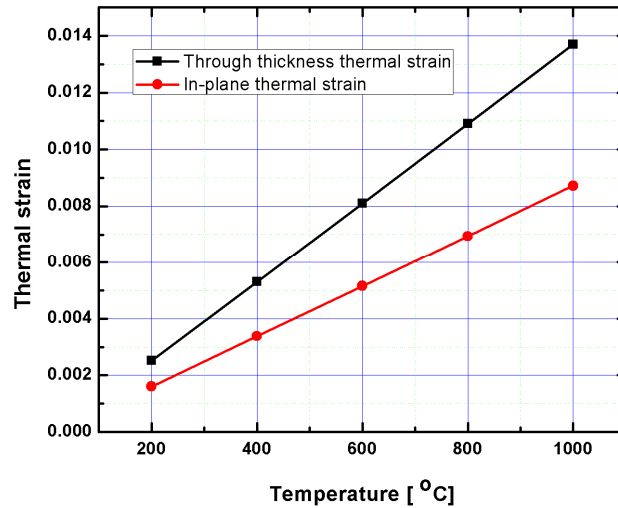


Fig. 5.10 Thermal strain graphs of geocomposite reinforced carbon fabric.

Figure 5.11 shows spectra of distribution of Von-Mise stress in matrix and failure index value in yarns at temperature of 200 °C. Observing pictures we can realize that the Von-Mise stress in matrix exceeds the tensile strength of geopolymer, occurs at the poor matrix zone in the unit cell and the interface between matrices and yarns where appears thermal expansion mismatch. The color spectrum illustrating failure index number scatter in yarns shows that the yarns bear maximum effective stress at the edges of yarns with value exceeds unit. Generally, when fabric reinforced geocomposites are heated in a high temperature condition the thermal stress always exist inside materials due to thermal expansion mismatch between matrix and yarns, the geometry of the fiber bundle and the surrounding matrix layers. Thermal stresses result in a lot of cracks existing in materials that degrade strength of geocomposite. This is inevitable for geocomposite materials.

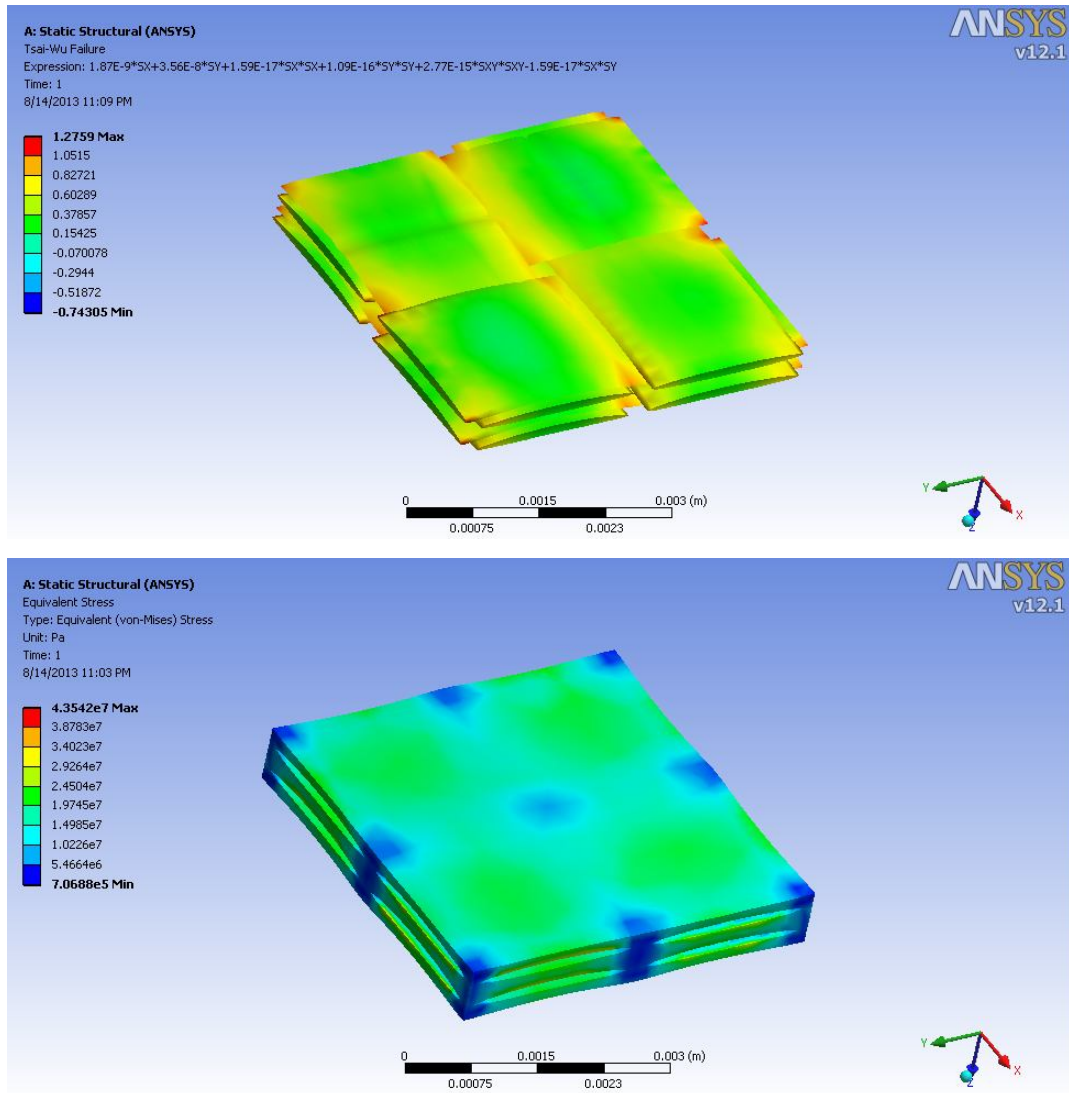


Fig. 5.11 The spectra of distribution of Von-Mise stress on matrix (below) and failure index value on yarns (above) in thermal model at 200 °C .

Chapter 6

POTENTIAL APPLICATIONS

With excellent properties such as fire resistant, light weight, being good to resist acid, high strength and no toxic, smoke while burning... fabric reinforced geocomposites are applicable in high technologies like airspace, automobile and military ship [1]. In individual ideas, author can recommend some applications of geopolymers as well as geocomposites reinforced with fabric fibers as follows.

- Insulation materials are used for hot piping industries.
- Insulation materials are used for chimneys, exhaust systems, heat equipments.
- Insulation materials is used for warning systems and insulator walls in building industries such as: cover bricks, cover Portland cements, cover polystyrene, cover plastics, cover woods, cover steels (Fig. 6.1, 6.2, 6.3).
- Materials are used for fabrication of mold systems, direct molten systems.
- Materials are used for fabrication of chemical insulations, for examples, tanks to contain acid solutions.
- It is possible to cut, to drill for geocomposites reinforced with fabric fibers (figure 6.5).
- Geopolymers can be used in radioactive waste stores because geopolymers are inorganic polymers suitable for encapsulating radioactive wastes so as to enable their safe and long-term storage.
- Geopolymers can be fabricated with different colors (figure 6.5).
- Geopolymers can be used for repairing in the ancient and modern architecture (figure 6.6).

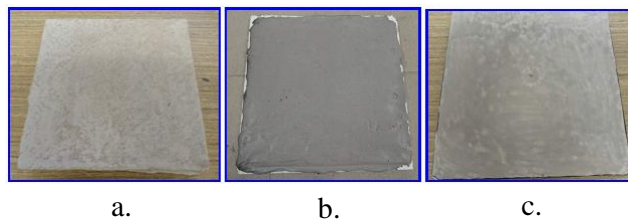


Fig. 6.1 a. Polystyrene coated by pure geopolymer;
 b. Polystyrene coated by geopolymer mortar;
 c. Plastic coated by pure geopolymer.



Fig. 6.2 Portland concrete coated by pure geopolymer before (left) and after heated 600 °C (right)

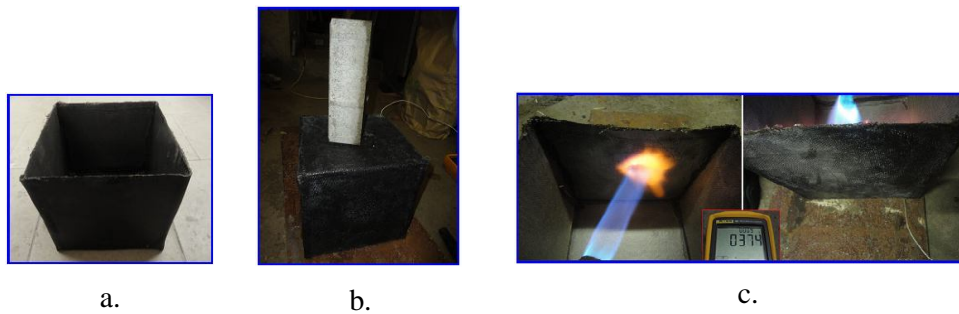


Fig. 6.3 a. Geopolymer composite reinforced basalt fabric fiber, box (200 x 200 x 200) mm;
b. Heating 300 °C and loading 1.5 kg; c. The box heated by flame up to 374 °C



Fig. 6.4 Wooden plate coated by geopolymer mortar (left) and after heated 354 °C in the oven, outside only 175.8 °C



Fig. 6.5 a. Geocomposite samples after cutting and drilling; b. Geopolymer mortar with different colors

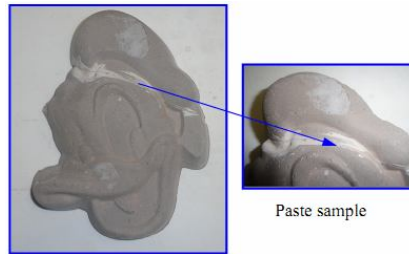


Fig. 6.6 The broken architecture sample was pasted by geopolymers

Chapter 7

CONCLUSIONS AND FUTURE WORKS

In this dissertation, geocomposites reinforced fabrics can be fabricated by the hand lay-up technique combined with bagging technique (using the "molding by vacuum") for 1 hour at room temperature and for 2 hours in an oven at 80 °C with a pressure of 0.3 MPa. And finally, materials were dried for 20 hours at the same curing condition after removed off from the bag. The thermo-mechanical behavior of the composite combined geopolymer and carbon, basalt, and E-glass woven fabrics has been studied. The elastic characteristics of the geocomposites were tested and simulated in normal condition and in high temperature. Some standard experiments such as simple tensile, pure shear, flexural and thermal conductivity tests for of pure geopolymers, fabrics as well as of geocomposites were carried out. Especially, experiments verifying fire-resistant properties of geocomposite materials were conducted thoroughly with a goal to confirm these advantage performances. The prediction of elastic properties of geocomposites was implemented with various models of a unit cell in materials aiming to quantify the geometric parameters of fiber bundles and to evaluate their effects on mechanical properties. The combination between free software named TexGen and finite element program, Ansys, was established for modeling thermo-mechanical behavior of unit cell in 3D geometry of textile composite. Some results from simulation agreed well with from test but some results were underestimated due to complexion of non-homogeneity of geocomposite materials.

Generally, the results show that the mechanical properties of geocomposites depend on types of fabric both from experiments and from simulations. Combinations of geopolymer and carbon fibers or E-glass fibers are tougher than of geopolymer and basalt fibers. In the opposite direction, geocomposite with basalt fibers is harder and more brittle than with carbon and E-glass fibers. In a normal condition or in high temperatures the carbon geocomposite has tension, in-plane shear, interlaminar shear strengths better than the other two geocomposites. In assess of thermal stability and fire-resistant performance, the residual strength of all geocomposites decreases after heating at different levels of 200 °C, 400 °C, 600 °C, 800 °C, and 1000 °C for 30 minutes. At level of 400 °C, geocomposite 10C remains 36% of original ultimate strength; hybrid geocomposites 5E+2x1C, 5E+2x2B, 12B+2x1C kept

29%, 37%, 27% of strengths in room temperature while for geocomposites 7E and 15B are only 12% and 10%. Especially, the remaining strength of composites 10C increases when the temperature is above 600 °C and has good toughness of approximate 79% after heating at 1000 °C. Thickness thermal expansion of carbon geocomposite is very stable with maximum increase of 28% compared to the original thickness. In a contrary, basalt geocomposite and E-glass geocomposite seem to stabilize worse in elevated temperature due to porosity observed by microscopy system. Thermal tests also proved that thermal conductivity coefficients of geocomposite are very low (for E-glass geocomposite: 0.46 W/mK; for carbon geocomposite: 0.66 W/mK; for basalt geocomposite: 0.56 W/mK) to be useful in fabrication of thermal insulation materials. Furthermore, with excellent properties, for instance: ease of manufacturing, light weight (lower 2 g/cm³), no toxic and smoke while burning, being possible to cut and to drill, good bonding with steels, woods, bricks, cements, polystyrene, plastics... geocomposites or geopolymers have wide potential application for many industrial fields.

In order to fully evaluate realistic possibility of geocomposite reinforced fabric in high temperature, it should be implemented simple tensile, pure shear, flexural experiments with testing machine equipped heat chamber similar to ovens. This will help us understand clearly thermo-mechanical behavior of geocomposites at instant time on heating.

Literatures

- [1] Davidovits J., Geopolymers: *Inorganic polymeric new materials*, Journal of Thermal Analysis, Vol. 37, p. 1633 – 1656, 1991
- [2] Davidovits J., *Geopolymer Chemistry & Applications*, Institut Géopolymère, France (2008).
- [3] Davidovits J., *30 Years of Successes and Failures in Geopolymer Applications - Market trends and Potential breakthroughs*, Geopolymer 2002 Conference, Melbourne, Australia (2002).
- [4] Davidovits J., Geopolymer, *Green Chemistry and Sustainable Development Solutions*, Proceedings of the World Congress Geopolymer (2005), p. 9-16.
- [5] Sheppard L.M., *Geopolymer composites: A ceramics Alternative to Polymer Matrices, the 105th Annual Meeting and Exposition of the American Ceramic Society*-[http://composite.about.com/library/weekly/aa030529.htm\(2007\).](http://composite.about.com/library/weekly/aa030529.htm(2007).)
- [6] Kriven W.M., Gordon, M. and Bell, J.L., *Geopolymers: Nanoparticulate, Nanoporous Ceramics Made Under Ambient Conditions, Microscopy and Microanalysis '04, (Proc. 62nd Annual Meeting of Microscopy Society of America)* vol. 10 (2004), p. 404-405.
- [7] Papakonstantinou C.G. and Balaguru P.N., *Use of geopolymer matrix for high temperature resistant hybrid laminates and sandwich panels*, *Geopolymer, Green Chemistry and Sustainable Development Solutions*, Proceedings of the World Congress Geopolymer (2005), p. 201-208.
- [8] Palomo et al., *Alkali activated fly ashes: A cement for the future* *Cement Concrete Res* 29, p. 1323 – 1329, 1999.
- [9] Rangan R.V., *Low-calcium fly ash based geopolymer concrete*, *Concrete construction Engineering handbook* (2nd ed.), New York, 2007.
- [10] Mallick P.K., *Department of Mechanical Engineering, University of Michigan-Dearborn, Dearborn, Michigan: Fiber-reinforced composites Materials, Manufacturing, and Design.*

- [11] Duxson P., et al, *Thermal conductivity of metakaolin geopolymers used as a first approximation for determining gel interconnectivity*, Ind. Eng. Chem. Res. 45 (23), p. 7781 – 7788, 2006.
- [12] Fareed Ahmed M., *Compressive Strength and Workability Characteristics of Low-Calcium Fly ash-based Self-Compacting Geopolymer Concrete*, Word Academy of Science, Engineering and Technology 74, 2011.
- [13] Duxson P., et al., *Geopolymer technology: the current state of the art*. Journal Material Science. 42: p. 2917-2933, 2007.
- [14] Davidovits J. *About geopolymerization*. [cited 2011 October 22]; Available from: <http://www.geopolymer.org/science/about-geopolymerization>.
- [15] Zongjin Li, et al., *Advanced Concrete Technology*: John Wiley & Sons, Canada, 2011.
- [16] Mustafa A. B. A. M., *Mechanism and Chemical Reaction of Fly Ash Geopolymer Cement- A Review Journal of Asian Scientific Research. 1*: p. 247-253, 2011.
- [17] Panagiotopoulou Ch., et al., *Dissolution of aluminosilicate minerals and by-products in alkaline media*. Materials Science. 42: p. 2967–2973, 2007.
- [18] McCormick A. V., et al., *Evidence from alkali-metal NMR spectroscopy for ion pairing in alkaline silicate solutions*. Physical Chemistry 93: p. 1737-1742, 1989.
- [19] Davidovits J., *Geopolymer chemistry & application*, ed. Second. 2008: Institute Géopolymère – France. 587.
- [20] Duxson P., et al., *The role of inorganic polymer technology in the development of ‘green concrete*. Cement and Concrete Research. 37: p. 1590 – 1597, 2007.
- [21] Dimas D., et al., *Polymerization in sodium silicate solutions: a fundamental process in geopolymerization technology*. Materials Science. 44: p. 3719–373, 2009.
- [22] Panyas D., et al., *Effect of synthesis parameters on the mechanical properties of fly ash-based geopolymers*. Colloids and Surfaces A: Physicochemical and Engineering Aspects. 301: p. 246-254, 2007.
- [23] Phair J. W., *Effect of the silicate activator pH on the microstructural characteristics of waste-based geopolymers*. International Journal of Mineral Processing. 66: p. 121-143, 2002.

- [24] Duxson P., et al., *Effect of Alkali Cations on Aluminum Incorporation in Geopolymeric Gels*. Industrial & Engineering Chemistry Research, 2005. 44(4): p. 832-839.
- [25] Duxson P., et al., *Understanding the relationship between geopolymer composition, microstructure and mechanical properties*. Colloids and Surfaces A: Physicochemical and Engineering Aspects, 2005b. 269(1-3): p. 47-58.
- [26] Kriven W.M. and J.L. Bell, *Effect of Alkali Choice on Geopolymer Properties*. Ceramic Engineering and Science Proceedings, 2004: p. 99-104.
- [27] Singh P.S., T. Bastow, and M. Trigg, *Outstanding problems posed by nonpolymeric particulates in the synthesis of a well-structured geopolymeric material*. Cement and Concrete Research, 2004. 34(10): p. 1943-1947.
- [28] Sindhunata et al., *Effect of Curing Temperature and Silicate Concentration on Fly-Ash-Based Geopolymerization*. Industrial & Engineering Chemistry Research, 2006. 45(10): p. 3559-3568.
- [29] Wang H., H. Li, and F. Yan, *Synthesis and mechanical properties of metakaolinite-based geopolymer*. Colloids and Surfaces A: Physicochemical and Engineering Aspects, 2005. 268(1-3): p. 1-6.
- [30] Weng L., et al., *Effects of aluminates on the formation of geopolymers*. Materials Science and Engineering B, 2005. 117(2): p. 163-168.
- [31] Duxson P., et al., *The effect of alkali and Si/Al ratio on the development of mechanical properties of metakaolin-based geopolymers*. Colloids and Surfaces A: Physicochemical and Engineering Aspects, 2007. 292(1): p. 8-20.
- [32] Mehta P.K. High-Performance, *High-Volume Fly Ash Concrete for Sustainable Development*. in International Workshop on Sustainable Development and Concrete Technology. 2004. Beijing, China.
- [33] Nugteren H.W., V.C.L. Butselaar-orthlieb, and M. Izquierdo, *High Strength Geopolymers Produced from Coal Combustion Fly Ash*. Global NEST Journal, 2009. 11(2): p. 155-161.
- [34] Bortnovsky O., et al. *Structure and stability of geopolymers synthesized from kaolinitic and shale clay residues*. in *Geopolymer, green chemistry and sustainable development solutions*, The World Congress Geopolymer 2005, Sain-Quentin. 2005. Sain-Quentin, France: Geopolymer Institute.

- [35] Miller N.A., C.D. Stirling, and C.I. Nicholson. *The relationship between cure conditions and flexural properties in flyash-based geopolymers. in Geopolymer, green chemistry and sustainable development solutions*, the World Congress Geopolymer 2005. 2005. Sain-Quentin, France.
- [36] Varela, B., *A Study on the Suitability of Geopolymers for Structural Steel Fire Prevention*. Las Cruces, New Mexico: New Mexico State University, 2002.
- [37] Foden A.J., Balaguru P., and Lyon R.E., *Fire Response of Geopolymer Structural Composites*, In Proceedings from the First International Conference on Fiber Composites in Infrastructure, 1996, pp.972-981.
- [38] Davidovits, J., *Global Warming Impact on the Cement and Aggregates Industries*, World Resource Review Vol.6 No.2, 1994, pp. 263-278.
- [39] Mishra S.R., Kuman S., A.Park, J.Rho, J.Losby, B.K. Horrmeister, *Ultrasonic Characterization of the Curing Process of PCC Fly Ash-Cement Composites Materials Characterization*, vol. 50, no. 4-5, pp. 317-323, 2003.
- [40] Pinto A.T., Viera E., *Optimised Conditions for the Obtaining of Metakaolin*, Materials Science Forums, vol. 514-516, pp. 1536-1540, 2006.
- [41] Van Jaarsveld J.G.S., Van Deventer J.S.J., Lorenzen L., *The Potential Use of Geopolymeric Materials to Immobilise Toxic Metals: Part I. Theory and Applications*, Minerals Engineering vol.10, no.7, pp. 659-669, 1996.
- [42] Davidovits J. and M. Davidovics, *Geopolymer: Ultra-High temperature Tooling Material for the Manufacture of Advanced composites*. 36th SAMPE Symposium, 1991. 36(2): p. 1939-1949.
- [43] Hussain M., et al., *Investigation of thermal and fire performance of novel hybrid geopolymer composites*. Journal of Materials Science, 2004. 39(14): p. 4721-4726.
- [44] Bogdanovich A.E. and Pastore C.M., *Mechanics of Textile and Laminated Composites: With applications to structural analysis*, Chapman & Hall: p.235-236; p.250-261.
- [45] Dubrovski P.D., *Woven Fabric Engineering*, Sciyo: p.1-9.
- [46] Robert M.J., *Mechanics of Composite Materials*, Second Edition, Taylor & Francis, 2006.
- [47] Autar K.Kaw, *Mechanics of Composite Materials*, Second Edition, Taylor & Francis, 2006.

- [48] Creemers R.J.C, *Interlaminar shear strength criteria for composites: An assessment by means of statistical analysis*, 2010. NLR.
- [49] Mallick P.K., *Fiber Reinforced Composites: Materials, Manufacturing, and Design*, Taylor & Francis, 2007.
- [50] Hung, T.D., et al., *Effect of curing condition on mechanical properties of fibers and composites based on geopolymer matrices*, in The 2nd International Student Conference of Material Science, Liberec - Czech Republic, 2008.
- [51] Hung, T.D., et al., *Thermal-Mechanical behavior of silica-based geopolymer-carbon composite*, in The 7th International Conference – TEXSCI 2010, September 6-8, Czech Republic.
- [52] EN ISO 13934, *Standard test method for tensile properties of textile*
- [53] ASTM C 1275 – 00, *Standard test method for tensile properties of continuous fiber-reinforced advanced ceramic composites*. 2006, ASTM.
- [54] Arcan. M, et al., *A method to produce uniform plane-stress states with applications to fiber-reinforced materials*, April 1978, Experimental Mechanics. p. 141-146.
- [55] Holzapfel G.A. , *Nonlinear solid mechanics*, John Wiley & Sons Ltd, Chichester West Sussex PO19, England, 2000.
- [56] ASTM D2344, *Standard test method for short-beam shear test*. 2006, ASTM.
- [57] Sideridis E., et al., *Short-Beam and Three-Point-Bending Tests for the Study of Shear and Flexural Properties in Unidirectional-Fiber-Reinforced Epoxy Composites*, (www.interscience.wiley.com).
- [58] Davidovits J., *Geopolymer - fiber composites*, in *Geopolymer Chemistry & Applications*, D. Joseph, Editor. 2008, Geopolymer Institute: Saint-Quentin, France.
- [59] Lyon R.E., et al. *Fire response of geopolymer structural composites*. in The First International Conference on Composites in Infrastructure (ICCI' 96). 1996. Tuscon, Arizona, United States.
- [60] ASTM C 1341 - 06, *Standard test method for flexural properties of continuous fiber-reinforced advanced ceramic composites*. 2006, ASTM.
- [61] Thermal Diffusivity – Thermal Conductivity: Method, Technique, Applications of Flash Apparatus LFA 447 NanoFlash
- [62] Stepan V.Lomov, *Predictive models for textile composites*, in The 7th International Conference – TEXSCI 2010, September 6-8, Czech Republic.

- [63] Martin Sherburn, *Geometric and Mechanical Modelling of Textiles*, Thesis submitted to The University of Nottingham for the degree of Doctor of Philosophy, 2007.
- [64] Mills-Brown J., *Thermal and tensile properties of polysialate composites*, Journal of ScienceDirect, 2013.
- [65] Jonathan Jcrookston, *Prediction of elastic behaviour and initial failure of textile composite*, PhD Dissertation, University of Nottingham, 2004.
- [66] http://texgen.sourceforge.net/index.php/User_Guide
- [67] Kent L.Lawrence, *ANSYS Workbench Tutorial*, University of Texas at Arlington, 2010.

PUBLICATIONS OF AUTHOR

1. **Nhan P.T** “*Estimate the elastic modulus and strength of composites with Basalt woven fiber reinforcement and thermal silica geopolymer matrix by ANSYS software*”. Conference of Mechanics of Composite Materials and Constructs – in April of 2011 at ČVUT in Prague, Czech Republic
2. Petrikova I., Marvalova B., **Nhan P.T.**, “*Influence of thermal ageing on mechanical properties of styrene-butadiene rubber*”, In Constitutive models for rubber VII, Jerams & Mutrphy eds, pp. 77-83, Taylor & Francis, London 2012, ISBN 978-0-415-68389-0
3. **Nhan P.T** “*Tensile mechanical properties of woven fabric geocomposites*”. The International Conference on Materials Science and Technology – in Jun of 2012 at NTU in NhaTrang, Vietnam
4. **Nhan P.T** “*Fire-resistant properties of woven fabric geocomposites*”. Conference of Young Scientists – in May of 2012 at University of Economy in Wroclawiu, Poland, pp. 104, ISBN 978-83-62708-66-6
5. **Nhan P.T** “*Prediction of elastic tensile behaviors and initial failure of geocomposites reinforced woven fabrics in 3D-simulation by TexGen and Ansys softwares*”. Workshop for PhD of Textile Faculty and Mechanical Faculty – in September of 2012 at Svetlanka, Czech Republic, pp. 238, ISBN 978-80-7372-891-5
6. Kafka J. , **Nhan P.T** “*Simulation of the behaviors of knitted structure made of Ni-Ti wires to the mechanical loading*”. Computation of constructs by FEM – in December of 2011 at ZČU in Plzen, Czech Republic, pp. 33, ISBN 978-80-261-0059-1
7. **Nhan P.T** “*In-plane shear properties of geocomposites reinforced woven fabrics*”, Mezinárodní vědecká konference k problematice technologických a inovačních procesů Technnológia Europea 2012, ISBN 978-80-905243-4-7, http://www.vedeckekonference.cz/library/proceedings/te_2012.pdf
8. Thai H.L.H, **Nhan P.T** “*Analysis stability of brake related to squeal by finite element method*”, Grant Journal, ISSN 1805-062X, 1805-0638 (online), <http://www.grantjournal.com/images/stories/0101thai.pdf>

APPENDIX A



Fig. A.1 Geocomposite samples: 7E, 10C, 15B, 5E+2x2B, 5E+2x1C, 12B+2x1C after heating at different level 200 °C, 400 °C, 600 °C, 800 °C, and 1000 °C for 30 mins.

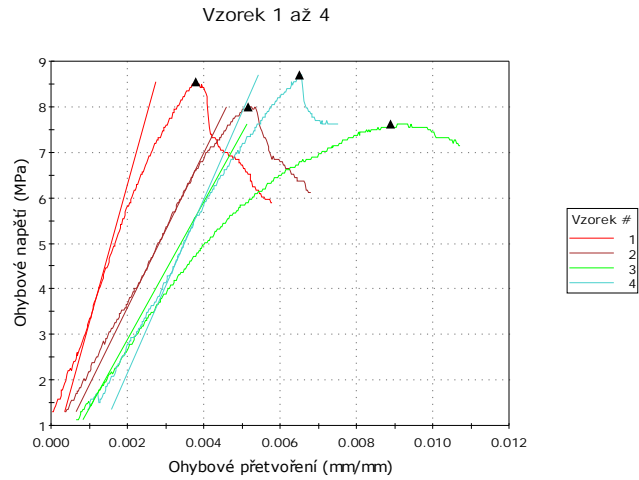


Fig. A.2 Flexural graph of geocomposite 7E after heating at 600 °C for 30 mins

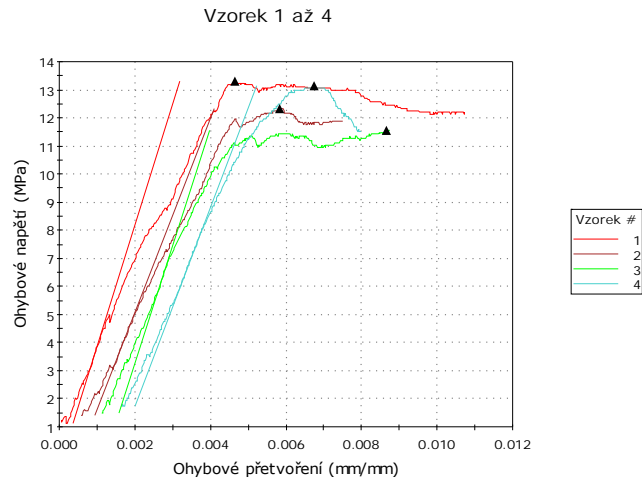


Fig. A.3 Flexural graph of geocomposite 7E+2x1C after heating at 600 °C for 30 mins

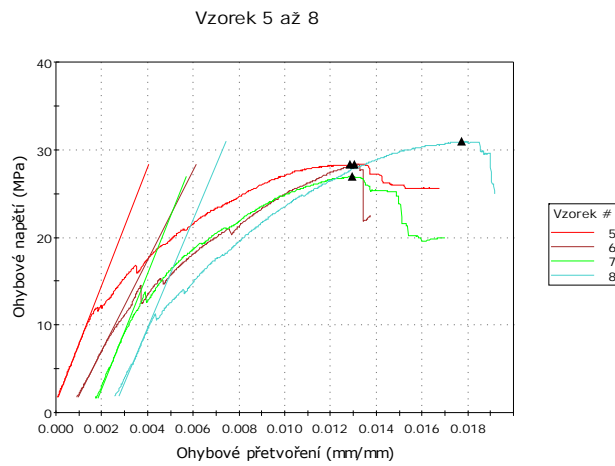


Fig. A.4 Flexural graph of geocomposite 7E+2x2B after heating at 600 °C for 30 mins

Vzorek 1 až 4

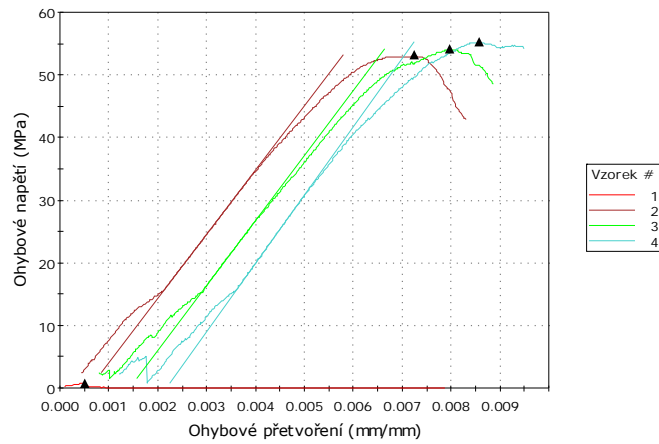


Fig. A.5 Flexural graph of geocomposite 10C after heating at 1000 °C for 30 mins

Vzorek 1 až 4

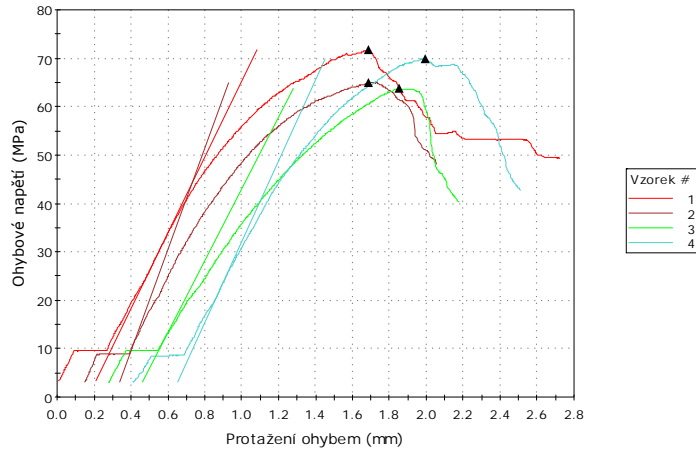


Fig. A.6 Flexural graph of geocomposite 15B at room temperature

Vzorek 1 až 8

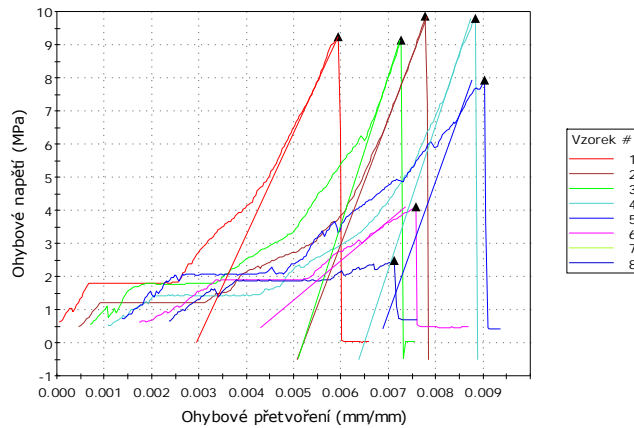


Fig. A.7 Flexural graph of geocomposite 12B+2x1C after heating at 200 °C for 30 mins

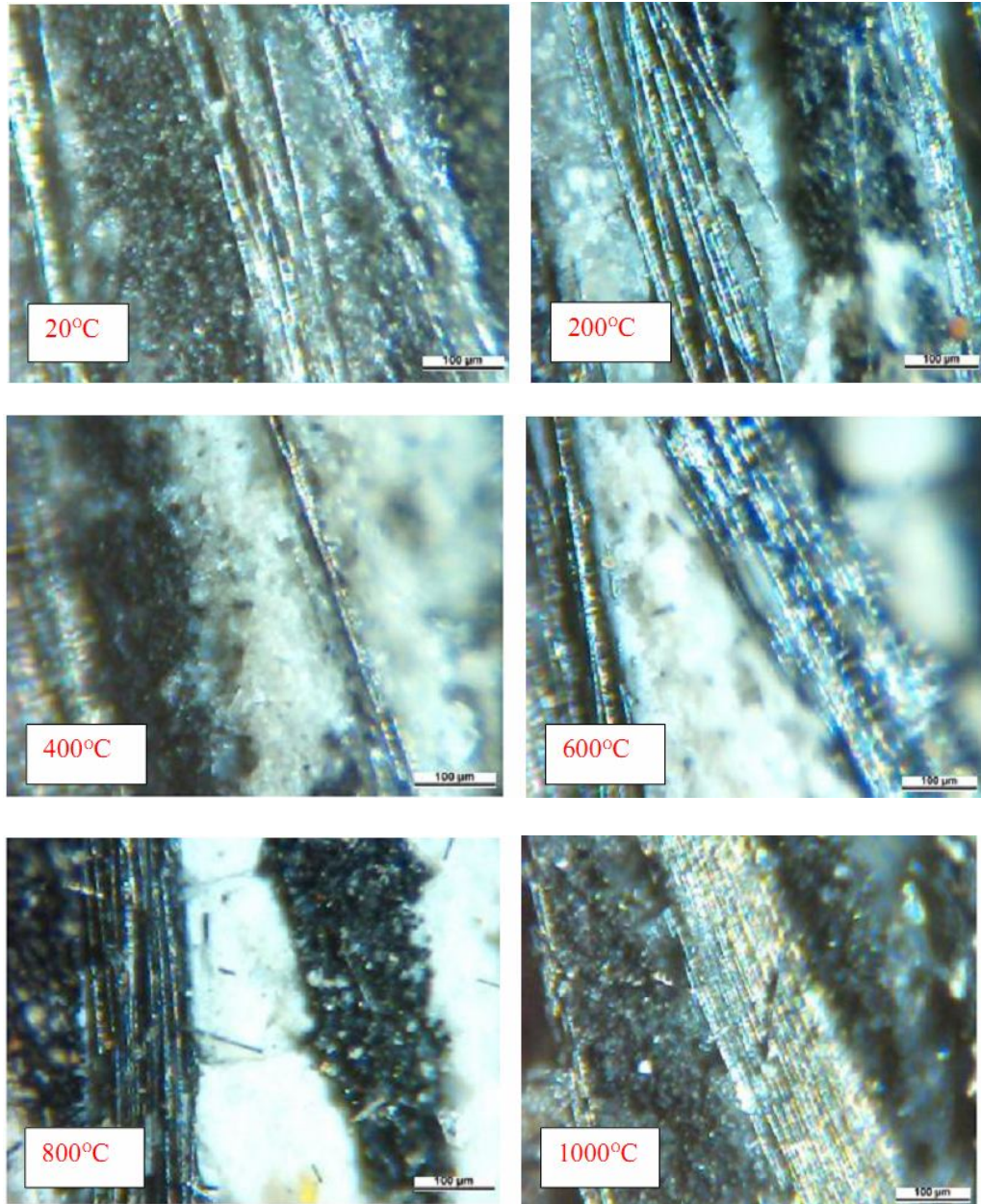


Fig. A.8 Observation of the microstructure of the geocomposite 10C in room temperature and after heating at different level 200 °C, 400 °C, 600 °C, 800 °C, and 1000 °C for 30 mins.

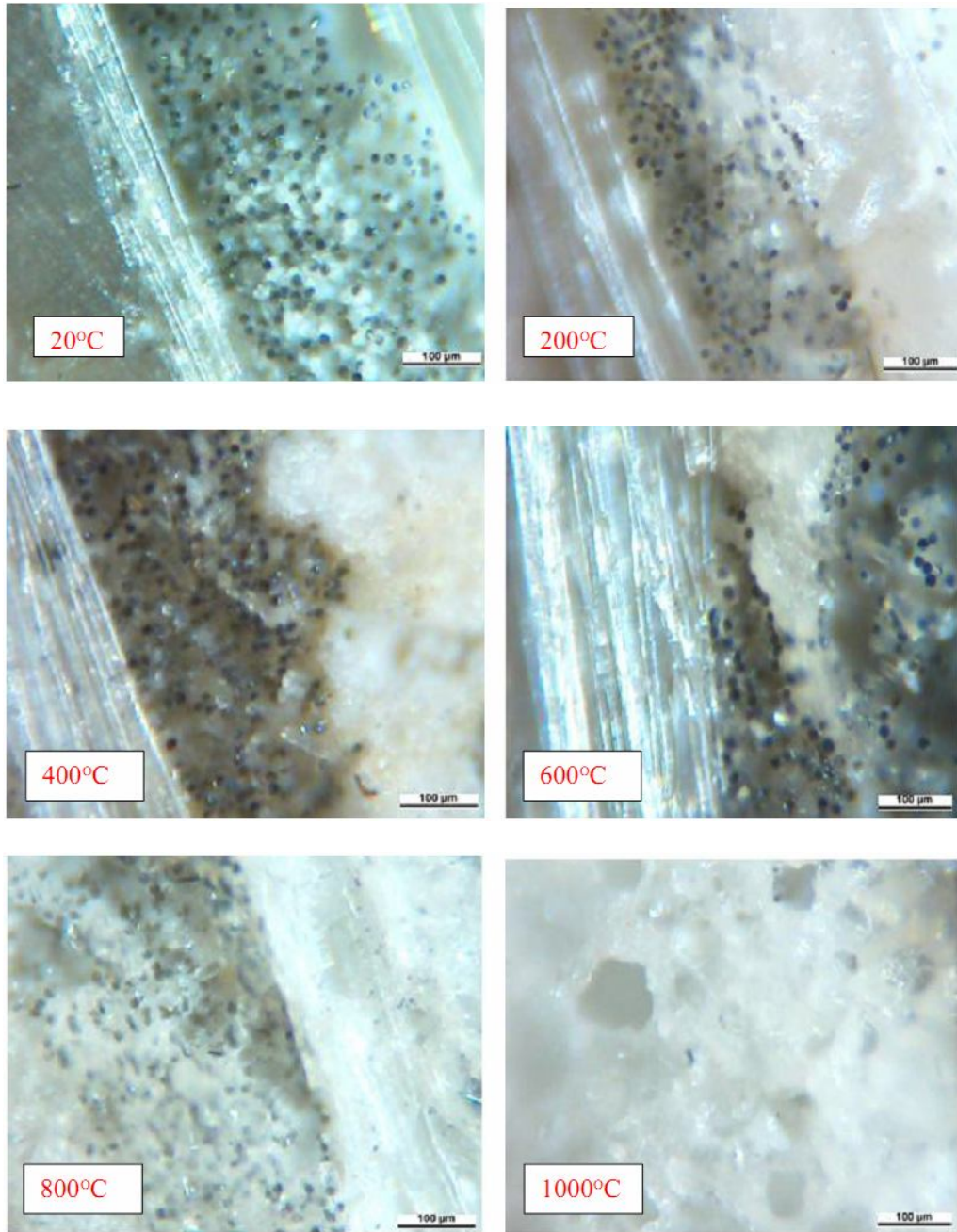


Fig. A.9 Observation of the microstructure of the geocomposite 7E in room temperature and after heating at different level 200 °C, 400 °C, 600 °C, 800 °C, and 1000 °C for 30 mins.

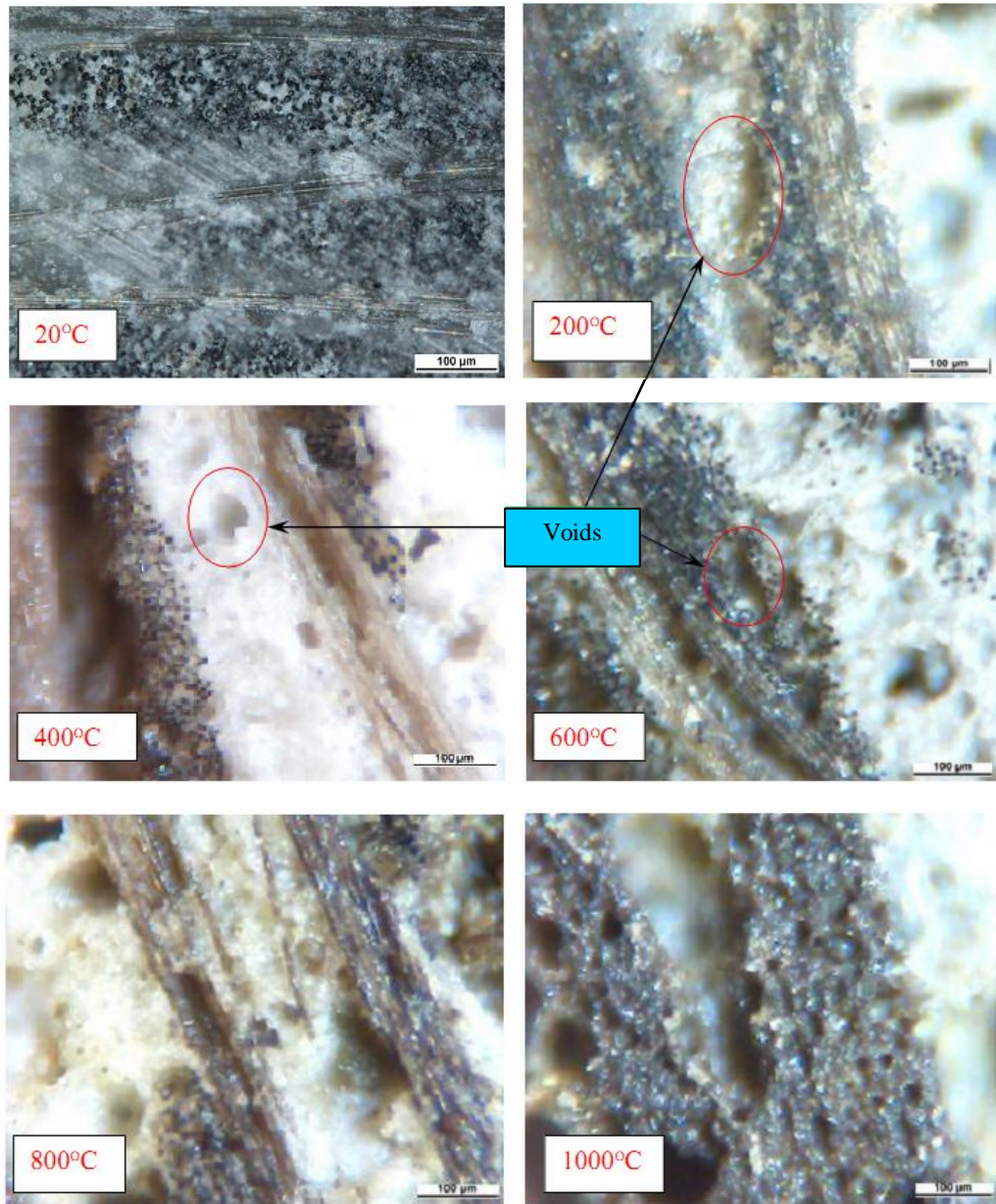


Fig. A.10 Observation of the microstructure of the geocomposite 15B in room temperature and after heating at different level 200 °C, 400 °C, 600 °C, 800 °C, and 1000 °C for 30 mins.

APPENDIX B

SOME M-FUNCTION AND SCRIPT FILES IN MATLAB

B.1. The Script file calculates shear strains from digital data of Istra camera.

```

clear
p=140:175;
q=180:205;
cti_e1=['/strains/strain_p1'];
cti_e2=['/strains/strain_p2'];
cti_u=['/displacements/displacement_x'];
cti_v=['/displacements/displacement_y'];
cti_x=['/coordinates/coordinate_x'];
cti_y=['/coordinates/coordinate_y'];
cti_mask=['/coordinates/mask'];
I=[1 0;0 1];
snimek=0;
nazev=['series_step_', int2str(snimek),'.hdf5'];
X= hdf5read(nazev,cti_x);
Y= hdf5read(nazev,cti_y);
mask = double(hdf5read(nazev, cti_mask));
X=X(p,q);
Y=Y(p,q);
n=length(p)*length(q);
sX=reshape(X,n,1);
sY=reshape(Y,n,1);
jedna=ones(n,1);
nula=zeros(n,1);
MAT=[sX,sY,jedna];
R=triu(qr(MAT));
vysled=[];
for snimek=1:179
    nazev=['series_step_', int2str(snimek),'.hdf5'];
    x= hdf5read(nazev,cti_x);
    y= hdf5read(nazev,cti_y);
    x=x(p,q);
    y=y(p,q);
    u= hdf5read(nazev,cti_u);
    v= hdf5read(nazev,cti_v);
    u=u(p,q);
    v=v(p,q);
    prav=reshape(u,n,1);
    res=R\'(R\'(MAT'*prav));
    epsxy=res(2);
    prav=reshape(x,n,1);
    res=R\'(R\'(MAT'*prav));
    f(1,1)=res(1);
    f(1,2)=res(2);
    prav=reshape(v,n,1);
    res=R\'(R\'(MAT'*prav));
    epsxy=epsxy+res(1);
    prav=reshape(y,n,1);
    res=R\'(R\'(MAT'*prav));
    f(2,1)=res(1);
    f(2,2)=res(2);
    E=(f'*f-I)/2;
    vysled=[vysled; epsxy E(1,2)];
end

```

B.2. “Crimpmodelisostrain” function

```

function [Ex,Ey,nuyxy,Gxy]=crimpmodelisostrain(EL_warp,EL_weft,ET,nuyLT,GLT,nuyTT,GTT,phi_warp,
phi_weft,k_warp,k_weft,km)
Em = 11.7;
nuy_m = 0.05;
Gm = Em/(2*(1+nuy_m));
Cg_m = inv([1/Em -nuy_m/Em -nuy_m/Em 0 0 0;-nuy_m/Em 1/Em -nuy_m/Em 0 0 0;-nuy_m/Em -nuy_m/Em
1/Em 0 0 0;0 0 0 1/Gm 0 0;0 0 0 0 1/Gm 0;0 0 0 0 0 1/Gm]);

Cl_warp = inv([1/EL_warp -nuyLT/EL_warp -nuyLT/EL_warp 0 0 0;-nuyLT/EL_warp 1/ET -nuy_m/ET 0 0
0;-nuyLT/EL_warp -nuy_m/ET 1/ET 0 0 0;0 0 0 1/GTT 0 0;0 0 0 0 1/GLT 0;0 0 0 0 0 1/GLT]);
Cg_warp = [0 0 0 0 0 0;0 0 0 0 0 0;0 0 0 0 0 0;0 0 0 0 0 0;0 0 0 0 0 0;0 0 0 0 0 0];
for i = 1:10
    anpha_warp = ((phi_warp/20)*3.14/180)*(-2*i+11);

    T_epsilon_warp = [0 (cos(anpha_warp))^2 (sin(anpha_warp))^2
sin(anpha_warp)*cos(anpha_warp) 0 0;1 0 0 0 0 0;0 (sin(anpha_warp))^2 (cos(anpha_warp))^2
-sin(anpha_warp)*cos(anpha_warp) 0 0;0 0 0 0 cos(anpha_warp) -sin(anpha_warp);
0 -2*sin(anpha_warp)*cos(anpha_warp) 2*sin(anpha_warp)*cos(anpha_warp)
(cos(anpha_warp))^2-(sin(anpha_warp))^2 0 0;0 0 0 0 sin(anpha_warp) cos(anpha_warp)];

    T_sigma_warp = [0 (cos(anpha_warp))^2 (sin(anpha_warp))^2
2*sin(anpha_warp)*cos(anpha_warp) 0 0;1 0 0 0 0 0;0 (sin(anpha_warp))^2
(cos(anpha_warp))^2 -2*sin(anpha_warp)*cos(anpha_warp) 0 0;0 0 0 0 cos(anpha_warp)
-sin(anpha_warp);0 -sin(anpha_warp)*cos(anpha_warp) sin(anpha_warp)*cos(anpha_warp)
(cos(anpha_warp))^2-(sin(anpha_warp))^2 0 0;0 0 0 0 sin(anpha_warp) cos(anpha_warp)];

    delta_Cg_warp = k_warp*T_sigma_warp*Cl_warp*inv(T_epsilon_warp);
    Cg_warp = Cg_warp+delta_Cg_warp;
end

Cl_weft = inv([1/EL_weft -nuyLT/EL_weft -nuyLT/EL_weft 0 0 0;-nuyLT/EL_weft 1/ET -nuy_m/ET 0 0
0;-nuyLT/EL_weft -nuy_m/ET 1/ET 0 0 0;0 0 0 1/GTT 0 0;0 0 0 0 1/GLT 0;0 0 0 0 0 1/GLT]);
Cg_weft = [0 0 0 0 0 0;0 0 0 0 0 0;0 0 0 0 0 0;0 0 0 0 0 0;0 0 0 0 0 0;0 0 0 0 0 0];
for i = 1:10
    anpha_weft = ((phi_weft/20)*3.14/180)*(-2*i+11);

    T_epsilon_weft = [(cos(anpha_weft))^2 0 (sin(anpha_weft))^2
0 sin(anpha_weft)*cos(anpha_weft) 0;0 1 0 0 0 0;(sin(anpha_weft))^2 0 (cos(anpha_weft))^2
0 -sin(anpha_weft)*cos(anpha_weft) 0;0 0 0 0 cos(anpha_weft) 0 -sin(anpha_weft);
-2*sin(anpha_weft)*cos(anpha_weft) 0 2*sin(anpha_weft)*cos(anpha_weft)
0 (cos(anpha_weft))^2-(sin(anpha_weft))^2 0;0 0 0 0 sin(anpha_weft) 0 cos(anpha_weft)];

    T_sigma_weft = [(cos(anpha_weft))^2 0 (sin(anpha_weft))^2
0 2*sin(anpha_weft)*cos(anpha_weft) 0;0 1 0 0 0 0;(sin(anpha_weft))^2
0 (cos(anpha_weft))^2 0 -2*sin(anpha_weft)*cos(anpha_weft) 0;0 0 0 0 cos(anpha_weft) 0
-sin(anpha_weft);-sin(anpha_weft)*cos(anpha_weft) 0 sin(anpha_weft)*cos(anpha_weft) 0
(cos(anpha_weft))^2-(sin(anpha_weft))^2 0;0 0 0 0 sin(anpha_weft) 0 cos(anpha_weft)];

    delta_Cg_weft = k_weft*T_sigma_weft*Cl_weft*inv(T_epsilon_weft);
    Cg_weft = Cg_weft+delta_Cg_weft;
end

Cg = km*Cg_m+4*Cg_warp+4*Cg_weft;
Sg=inv(Cg);
Ex = 1/Sg(1,1)
Ey = 1/Sg(2,2)
nuyxy = -Sg(1,2)/Sg(2,2)
Gxy = 1/Sg(6,6)

```

B.3. “Crimpmodelisostress” function

```

function[Ex,Ey,nuyxy,Gxy]=crimpmodelisostress(EL_warp,EL_weft,ET,nuyLT,GLT,nuyTT,GTT,phi_warp,
phi_weft,k_warp,k_weft,km)
Em = 11.7;
nuy_m = 0.05;
Gm = Em/(2*(1+nuy_m));
Sg_m = [1/Em -nuy_m/Em -nuy_m/Em 0 0 0;-nuy_m/Em 1/Em -nuy_m/Em 0 0 0;-nuy_m/Em -nuy_m/Em 1/Em
0 0 0;0 0 0 1/Gm 0 0;0 0 0 0 1/Gm 0;0 0 0 0 0 1/Gm];

Sl_warp = [1/EL_warp -nuyLT/EL_warp -nuyLT/EL_warp 0 0 0;-nuyLT/EL_warp 1/ET -nuy_m/ET 0 0 0;-
nuyLT/EL_warp -nuy_m/ET 1/ET 0 0 0;0 0 0 1/GTT 0 0;0 0 0 0 1/GLT 0;0 0 0 0 0 1/GLT];
Sg_warp = [0 0 0 0 0 0;0 0 0 0 0 0;0 0 0 0 0 0;0 0 0 0 0 0;0 0 0 0 0 0;0 0 0 0 0 0];
for i = 1:10
    anpha_warp = ((phi_warp/20)*3.14/180)*(-2*i+11);

    T_epsilon_warp = [0 (cos(anpha_warp))^2 (sin(anpha_warp))^2
sin(anpha_warp)*cos(anpha_warp) 0 0;1 0 0 0 0 0;(sin(anpha_warp))^2 (cos(anpha_warp))^2
-sin(anpha_warp)*cos(anpha_warp) 0 0;0 0 0 0 cos(anpha_warp) -sin(anpha_warp);
0 -2*sin(anpha_warp)*cos(anpha_warp) 2*sin(anpha_warp)*cos(anpha_warp)
(cos(anpha_warp))^2-(sin(anpha_warp))^2 0 0;0 0 0 0 sin(anpha_warp) cos(anpha_warp)];

    T_sigma_warp = [0 (cos(anpha_warp))^2 (sin(anpha_warp))^2
2*sin(anpha_warp)*cos(anpha_warp) 0 0;1 0 0 0 0 0;(sin(anpha_warp))^2
(cos(anpha_warp))^2 -2*sin(anpha_warp)*cos(anpha_warp) 0 0;0 0 0 0 cos(anpha_warp)
-sin(anpha_warp);0 -sin(anpha_warp)*cos(anpha_warp) sin(anpha_warp)*cos(anpha_warp)
(cos(anpha_warp))^2-(sin(anpha_warp))^2 0 0;0 0 0 0 sin(anpha_warp) cos(anpha_warp)];

    delta_Sg_warp = k_warp*T_epsilon_warp*Sl_warp*inv(T_sigma_warp);
    Sg_warp = Sg_warp+delta_Sg_warp;
end

Sl_weft = [1/EL_weft -nuyLT/EL_weft -nuyLT/EL_weft 0 0 0;-nuyLT/EL_weft 1/ET -nuy_m/ET 0 0 0;-
nuyLT/EL_weft -nuy_m/ET 1/ET 0 0 0;0 0 0 1/GTT 0 0;0 0 0 0 1/GLT 0;0 0 0 0 0 1/GLT];
Sg_weft = [0 0 0 0 0 0;0 0 0 0 0 0;0 0 0 0 0 0;0 0 0 0 0 0;0 0 0 0 0 0;0 0 0 0 0 0];
for i = 1:10
    anpha_weft = ((phi_weft/20)*3.14/180)*(-2*i+11);

    T_epsilon_weft = [(cos(anpha_weft))^2 0 (sin(anpha_weft))^2 0
sin(anpha_weft)*cos(anpha_weft) 0;0 1 0 0 0 0;(sin(anpha_weft))^2 0 (cos(anpha_weft))^2
-sin(anpha_weft)*cos(anpha_weft) 0;0 0 0 cos(anpha_weft) 0 -sin(anpha_weft);
-2*sin(anpha_weft)*cos(anpha_weft) 0 2*sin(anpha_weft)*cos(anpha_weft) 0
(cos(anpha_weft))^2-(sin(anpha_weft))^2 0;0 0 0 sin(anpha_weft) 0 cos(anpha_weft)];

    T_sigma_weft = [(cos(anpha_weft))^2 0 (sin(anpha_weft))^2 0
2*sin(anpha_weft)*cos(anpha_weft) 0;0 1 0 0 0 0;(sin(anpha_weft))^2 0 (cos(anpha_weft))^2
0 -2*sin(anpha_weft)*cos(anpha_weft) 0;0 0 0 cos(anpha_weft) 0 -sin(anpha_weft);
-sin(anpha_weft)*cos(anpha_weft) 0 sin(anpha_weft)*cos(anpha_weft) 0
(cos(anpha_weft))^2-(sin(anpha_weft))^2 0;0 0 0 sin(anpha_weft) 0 cos(anpha_weft)];

    delta_Sg_weft = k_weft*T_epsilon_weft*Sl_weft*inv(T_sigma_weft);
    Sg_weft = Sg_weft+delta_Sg_weft;
end

Sg = km*Sg_m+4*Sg_warp+4*Sg_weft;
Ex = 1/Sg(1,1)
Ey = 1/Sg(2,2)
nuyxy = -Sg(1,2)/Sg(2,2)
Gxy = 1/Sg(6,6)

```

B.4. “Crimpmodel_thermal” function

```

function[alpha_x,alpha_y,alpha_xy]=crimpmodel_thermal(alpha_L,alpha_T,phi_warp,phi_weft,k_warp
,k_weft,km)
alpha_m = 15e-6;
alpha_matrix = [alpha_m alpha_m alpha_m 0 0 0]';
alpha_l_yarn = [alpha_L alpha_T alpha_T 0 0 0]';

alpha_g_warp = [0 0 0 0 0 0]';
for i = 1:10
    anpha_warp = ((phi_warp/20)*3.14/180)*(-2*i+11);

    T_epsilon_warp = [0 (cos(anpha_warp))^2 (sin(anpha_warp))^2
    sin(anpha_warp)*cos(anpha_warp) 0 0;1 0 0 0 0 0;0 (sin(anpha_warp))^2 (cos(anpha_warp))^2
    -sin(anpha_warp)*cos(anpha_warp) 0 0;0 0 0 0 cos(anpha_warp) -sin(anpha_warp);
    0 -2*sin(anpha_warp)*cos(anpha_warp) 2*sin(anpha_warp)*cos(anpha_warp)
    (cos(anpha_warp))^2-(sin(anpha_warp))^2 0 0;0 0 0 0 sin(anpha_warp) cos(anpha_warp)];

    delta_alpha_g_warp = k_warp*inv(T_epsilon_warp)*alpha_l_yarn;
    alpha_g_warp = alpha_g_warp+delta_alpha_g_warp;
end

alpha_g_weft = [0 0 0 0 0 0]';
for i = 1:10
    anpha_weft = ((phi_weft/20)*3.14/180)*(-2*i+11);

    T_epsilon_weft = [(cos(anpha_weft))^2 0 (sin(anpha_weft))^2
    0 sin(anpha_weft)*cos(anpha_weft) 0;0 1 0 0 0 0;(sin(anpha_weft))^2 0 (cos(anpha_weft))^2
    0 -sin(anpha_weft)*cos(anpha_weft) 0;0 0 0 cos(anpha_weft) 0 -sin(anpha_weft);
    -2*sin(anpha_weft)*cos(anpha_weft) 0 2*sin(anpha_weft)*cos(anpha_weft)
    0 (cos(anpha_weft))^2-(sin(anpha_weft))^2 0;0 0 0 sin(anpha_weft) 0 cos(anpha_weft)];

    delta_alpha_g_weft = k_weft*inv(T_epsilon_weft)*alpha_l_yarn;
    alpha_g_weft = alpha_g_weft+delta_alpha_g_weft;
end

alpha_g = km*alpha_matrix+4*alpha_g_warp+4*alpha_g_weft;
alpha_x = alpha_g(1)
alpha_y = alpha_g(2)
alpha_z = alpha_g(3)
alpha_xy = alpha_g(6)

```